University of Cape Town

An Experimental and Theoretical Study on the Effect of Strain Rate on Ductile Damage

Author: Matthew Weyer

Supervisor: Mr. Trevor Cloete

Co-Supervisor: Dr. Reuben Govender

A dissertation submitted in fulfilment of the requirements for the degree of M.Sc. Mechanical Engineering

in the

Blast Impact and Survivability Research Unit
Department of Mechanical Engineering

BISRU

May 2016

University of Cape Town

The copyright of this thesis vests in the author. No quotation from it or information derived from it is to be published without full acknowledgement of the source. The thesis is to be used for private study or non-commercial research purposes only.

Published by the University of Cape Town (UCT) in terms of the non-exclusive license granted to UCT by the author.

University of Cape Town

Declaration of Authorship

I, Matthew Weyer, declare that this thesis titled, 'An Experimental and Theoretical Study on the Effect of Strain Rate on Ductile Damage' and the work presented in it are my own. I confirm that:

- "I know the meaning of plagiarism and declare that all the work in the document, save for that which is properly acknowledged, is my own.
- Where any part of this thesis has previously been submitted for a degree or any other qualification at this University or any other institution, this has been clearly stated.
- Where I have quoted from the work of others, the source is always given. With the exception of such quotations, this thesis is entirely my own work.

Signed: 

Date: 12/02/2016

UNIVERSITY OF CAPE TOWN

Abstract

Engineering and the Built Environment
Department of Mechanical Engineering

M.Sc. Mechanical Engineering

An Experimental and Theoretical Study on the Effect of Strain Rate on Ductile Damage

by Matthew Weyer

Simulation of fracture in ductile materials is a challenging problem, since it typically occurs at length scales that are orders of magnitude smaller than that of the structures in which the fracture is occurring and, hence, difficult to resolve . One approach is to avoid modelling the micro-mechanics of ductile fracture by describing the macroscopic effects of fracture using damage parameters. Damage in metals can be defined as a measure of discontinuous deformation of a body. Many numerical models include some measure of damage to predict when a material will fracture under certain conditions, however there is little consensus as to what measures and parameters will accurately predict the onset of fracture. Most notably, the effect of strain rate at the point of fracture is significant and must be taken into account. The literature indicates that in the quasistatic regime where inertial effects are negligible, an increase in strain rate increases the strain at fracture. However, the research conducted in this dissertation suggests the opposite is true. The aim of this research is to conduct further high strain rate ductile damage experiments so as to extend the available data set, and develop a pragmatic damage model to relate the plastic strain at fracture to material parameters such as triaxiality, lode angle and strain rate in a specimen, which is verified using experiments performed under various loading conditions and strain rates.

Acknowledgements

Firstly, and perhaps most importantly, I must thank my supervisors, Mr Trevor Cloete and Dr Reuben Govender, without whom I would not have the guidance and support required to tackle the challenges I faced during my studies. Thank you to Mr Cloete for the many long hours spent talking over the countless small details and concepts which went into completing this dissertation, and to Dr Govender for the fresh perspective provided when I was too engrossed in the research to see the bigger picture.

To the staff and students of BISRU, thank you for support and companionship throughout my two years at the research unit. Whenever I needed a helping hand, or a pair of ears to listen to my problem of the day, someone was always available and willing to help.

Thank you to the NRF, as well as BISRU, who both funded my research, which ultimately made it possible for me to complete my studies over the past two year, as well as SSAB, who donated the material used for testing during this dissertation.

For the advice, assistance, and tireless efforts of the UCT Mechanical Engineering workshop staff, I extend my gratitude. Mr Pierre Smith was instrumental in the design and manufacture of all the components and specimens required tests performed during the research.

Lastly, I am eternally grateful to all my friends and family. The love and support given by those close to me made the last two years some of the best of my life.

Contents

List of Figures

List of Tables

Abbreviations

BISRU	**B**last **I**mpact and **S**urvivability **R**esearch **U**nit
MSE	**M**ean **S**quare **E**rror
MSS	**M**aximum **S**hear **S**tress
SHPB	**S**plit **H**opkinson **P**ressure **B**ar

Symbols

c	wave speed	m/s
c_p	specific heat capacity	kJ/kgK
E	elastic modulus	MPa
G	elastic shear modulus	MPa
GF	gauge factor	-
p	hydrostatic pressure	MPa
S_{ij}	deviatoric stress tensor component	MPa
$\mathbb{C}_{ijkl}$	elastic constitutive tensor component	MPa
ε	equivalent strain	
$\dot{\varepsilon}$	equivalent strain rate	s^{-1}
η	triaxiality	
θ	Lode angle	rad
$\bar{\theta}$	normalised Lode angle	
ν	Poisson's ratio	
ρ	density	kg/m^3
σ	stress	MPa

Chapter 1

Introduction

The phenomenon of ductile fracture in metals has been formally studied since as early as 1949, when Tipper observed the growth of holes in ductile metals [1]. Since then, ductile fracture has been shown to be strongly linked to hydrostatic tension [2–4] through continuum mechanics based damage analyses, and numerical models incorporating the findings thereof, such as the Johnson-Cook damage model [5], are commonly used today. However recent findings by Bao and Wierzbicki [6] suggest that the dependence of the strain at failure on hydrostatic pressure is not monotonic, and subsequently it has been found that a second parameter, the Lode angle, which describes the directionality of the loading, is needed to accurately describe the ductile failure behaviour of a material over a large range of loading conditions [7, 8].

Although modern numerical models like the Johnson-Cook damage model include rate dependency, their has been relatively little research into the effect of strain rate on the strain at failure in comparison to the effect of the loading conditions. Considering that many simulations incorporating material failure attempt to replicate complex failure modes, a damage model is required which is accurate over a large range of loading conditions and strain rates. In this dissertation, a suitable model is chosen, and an experimental and numerical procedure is developed to calibrate said model over a range of strain rates with the goal of observing and quantifying trends in the effect of strain rate on ductile damage.

1.1 Motivation

The work done at the Blast Impact and Survivability Research Unit (BISRU) primarily involves the blast and impact loading of structures to better understand the mechanics and dynamics involved, with the purpose of reducing risk through injury and saving lives through protection against blast and high speed impact events. The study of such events often involves numerical simulations of high strain rate experiments, such as blast loading of plates, which must replicate the experiment as accurately as possible. Since these experiments often lead to tearing in the material, a constitutive model is required which accurately predicts the onset of fracture in a material not only at quasistatic strain rates ($<1s^{-1}$), but also at dynamic rates ($>100s^{-1}$), over a large range of loading conditions. BISRU's primarily tests high strength steels due to their common use in protective structures, which is why the focus of this research is to develop a testing and calibration procedure for a chosen damage model using a high strength steel, and to analyse and characterise the fracture behaviour of the material.

Similar work was performed by Bowden in 2009 [9], but although the procedure was sound, the quality of data, particularly for the dynamic strain rate range, was not adequate to draw any conclusions other than qualitative observations. This research aims to improve on the quality and quantity of data available by improving both the manufacturing method for the specimens to be tested and the testing method at dynamic strain rates.

1.2 Objectives

The aims of this research can be summarised into two broad requirements as follows:

1. Develop a procedure to investigate and quantify the fracture characteristics of the chosen material.
   (a) Choose a suitable damage model.
   (b) Perform tensile tests on required specimen geometries to obtain data illustrating fracture behaviour for different loading conditions.
   (c) Write a user-defined material model in LS-DYNA implementing the desired plasticity and fracture behaviour.

(d) Simulate the experimental tests to determine required parameters at the fracture location.

(e) Calibrate the damage model

2. Determine the effect of strain rate on the fracture characteristics of the chosen material.

(a) Quantify the fracture characteristics over a range of strain rates.

(b) Investigate the differences in the damage model parameters for the different strain rates.

(c) Quantify the effects of strain rate to create a damage model incorporating strain rate effects

1.3 Dissertation Outline

The required theory, the procedure followed and the results obtained are all described in the following sections:

- A review of the commonly used damage models and their predecessors, as well as the information required for the calibration thereof:
  - A chronological summary and assessment of the different damage models.
  - An assessment of a selection of relevant plasticity models required for the numerical modelling of plastic deformation of steels.
  - An investigation into the specimen design requirements for the calibration of a chosen damage model.
- An outline of the experimental and numerical procedure required for the calibration of the chosen damage model:
  - A description of the testing methods used.
  - The design choices made for the specimens to be used.
  - An explanation of the implementation of the chosen plasticity model, as well as the requirements for replicating the tests performed in a finite element analysis.
  - A summary of the procedure used to calibrate the damage model, as well as to determine the effect of strain rate on the model.

- A qualitative analysis of the experimental results, discussing the trends observed regarding the strain at failure:
  - A comparison of the force-displacement curves obtained for each specimen geometry at the different strain rates tested.
  - A comparison of the sizes of the surfaces at the location of failure of the tested specimens.
- A quantitative analysis of the effect of strain rate on ductile damage through a comparison of the numerical results at the different strain rates:
  - An assessment of the accuracy of the calibrated plasticity model.
  - A confirmation of the qualitative trends observed in the experimental tests through an analysis the numerical results.
  - An analysis of the trends shown in the damage model calibration for the different strain rates.
  - A description of a calibrated damage model including strain rate effects.
  - A verification of the model.
- A summary of the challenges met and the conclusions drawn through the research, as well as recommendations for improving the procedure followed and results obtained for future research in the field.

Chapter 2

Literature Review

In this chapter, the current literature relevant to the topic of ductile damage is reviewed. A selection of plasticity models applicable to the modelling of high strength steels are investigated, as accurately modelling the deformation in a specimen prior to failure is of utmost importance when using a numerical model to investigate the parameters affecting ductile damage. Secondly, the existing widely-used damage models are investigated in chronological order to illustrate the evolution of damage modelling and the logic behind why the modern damage models are formulated as they are. The theory required for split-Hopkinson pressure bar analysis is then summarised, and lastly, a review of the different specimens typically used to calibrate existing damage models is conducted in order to determine the design and manufacturing requirements for the successful calibration of a damage model.

2.1 Plasticity Models

Plasticity models are used to define the constitutive behaviour of a material during the region of non-reversible, or plastic deformation. It is pertinent to first investigate popular plasticity models before considering the damage models, as it is important to correctly capture the plastic deformation of the material before fracture occurs. Incremental plastic constitutive theory requires a function of the stress state which determines whether or not the material has yielded, a flow rule which describes the direction of the plastic flow, and a consistency condition together with a hardening rule relating the magnitude of the plastic strain increment to a stress increment [10]. The yield function is given by Equation 2.1, where $\bar{\sigma}$ represents the flow stress, H represents

the hardening law, and the parameters ε^p, $\dot{\varepsilon}^p$ and T represent the plastic strain, plastic strain rate and temperature respectively.

$$f = \bar{\sigma} - H(\varepsilon^p, \dot{\varepsilon}^p, T) \leq 0 \tag{2.1}$$

The hardening law, H, describes the change in flow stress as the material plastically deforms, and varies between different constitutive models. Three popular forms of hardening laws will be discussed, namely Johnson-Cook [11], Zerilli-Armstrong [12], and Zhao [13].

2.1.1 Johnson - Cook

The Johnson-Cook model is a relatively simple phenomenological model developed for use in numerical computations [11]. The model was based on torsional and tensile test data performed over a range of strain rates and temperatures for three different materials. The description of the flow stress is given in Equation 2.2.

$$\bar{\sigma} = [A + B\varepsilon^n][1 + Cln\dot{\varepsilon}^*][1 - (T^*)^m] \tag{2.2}$$

In the above Equation, ε represents the equivalent plastic strain, $\dot{\varepsilon}^*$ represents the dimensionless plastic strain rate, and T^* represents the homologous temperature. The dimensionless strain rate and homologous temperature are described in Equations 2.3 and 2.5.

$$\dot{\varepsilon}^* = \frac{\dot{\varepsilon}}{\dot{\varepsilon}_0} \tag{2.3}$$

$$\tag{2.4}$$

$$T^* = \begin{cases} 0 & \text{if } T < T_{ref} \\ \frac{T - T_{ref}}{T_m - T_{ref}} & \text{if } T_{ref} \geq T \leq T_m \\ 1 & \text{if } T > T_m \end{cases} \tag{2.5}$$

ε_0 is a reference strain rate, which was taken as $1.0s^{-1}$ for the data used by Johnson and Cook, and T_{ref} and T_m are the reference and melting temperatures respectively. The homologous temperature is set to zero for temperatures less than the reference temperature such that the temperature function has no effect on the flow stress, and one for temperatures above the melting temperature such that the flow stress is zero and the material exhibits no resistance to flow.

A popular adaptation of the Johnson - Cook model uses the Cowper - Symonds strain rate equation [14] in place of the standard strain rate dependence function. The Cowper - Symonds equation is shown in Equation 2.6.

$$\frac{\sigma}{\sigma_0} = 1 + \left(\frac{\dot{\varepsilon}^*}{D}\right)^{\frac{1}{q}} \tag{2.6}$$

This equation is consistent at strain rates approaching zero, unlike the equation employed Johnson and Cook, which can yield a negative flow stress very low strain rates.

2.1.2 Zerilli - Armstrong

The Zerilli-Armstrong constitutive equations are dislocation-mechanics-based so as to capture the different behaviour for materials with different micro-structures [12]. More specifically, the model incorporates two different equations to describe the flow stress for body-centred cubic and face-centred cubic materials. Like the Johnson-Cook model, the constitutive relations incorporate the effects of plastic strain, strain rate and temperature on the material hardening. However, the form of the Zerilli-Armstrong model is somewhat different, as the different functions are not separable as in the Johnson - Cook model, and the effects of strain rate and temperature are interdependent. The flow stress equations for BCC and FCC materials are shown in Equations 2.7 and 2.8 respectively.

$$\sigma_{BCC} = C_0 + C_1 \exp(-C_3 + C_4 T ln\dot{\varepsilon}^*) + C_5 \varepsilon^n \tag{2.7}$$

$$\sigma_{FCC} = C_0 + C_2 \varepsilon^{1/2} \exp(-C_3 T + C_4 T ln\dot{\varepsilon}^*) \tag{2.8}$$

In the model, for BCC materials such as iron, the yield stress is dependent on temperature and strain rate, but the strain hardening curve is independent of these parameters, whereas for FCC

materials such as copper, the strain rate and temperature have no effect on the yield stress, but do have an effect on the hardening rate. The term $\exp(-C_3 + C_4 T ln\dot{\varepsilon}^*)$, represents the thermally activated component of plastic flow, which is uncoupled from the plastic strain for BCC materials and is coupled to the plastic strain for FCC materials. The terms C_0 and $C_5\varepsilon^n$ represent the athermal components of plastic flow.

2.1.3 Zhao

In 1997, Han Zhao developed a phenomenological model similar to that of the Johnson - Cook model, but incorporating a more complete description of the strain rate dependence. Zhao argued that a linear approximation for strain rate effects is valid for quasistatic and high strain rates separately ($\dot{\varepsilon} > 100s^{-1}$ and $\dot{\varepsilon} < 1s^{-1}$), however is not valid in the intermediate region or across the entire range of strain rates [13]. This behaviour is illustrated in Figure 2.1.

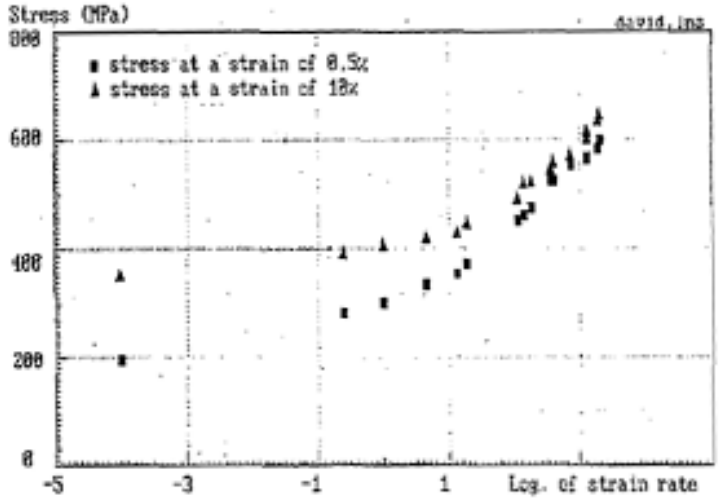

Figure 2.1: The effect of strain rate on flow stress for mild steel sheets at different strains [13].

Zhao proposed a model for metals and alloys comprised of an additive combination of three functions describing the flow stress behaviour due the contributions from quasistatic, thermally actived, and viscous drag components. The model is described in Equations 2.9 and 2.10.

$$\sigma = \sigma_s(\varepsilon, T) + \sigma_t(\varepsilon, \dot{\varepsilon}, T) + \sigma_v(\varepsilon, \dot{\varepsilon}, T) \tag{2.9}$$

$$= \left[A + B\varepsilon^n + (C - D\varepsilon^m)log(\dot{\varepsilon}^*) + E\dot{\varepsilon^*}^k\right] f(T) \tag{2.10}$$

As can be seen, the quasistatic component of the flow stress is a strain hardening function the same as that used in the Johnson - Cook model, the thermally activated component displays a log-linear rate dependence, and the viscous drag component is described by a power law function. Like the Johnson - Cook model, the temperature function is separable from the plastic strain and strain rate functions. However unlike the Johnson - Cook model, the plastic strain and strain rate functions are additive, not multiplicative. This allows the material to exhibit behaviour more common to BCC materials. Note the second term in the thermally activated component results in a decrease in rate effects as the material is strained. As can be seen in Figure 2.1, the gradient of the linear rate dependence regime decreases as the strain increases. The combination of the thermally activated and viscous drag components are shown in Figure 2.2.

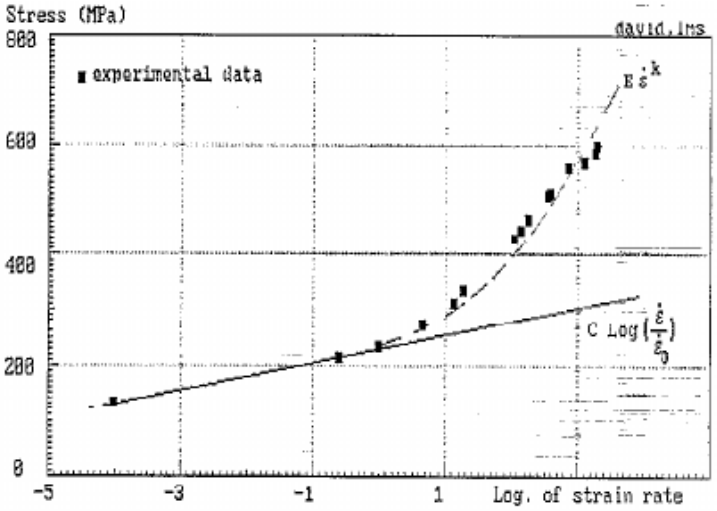

Figure 2.2: A graphical representation of the contributions of the thermally activated and viscous drag components of the Zhao model [13].

The model is valid over a large range of strain rates and relatively straight forward to calibrate.

2.2 Existing Damage Models

This dissertation focuses on the development of macroscopic cracks in an initially crack-free body. For this reason it is pertinent not to consider the implementation of models which require prior knowledge of where fracture will occur, such as the cohesive zone model which follows the concept proposed by Barenbolatt [15]. The research shall focus on models which use damage parameters to predict when a point will begin to fracture based on a postulated damage evolution law. These models can be divided into three types as suggested by Bai & Wierzbicki [16], namely physics or continuum mechanics based models, phenomenological models and empirical models.

For the purpose of this dissertation, the phenomenological and empirical models will be grouped for the sake of convenience, as both are empirical by nature, being driven by trends identified in data.

Continuum mechanics-based models are generally difficult to calibrate, since the parameters are often very difficult to measure. Many of the parameters are related to microscopic mechanisms, such as void growth, making them difficult to determine via experiments. Phenomenological models are generally easier to calibrate via a set of experiments which do not require processes such as microscopy, and empirical models are even more so. However, empirical models often come with a set of conditions, outside which they are not valid, due to the lack of physical bases in their derivations.

2.2.1 Continuum Mechanics Based Models

This type of model considers the growth of micro voids in a continuum and developing damage evolution equations based on continuum mechanics theory rather than experimental observation.

McClintock

McClintock analysed the growth of mutually perpendicular set of circular or elliptical cross-sectional holes with axes coinciding with the principle stress axes in an infinite continuum material [2].

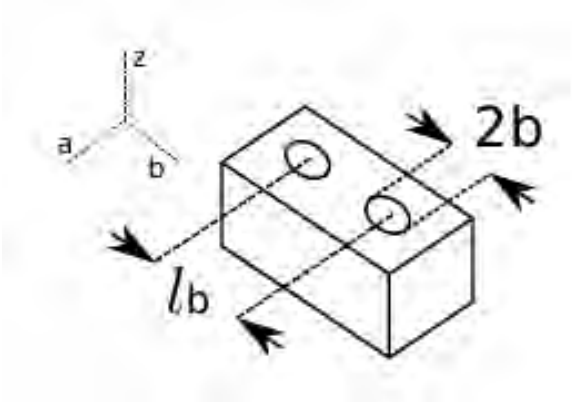

Figure 2.3: A single set of holes used by McClintock for the analysis of void growth with axes in the z-direction coalescing in the b-direction.

McClintock defined a relative growth factor for the holes given by Equation 2.11 for a pair of holes as shown in Figure 2.3.

$$F_{zb} = (b/l_b)/(b^0/l_b^0) \tag{2.11}$$

Fracture was deemed to have occurred when the growth was such that the holes touched one another, i.e. when $b = l_b/2$.

This model represents the growth of micro voids which has is commonly believed to be the dominant mode of ductile fracture in the range of high stress triaxiality. McClintock showed that an increase in triaxiality reduces the strain at fracture, suggesting that the effect of the growth of micro voids present in the material increases at higher triaxialities. McClintock noticed that the model did not agree well with data for pure tensile tests, suggesting that void is growth only the dominating fracture mechanism for large hydrostatic tensions. A convenient measure of hydrostatic pressure is the stress triaxiality, η, which is defined as the ratio between the hydrostatic tension, σ_m and the flow stress, $\bar{\sigma}$.

$$\eta = \frac{\sigma_m}{\bar{\sigma}} \tag{2.12}$$

Mclintock found that for constant ratios between applied stresses, the strain at failure could be given as a function of the strain hardening exponent, n, the applied transverse stresses, and the geometry of the holes, as shown in Equation 2.13 [2]. The strain hardening exponent describes the flow stress in the material during plastic deformation by $\bar{\sigma} = A\varepsilon^n$.

$$\varepsilon_f = \frac{(1-n)\ln(l_b^0/2b^0)}{\sinh[(1-n)(\sigma_a+\sigma_b)/(2\bar{\sigma}/\sqrt{3})]} \tag{2.13}$$

The McClintock fracture criterion shown in Equation 2.13 suggests strain at fracture is closely related to the tensile stress transverse to the hole axes. Higher transverse stresses result in higher hydrostatic tension or triaxiality, which facilitates the growth of voids.

Rice and Tracey

Rice and Tracey extended the work of McClintock to the analysis of the growth of spherical voids which are more representative of the micro voids present in materials undergoing plastic deformation. The dilatational amplification factor, D is defined ratio of the average strain rate of the void's radius to the imposed strain rate [3].

$$D = \frac{\dot{R}_0}{\dot{\varepsilon} R_0} \tag{2.14}$$

R_0 and $\dot{R}_0$ represent the initial void radius and the rate of change of the void radius respectively. D can be interpreted as a factor defining the rate of growth of the voids relative to the imposed strain rate. Rice and Tracey found that for high triaxialities the dilitational amplification factor to be related to triaxiality by Equation 2.15 [3].

$$D = Ce^{3/2\eta} \tag{2.15}$$

Failure is defined as occurring when the void boundaries reach a critical size, which can be written mathematically as:

$$\int_0^{\bar{\varepsilon}_f} D \mathrm{d}\bar{\varepsilon} = C_1 \tag{2.16}$$

For a constant stress state, the strain at failure can then be written as:

$$\bar{\varepsilon_f} = Ae^{-3/2\eta} \tag{2.17}$$

A more general form of this has been used in subsequent models, as written in Equation 2.18.

$$\bar{\varepsilon_f} = Ae^{-B\eta} \tag{2.18}$$

Gurson/GNT

Gurson followed a similar approach to the aforementioned authors by considering both the growth of a sphere and a cylinder in a unit cube of continuum material under an axial stress with a superimposed hydrostatic stress [4]. He noted that the results obtained represented estimates for materials with a more random distribution of voids. By considering the distortional strain of the material, as well as the dilatational strain of the void, Gurson was able to modify the Von Mises plastic flow yield criterion to include the effect of void growth, as shown for spherical voids

under spherically symmetric deformation in Equation 2.19. Φ represents the yield criterion, such that $\Phi \leq 0$.

$$\Phi = \left(\frac{\bar{\sigma}}{\sigma_y}\right)^2 + 2f\cosh\left(\frac{3\sigma_m}{2\sigma_y}\right) - 1 - f^2 \tag{2.19}$$

where σ_y is a constant representing the material's initial yield strength, and f is the volume fraction of the voids in the material, which is updated according to the void growth after each strain increment. Note that Gurson's original model did not consider a critical value for f at which the material was deemed to have fractured, focusing rather on the effect of void growth on the yield behaviour of the material. This means a fracture locus cannot be obtained from the original model.

Tvergaard modified Gurson's model to include a constant, q_1 such that the model would correspond more closely with experimental data [17]. Needleman and Tvergaard then later extended Gurson's work to include the effect of void nucleation in the material constitutive description [18],[19], by changing the void volume fraction to include a critical value, f_c, at which the material's load-carrying capacity would begin to decay more rapidly, and eventually lose any load-carrying capacity when $f = f_F$, at which point failure has occured. The results of these modifications are shown in Equations 2.20 and 2.21, which describe the Gurson, Needleman and Tvergaard (GNT) model,

$$\Phi = \left(\frac{\bar{\sigma}}{\sigma_y}\right)^2 + 2f * q_1\cosh\left(\frac{3\sigma_m}{2\sigma_y}\right) - 1 - (q_1 f^*)^2 \tag{2.20}$$

$$f^{=} \begin{cases} f & : f \leq f_c \\ f_c + \frac{f_u^* - f_c}{f_F - f_c}(f - f_c) & : f > f_c \end{cases} \tag{2.21}$$

where $f_u^* = 1/q_1$.

2.2.2 Phenomenological and Empirical Models

Following the previously discussed models, are the models which are not based on a continuum mechanics analysis, but rather rely on experimental data to determine critical values for certain parameters which are proposed rather than derived via analysis.

Constant Fracture Strain

The simplest of any commonly used damage model suggests that fracture occurs when the equivalent plastic strain reaches a critical value, as shown in Equation 2.22.

$$\bar{\varepsilon}_f = \sqrt{\frac{2}{3}\varepsilon^p_{ij}\varepsilon^p_{ij}} \tag{2.22}$$

The use of this model dates back as early as the beginning of the 20th century [7], it is widely used in most commercial finite element packages due to its ease of calibration and implementation. However, the model is only accurate for loading conditions used for its calibration, and is unsuitable for models undergoing a wide range of loading conditions.

Maximum Shear Stress (MSS)

The maximum shear stress fracture condition is similar to the Tresca yield condition [10], postulating that fracture occurs in a plane where the maximum shear stress has reached a limiting value, τ_s.

$$\tau_{max} \leq \tau_s \tag{2.23}$$

The model has been successfully applied in geomaterial models such as those used for rock and soil mechanics [7]. A similar model to the MSS model is the Mohr-Coulomb criterion, which includes the effect of pressure in the fracture criterion [20]. The criterion is described in Equation 2.24.

$$max(\tau + c_1\sigma_n)_f \leq c_2 \tag{2.24}$$

σ_n is the normal stress on the plane of maximum shear stress and c_1 and c_2 are material constants which determine the effect of pressure and the limiting stress respectively. Similarly, the Maximum Shear Stress model can be modified to include the effect of pressure by including the hydrostatic stress at the point of fracture [16] as shown in Equation 2.25:

$$(\tau_{max} + c_1\sigma_m)_f \leq c_2 \tag{2.25}$$

where σ_m is the hydrostatic pressure.

Wilkins

Following the physics-based models previously developed, Wilkins observed that fracture is a result of the history of strain damage in the material, which is influenced by two factors: hydrostatic tension and asymmetric strain [21]. Additionally, he observed that the length scale at which damage occurs will affect the fracture behaviour of the materials. The model is given in the following form:

$$D = \int w_1 w_2 \mathrm{d}\bar{\varepsilon}^p \tag{2.26}$$

such that fracture occurs when the damage exceeds a critical value, $D = D_c$. w_1 and w_2 are weighting terms to include the effect of the hydrostatic pressure and asymmetric strain respectively. The weighting terms are defined in Equations 2.27 and 2.28.

$$w_1 = \left(\frac{1}{1 + a\sigma_m}\right)^{\alpha}, \tag{2.27}$$

$$w_2 = (2 - A)^{\beta}, \tag{2.28}$$

$$A = max\left(\frac{s_2}{s_3}, \frac{s_2}{s_1}\right), \quad s_1 > s_2 > s_3. \tag{2.29}$$

s_1, s_2 and s_3 are the principal deviatoric stresses, and A is a measure of the symmetry of the stress field ranging from 0 (fully asymmetric), to 1 (fully symmetric). The respective examples of tests corresponding to these conditions would be a pure shear test and a simple tensile test.

Johnson and Cook

Johnson and Cook developed a damage model of a similar form to the widely used plasticity model previously developed by the same authors [11]. The model incorporated the effect of triaxiality on the effective strain at failure using a form similar to that of the Rice and Tracey model, however it also includes the effects of strain rate and temperature. The damage function

is given as separable function of triaxiality, strain rate, and temperature as shown in Equation 2.30 [5].

$$\bar{\varepsilon}_f = \left[D_1 + D_2 e^{D_4 \eta}\right] \left[1 + D_4 ln(\dot{\varepsilon}^*)\right] \left[1 + D_5 T^*\right] \tag{2.30}$$

The damage constants for the triaxiality function were calibrated using various tensile and torsional tests at quasistatic strain rates, where the triaxialities were approximated using numerical simulations. Using Hopkinson Bar experiments, the constants for the strain-rate and temperature functions could be determined by preheating specimens to a desired temperature before the tests. Since the duration of the test is short enough for the test to be considered adiabatic, the temperature in the specimen could be calculated as a function of the plastic work accumulated during the test. It is worth noting that the model was not calibrated using experiments in the negative triaxiality range, and it was assumed that the model would successfully extrapolate into the negative triaxiality region. Additionally, the data from the torsional tests performed for 4340 steel did not correspond with the model. This was initially disregarded as an anomaly in the testing procedure, but later work by Bao and Wierzbicki [22] suggested that a the fracture locus could not be calibrated by simply extrapolating the tensile data.

Bao - Wierzbicki

In 2004 Bao and Wierzbicki conducted a comparative study on various ductile damage criteria [6] over a wide range of triaxialities. Upsetting tests as well as tensile tests with different notch radii were performed to gather data for the strain at fracture over a range of triaxialities from the negative region for the upsetting tests, to the high triaxiality region for the notched specimens. As previously mentioned, the data suggested that the current commonly used damage criteria did not agree with the data for low to negative triaxiality. The reason postulated for this was that in the negative triaxiality region, the fracture mechanism is predominately shear decohesion, whilst in the high triaxiality region void nucleation and coalescence is dominant, and in the low triaxiality region, the failure mode is a combination of the two. It was suggested that a useful way to compare the results of the various fracture criteria was to plot the strain at failure against the average triaxiality, which is calculated according to Equation 2.31.

$$\eta_{ave} = \frac{1}{\bar{\varepsilon}_f} \int_0^{\bar{\varepsilon}_f} \frac{\sigma_m}{\bar{\sigma}} \mathrm{d}\bar{\varepsilon} \tag{2.31}$$

Figure 2.4 shows the Bao - Wierzbicki model using the effective strain at failure expressed as a function of average triaxiality, as well as data acquired using experiments and parallel simulations. Note the cutoff value of $\eta_{ave} = -1/3$ beyond which it was predicted fracture would not occur.

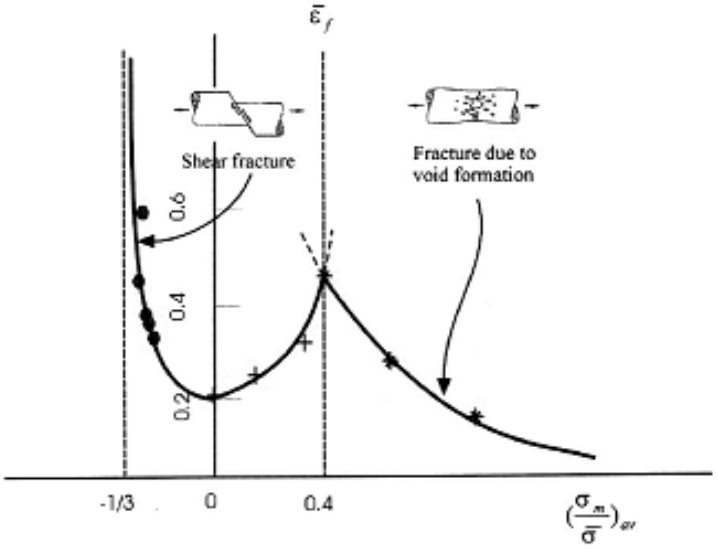

Figure 2.4: The Bao - Wierzbicki fracture locus in the Effective Failure Strain - Average Triaxiality space. [6]

The fracture locus yields a much better fit to the experimental data compared to other models such as Johnson and Cook, as shown in Figure 2.5, as it uses three piecewise functions to capture the different failure modes.

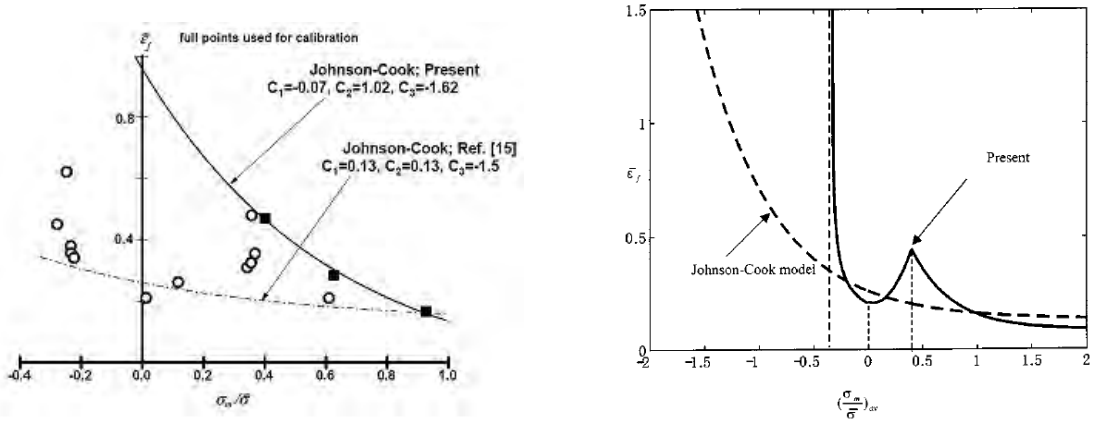

(a) The Johnson-Cook model with experimental data.

(b) The Bao-Wierzbicki and Johnson-Cook fracture loci

Figure 2.5: A comparison of the Bao-Wierzbicki and Johnson-Cook fracture loci. [6]

Using data from Bridgman's experiments [23], as well as a modification of the empirical approximation for triaxiality developed by Bridgman, Bao and Wierzbicki compiled a set of results

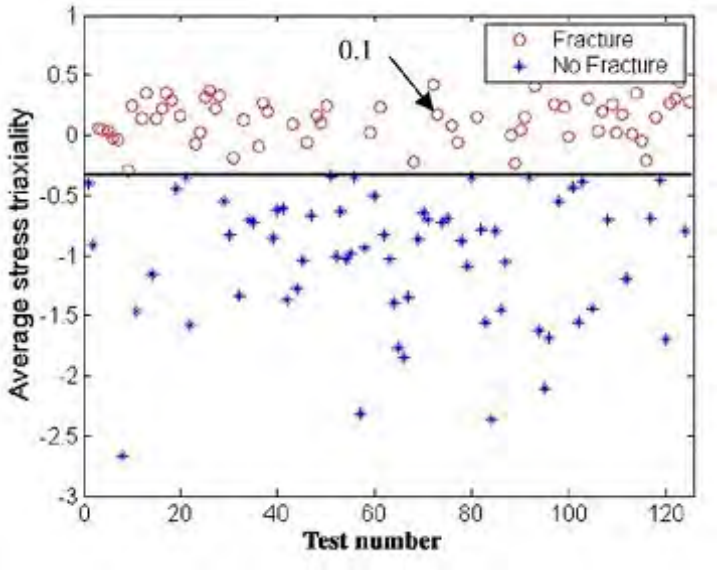

Figure 2.6: Average triaxiality in tests with superimposed hydrostatic pressure performed by Bridgman. [24]

illustrating which specimens fractured as well as their average triaxialities as shown in Figure 2.6.

The significance of this paper is that it was the first of its kind to suggest that the dependence of fracture strain on triaxiality is non-monotonic (i.e. the fracture strain cannot be described by a single function of triaxiality), which led to further developments in ductile fracture. Following this paper Wierzbicki and colleagues began to investigate the reason behind why the triaxiality dependence can not be described using a single function, which led to other parameters being introduced to fully describe the fracture locus.

Xue - Wierzbicki

Following the development of the Bao - Wierzbicki Model, Xue and Wierzbicki developed a model to include the third deviatoric invariant as well as the triaxiality, which is related to the first and second deviatoric invariants. The model [7, 16] assumes that the surface defining the strain at failure can be defined by two bounding functions of triaxiality, as seen in Figure 2.7a.

$$\bar{\varepsilon}_f^{upper} = C_1 e^{-C_2 \eta} \quad , \xi = 1 \tag{2.32}$$

$$\bar{\varepsilon}_f^{lower} = C_3 e^{-C_4 \eta} \quad , \xi = 0 \tag{2.33}$$

The upper bounding function describes the triaxiality dependence for axisymmetric tests, and the lower for plane strain tests. The variable ξ is the normalised third deviatoric invariant as defined by Equation 2.34, where J_3 is the third deviatoric invariant and $\bar{\sigma}$ is the flow stress. The fracture strain's dependence on ξ was assumed to be elliptical, as shown in Figure 2.7b.

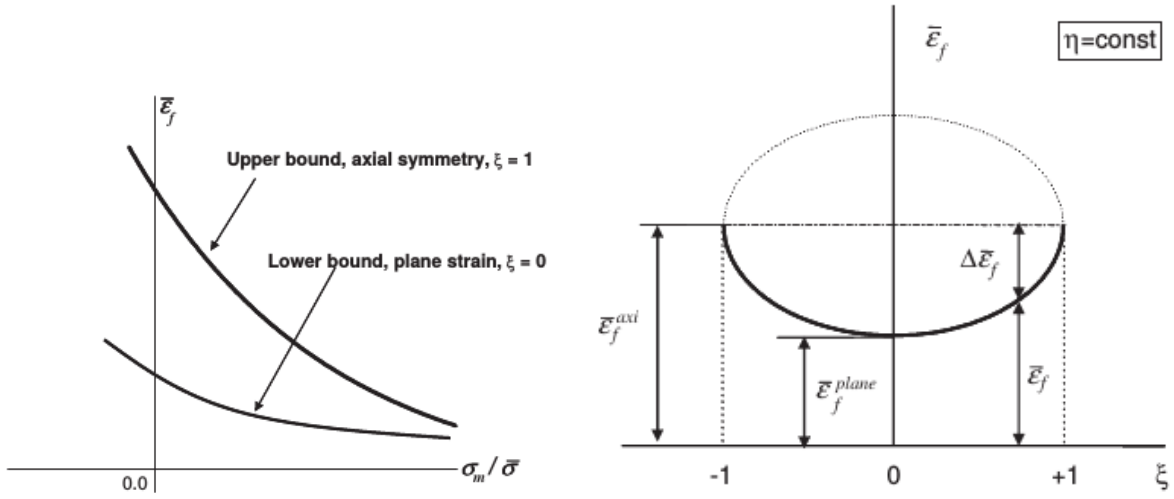

(a) Dependence of the fracture strain on the triaxiality, η.

(b) Dependence of the fracture strain on the normalised third deviatoric invariant, ξ.

Figure 2.7: A representation of the Xu - Wierzbicki model as a combination of two independent functions of triaxiality and the third deviatoric invariant. [7]

$$\xi = \frac{27}{2}\frac{J_3}{\bar{\sigma}^3} \tag{2.34}$$

The failure strain surface is given by Equation 2.35, where n is the material hardening exponent, and the surface is represented in the average $\xi - \eta$ space in Figure 2.8.

$$\bar{\varepsilon}_f = C_1 e^{-C_2\eta} - \left(C_1 e^{-C_2\eta} - C_3 e^{-C_4\eta}\right)\left(1 - \xi^{\frac{1}{n}}\right)^n \tag{2.35}$$

Note the black line on the surface representing the plane stress state. Projecting this line onto the η plane yields the curve shown in Figure 2.9, where m is an integer closest to $1/n$. This curve is very similar to the Bao - Wierzbicki model, which is to be expected since the model was calibrated using predominately plane stress specimens. The significance of the Xue - Wierzbicki model is that it was able to describe the apparent non-monotonic dependence of failure strain on triaxiality using an extra damage parameter, rather than piecewise functions.

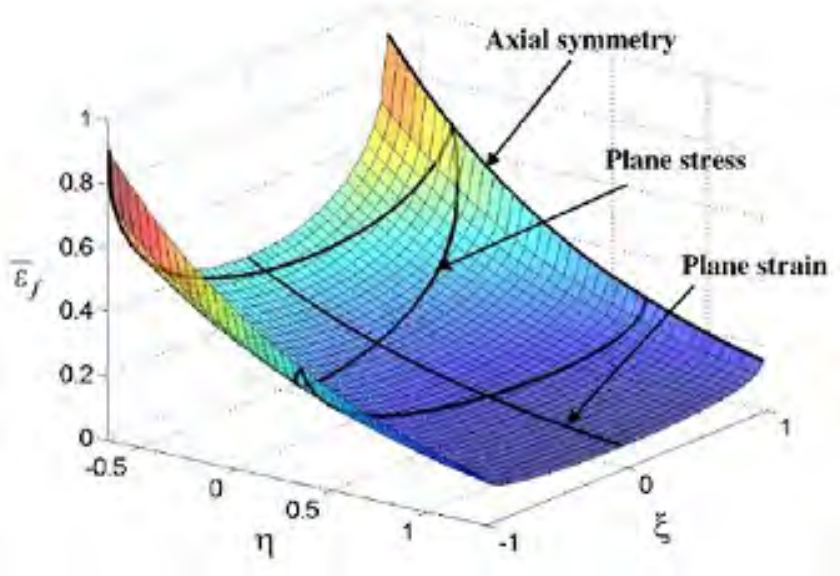

Figure 2.8: The Xue - Wierzbicki failure locus represented as the strain at failure in the average $\xi - \eta$ space. [7]

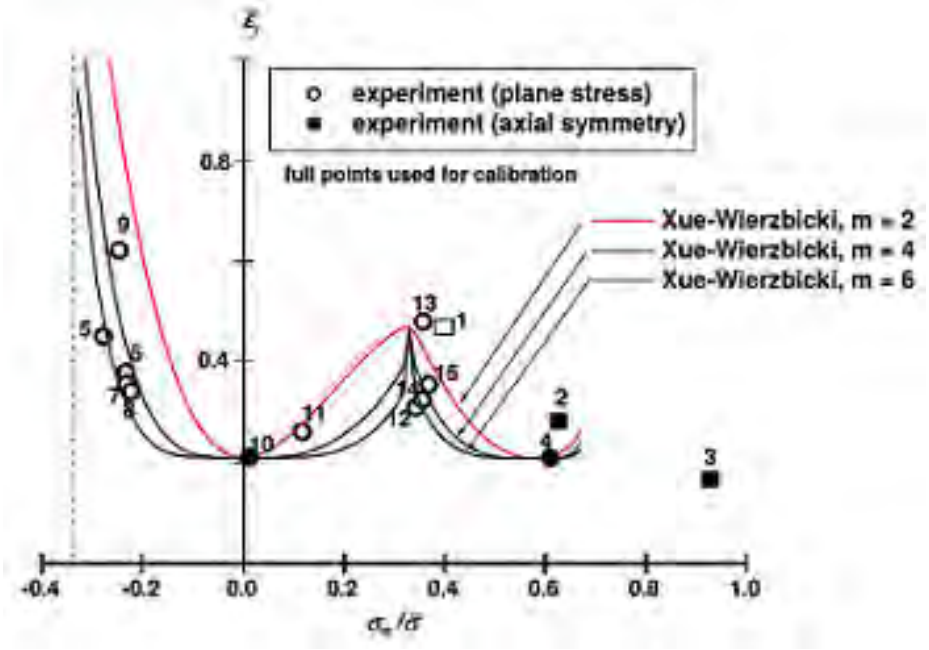

Figure 2.9: The Xue - Wierzbicki failure locus for plan strain represented as a function of η [7].

Bai - Wierzbicki

In 2008 Bai and Wierzbicki further developed the previous two models by changing the dependence of the fracture locus on the third invariant such that the locus was not necessarily symmetric about the line $\xi = 0$ [8]. For this model, the Lode angle was used, which is closely related to the third invariant, as shown in Equation 2.36. The model also included the effect of hydrostatic pressure and Lode angle on plasticity, but for the purpose of this research, only the analysis on fracture will be covered. The interpretation of the Lode angle is shown in Figure 2.10, which shows the principle stress space as viewed from the $(1, 1, 1)$ axis.

$$3\theta = arccos(\xi) \tag{2.36}$$

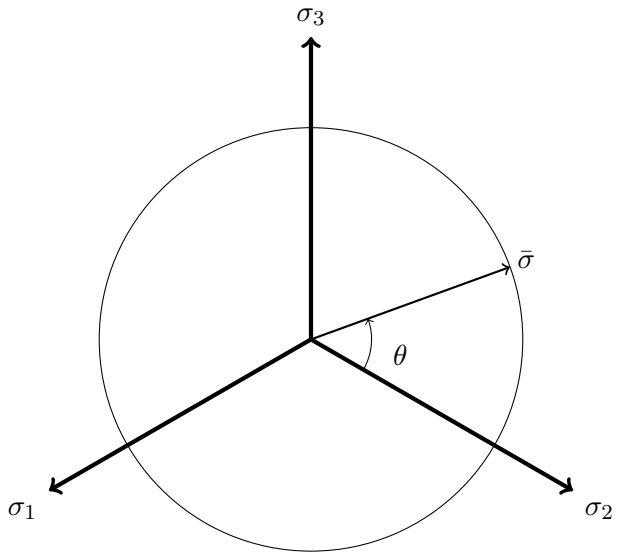

Figure 2.10: A graphical representation of the Lode angle

The circle shown in Figure 2.10 represents the yield surface for a von Mises material, where the radius of the cylinder represents the flow stress, $\bar{\sigma}$, and the Lode angle, θ, describes the ratio of the principle deviatoric stresses. Using triaxiality, flow stress and Lode angle, any point in the principle stress state can be defined, since the hydrostatic pressure is proportional to the distance along the yield surface's axis to the deviatoric plane. It was proposed that the Lode angle should be normalised in order to make the results easier to interpret, such that the normalised Lode angle ranges from -1 to 1 as shown in Equation 2.37.

$$\bar{\theta} = 1 - \frac{6\theta}{\pi} \tag{2.37}$$

Using a similar approach to the Xue - Wierzbicki model, Bai - and Wierzbicki assumed a parabolic Lode dependence, which allows for a asymmetric failure surface about the zero Lode angle line, as shown in Equation 2.38 and Figure 2.11.

$$\bar{\varepsilon}_f = \left[\frac{1}{2}\left(\varepsilon_f^{(+)} + \varepsilon_f^{(-)}\right) - \varepsilon_f^{(\circ)}\right]\bar{\theta}^2 + \frac{1}{2}\left(\varepsilon_f^{(+)} - \varepsilon_f^{(-)}\right)\bar{\theta} + \varepsilon_f^{(\circ)} \tag{2.38}$$

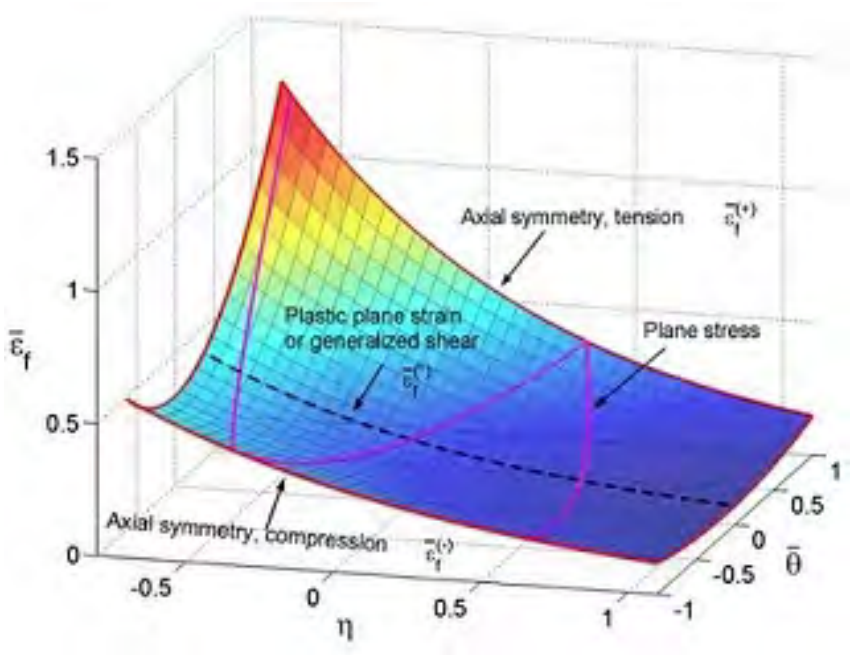

Figure 2.11: The fracture strain locus for the Bai - Wierzbicki model [8].

The functions $\varepsilon_f^{(+)}$, $\varepsilon_f^{(-)}$ and $\varepsilon_f^{(\circ)}$ represent the failure strain as a function of triaxiality along the lines of constant Lode angle representing axial symmetry in tension, axial symmetry in compression and plane strain respectively, as shown in Figure 2.11. The functions are shown in Equations 2.39, 2.40 and 2.41.

$$\varepsilon_f^{(+)} = D_1 e^{-D_2\eta} \tag{2.39}$$

$$\varepsilon_f^{(-)} = D_3 e^{-D_4\eta} \tag{2.40}$$

$$\varepsilon_f^{(\circ)} = D_5 e^{-D_6\eta} \tag{2.41}$$

2.2.3 Strain Rate Dependency

Relatively little research has been conducted into the effect of strain rate on ductile damage. As mentioned previously, Johnson and Cook incorporated strain rate and temperature into a damage model, and reported an increase in strain at fracture with increasing strain rate for OFHC copper, ARMCO iron and 4340 steel [5]. Clausen [25], Erice [26], and Kahn [27] all reported a similar strain rate behaviour for aluminium and steel.

Recently Roth and Mohr investigated the effect of strain rate on the Hosford-Coulomb fracture model for DP590 and TRIP780 steels [28], resulting in a series of fracture loci as shown in Figure 2.12. The model was calibrated using flat and notched specimens, as well as specimens with a central circular hole, at a quasistatic, intermediate and dynamic strain rates. A similar strain rate dependency function is used to that of Johnson and Cook, as shown in Equation 2.42.

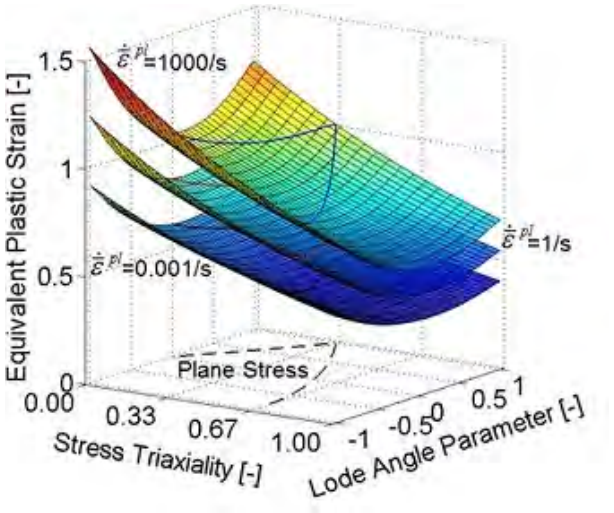

Figure 2.12: The effect of strain rate on the Hosford-Coulomb fracture model as investigated by Roth and Mohr [28]

$$f(\dot{\varepsilon}) = \begin{cases} f_0 & \text{for } \dot{\varepsilon} < \dot{\varepsilon}^* \\ f_0 \left(1 + ln\left(\frac{\dot{\varepsilon}}{\dot{\varepsilon}^*}\right)\right) & \text{for } \dot{\varepsilon}^* < \dot{\varepsilon} \end{cases} \tag{2.42}$$

The rate independent model is multiplied by the strain rate dependency function to yield an empirical version of the model incorporating strain rate effects.

2.3 The Split Hopkinson Pressure Bar

Material characterisation at high strain rates is challenging due to the fact that the inertial forces required to accelerate any parts in a testing apparatus during a test become significant when compared to the forces required to deform the specimen, and separating the two forces may be impossible for a conventional testing apparatus, even if it were possible to reach the required speeds. For dynamic strain rate tests, a split-Hopkinson pressure bar (SHPB) apparatus is used, as the apparatus is capable of recording stress-strain data for strain rates up to $1 \times 10^4 \text{s}^-1$, and any inertial effects are accounted for using one-dimensional wave propagation theory.

2.3.1 Theory

In 1914, Bertram Hopkinson developed a testing apparatus to measure the pressure history produced by a projectile impact [29]. The apparatus consisted of a suspended cylindrical steel bar with a short rod of the same radius held in contact with one end using grease, such that the tensile force holding the rod to the end of the bar was negligible when compared to the pressures measured. The other end of the bar is impacted by a projectile, resulting in a compressive pulse travelling down the length of the bar into the end piece. The pulse reflects off the end of the end piece as a tensile pulse, and since the interface between the end piece and the bar cannot withstand any appreciable tensile load, the end piece leaves the bar with a portion of the total momentum of the stress wave and impacts a ballistic pendulum such that the momentum of the end piece could be recorded. Hopkinson noted that the speed of the wave travelling through the bar was given by:

$$c = \sqrt{\frac{E}{\rho}} \quad [29] \tag{2.43}$$

With this information, the portion of the total momentum transferred to the end piece can be converted to an increasing pressure over a length of time, where the duration is equal to twice the time taken for the pressure wave to travel along the length of the end piece. By performing a number of repeatable tests with varying lengths of end pieces, the pulse length, as well as the average and peak pressures, can be inferred. Figure 2.13 shows a schematic of the apparatus designed by Hopkinson.

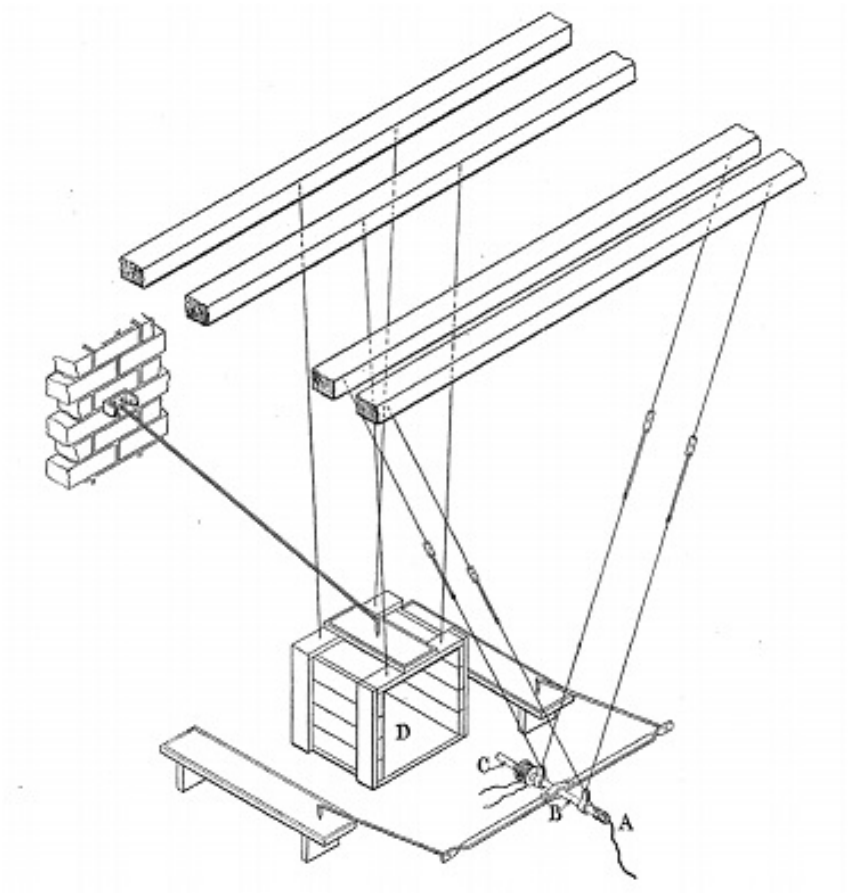

Figure 2.13: The original apparatus used by Hopkinson [29].

In 1948, Davies revisited the Hopkinson pressure bar by improving the method used to measure the momentum at the free end of the bar [30]. Using parallell plate capacitors, Davies was able to measure the small displacements of the bar's free end due to the changing pressure pulse. Making use of the fact that the velocity of the bar can be related to the stress by $\sigma = \rho c v$ [29] (where v is the particle velocity of a point in the bar), the pressure history could be inferred from the velocity history at the bar's end, which could be derived from the recorded displacement history.

The following year, Kolsky modified the apparatus for the purpose of determining the stress-strain behaviour of materials, thus creating what is now known as the Split-Hopkinson Bar apparatus [31]. The modified apparatus consisted essentially of two Hopkinson pressure bars between which a cylindrical specimen was secured. Like the apparatus designed by Davies, a parallel plate capacitor was positioned at the free end of the second bar, or output bar, to determine the stress pulse after the specimen, while a second cylindrical capacitor was introduced around the first bar, or input bar, so as to record the stress pulse before the specimen. To generate the stress pulse, a detonator was placed before an anvil which was held in place in

contact with the input bar by a collar to prevent damage of the input bar during the detonation. The apparatus is shown in Figure 2.14.

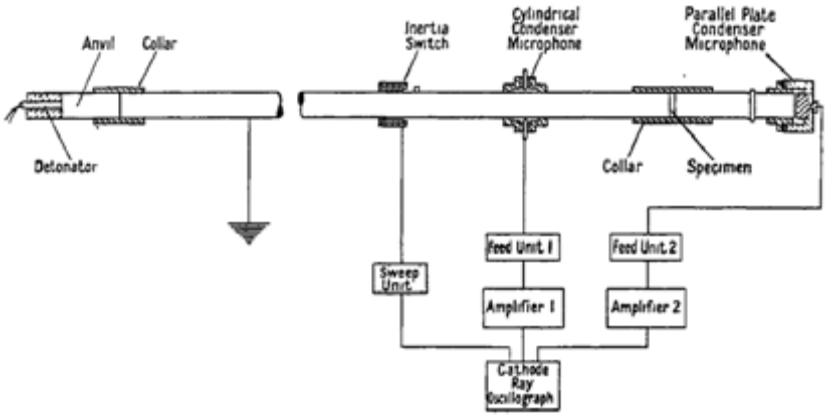

Figure 2.14: The modified apparatus designed by Kolsky [31].

The apparatus designed by Kolsky forms the basis for the modern commonly used SHPB apparatus, which is used to determine the force-displacement histories of specimens at dynamic strain rates. Knowing the wave propagation properties of the bar, the forces at either end of the specimen can be calculated assuming the wave shape remains unchanged as it propagates along the length of the bar. The time histories of the stresses at the bar-specimen interfaces can be calculated by shifting the measured strain waves forward or backward in time depending on the distance from the point of measurement to the bar end in contact with the specimen. In the input bar, the stress at the bar end in contact with the specimen is the sum of the incident wave shifted forward in time, and the reflected wave wave shifted backward in time. In order to verify equilibrium at the bar-specimen interfaces, the forces on either side of the specimen are calculated from:

$$F_{input} = A_{bar}(\sigma_i + \sigma_r) \tag{2.44}$$

$$F_{output} = A_{bar}(\sigma_t) \tag{2.45}$$

In order to obtain a force displacement curve, the displacements of the specimen end are needed as well as the forces. Using the relationship described earlier ($\sigma = \rho c v$), the stresses at the bar ends can be converted to displacements by:

$$u_{input} = \frac{1}{\rho c}\int_0^t (\sigma_i - \sigma_r)\mathrm{d}t \tag{2.46}$$

$$u_{output} = \frac{1}{\rho c}\int_0^t \sigma_t \mathrm{d}t \tag{2.47}$$

This theory and apparatus forms the basis of much of the high strain material characterisation performed today. Modern advances in electronics have allowed for strain gauges to replace the capacitors, which greatly increases the accuracy of the strain measurements in the bars, and the use of striker bars and gas-guns instead of detonators has allowed for more controllable stress pulses, however the theory and fundamental principles behind the SHPB apparatus remain unchanged.

2.4 Specimen Design

In order to calibrate some of the more complicated damage models, a variety of different test specimens are required. To calibrate the aforementioned plasticity models, a simple range of tensile tests can be performed at different strain rates. For example, for the Zhao model, four unique test configurations would be sufficient for calibration, since a quasistatic tensile test could calibrate the quasistatic parameters, another test at $\dot{\varepsilon} < 1s^{-1}$ could be used in in conjunction with the quasistatic test to determine the thermally activated parameters, and two high strain rate tests could be used to calibrate the viscous drag parameters [13]. The full calibration would only require one specimen type as four different strain rates. However, in order to calibrate the damage models, a variety of specimens are required in order to record the strain at failure for different stress states, since most models are some function of stress state history. For example, the full asymmetric Bai - Wierzbicki model requires the calibration of six different damage parameters, meaning at least six different specimen geometries are required in order to record the strain at failure for six different triaxiality - Lode angle combinations [8], without including any rate or temperature effects. This presents the challenge of designing specimens to fill the design space required to calibrate the model in question. Figure 2.15 shows how various specimen geometries fill the triaxiality - normalised Lode angle space.

Bai and Wierzbicki used three categories of specimens to calibrate their model: tensile, compressive, shear, and combined loading specimens.

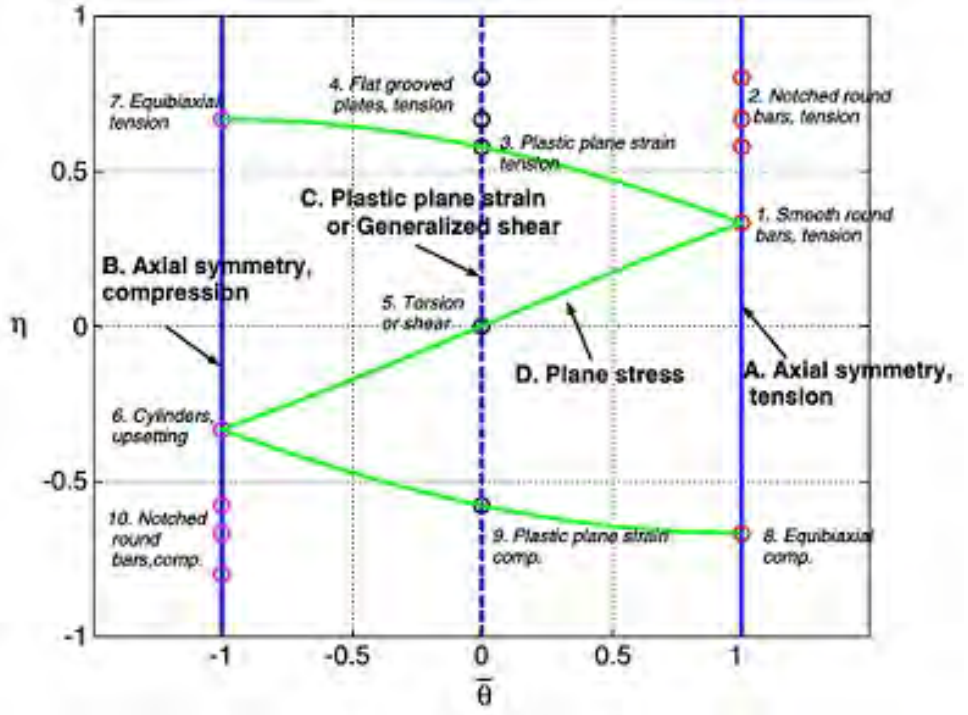

Figure 2.15: A graphical representation of the initial stress states for various specimen geometries [8].

2.4.1 Tensile

In order to obtain data for failure in the region of $\eta > 0$, straight, notched, and grooved tensile tests are used. To obtain data along the line of axial symmetry, straight and notched round bars are used, as seen in Figure 2.16a.

(a) Round specimens [8].

(b) Flat grooved specimens [8].

Figure 2.16: Tensile specimens used for damage model calibration.

The straight bars have one non-zero principle stress in the direction of tension, and hence a triaxiality of $\eta = 1/3$, whilst the notches in the bars superimpose hydrostatic stresses in the centre of the specimen, resulting in an increased triaxiality. The Bridgman formula for

estimating triaxiality in notched specimens [23] was used to estimate the initial triaxialities for the notched specimens in Figure 2.15. Bao and Wierzbicki modified the formula slightly by adding a coefficient to the logarithmic term based on numerical simulations [24]. The original and modified formulae are shown in Equations 2.48 and 2.49, where a represents the minimum radius of the specimen, and R represents the notch radius.

$$\eta = \frac{1}{3} + ln\left(1 + \frac{a}{2R}\right) \tag{2.48}$$

$$\eta_{mod} = \frac{1}{3} + 1.4ln\left(1 + \frac{a}{2R}\right) \tag{2.49}$$

Additionally, flat grooved plates were used to create a plane strain condition at the centre of the plate, since the relatively large lateral dimension limit the strain in the lateral direction. The grooves have a similar effect to the notches in increasing the triaxiality, as seen in Figure 2.15. The Bridgman formula was modified by Bai et. al. [32] for the application of grooved specimens as opposed to round notched specimens as shown in Equation 2.50, where t represents the minimum specimen thickness, and R the groove radius.

$$\eta_{mod} = \frac{\sqrt{3}}{3}\left[1 + 2ln\left(1 + \frac{t}{4R}\right)\right] \tag{2.50}$$

2.4.2 Shear

In order to fully calibrate the triaxiality dependence of fracture along the line $\bar{\theta} = 0$, a shear specimen is required, since pure shear corresponds to $\eta = 0$. Bao and Wierzbicki [22] developed the specimen shown in Figure 2.17, which was designed to deform in a localised area in pure shear. The gauge section was thinned down and flared at the edges in a "butterfly" configuration to ensure shear localisation in the middle of the gauge section.

A drawback of this specimen is that areas of localised stresses form in the gauge section, as shown in the simulation in Figure 2.18, which are not necessarily in a state of pure shear. This increases the difficulty of determining where failure occurred, and whether the onset of fracture was under pure shear stress. However, a qualitative analysis of the specimens post-testing did indicate that the dominant fracture mechanism was shear decohesion, as seen in the magnification of the gauge section in Figure 2.17.

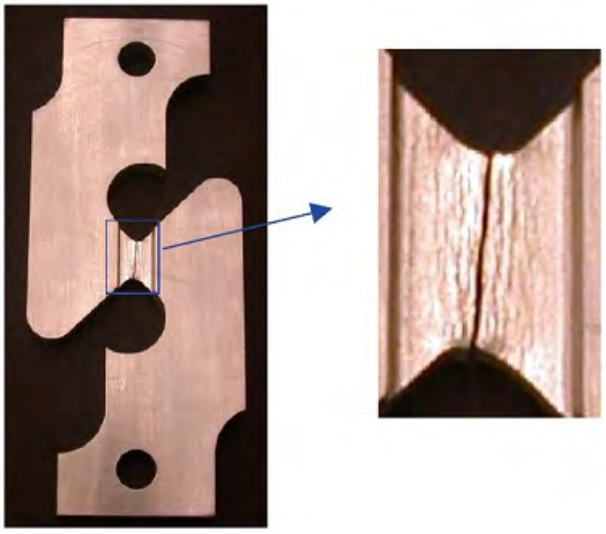

Figure 2.17: The pure shear specimen used by Bao and Wierzbicki [22].

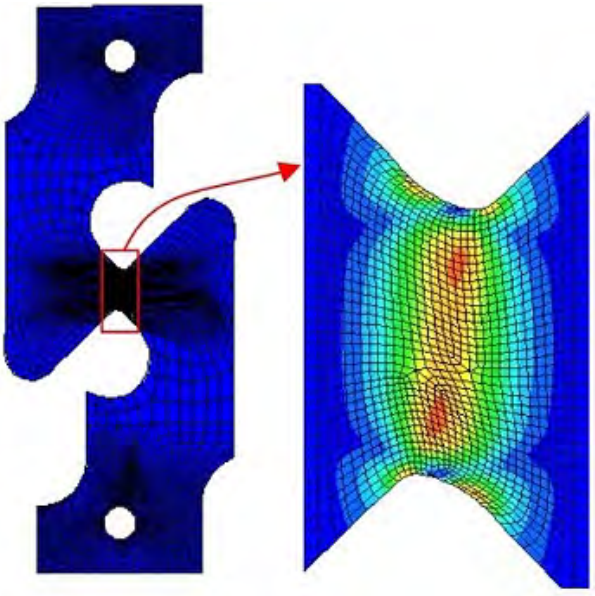

Figure 2.18: Localised stresses in a deformed shear specimen [22]

2.4.3 Combined

Combined loading specimens deform under stress states which lie off the lines of plane stress, plane strain and axial symmetry. Recording fracture behaviour under these conditions is useful for ensuring the accuracy of the fracture locus. An example of a combined loading specimen is that used by Bao and Wierzbicki in Figure 2.19. The gauge section deforms under a combination of shear and tension, meaning that providing the specimen is thin enough, the Lode angle and triaxiality will lie on the line of plane stress somewhere between the line of axial symmetry and plane strain.

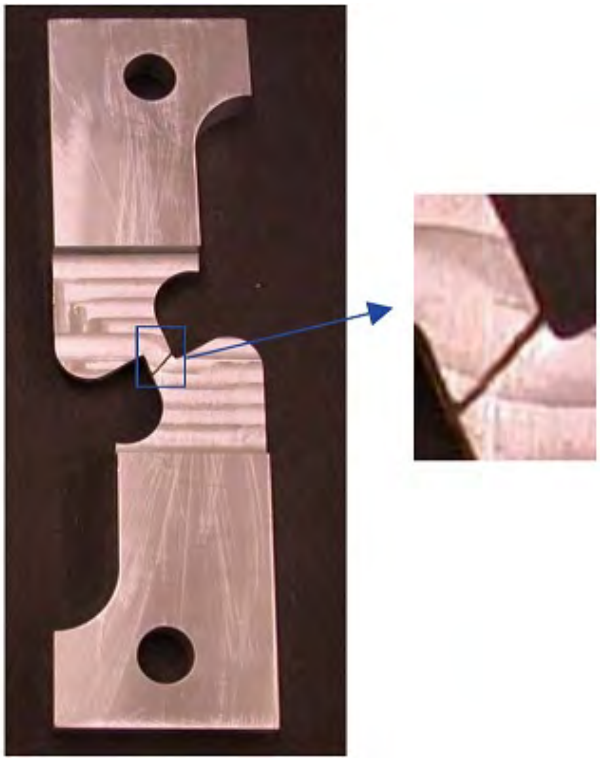

Figure 2.19: A combined loading specimen used by Bao and Wierzbicki [22]

Another example of combined loading specimens, is the "butterfly" specimen developed by Mohr, as described in [33–35]. The specimens require specialised a biaxial loading apparatus, which is only suitable for testing at quasistatic rates. The name "butterfly" comes from the flared edges of the specimen gauge section which ensures that the stress is concentrated along the centre of the gauge section and not at the edges, thus preventing premature failure away from the specimen centre. Figure 2.20 shows a butterfly specimen designed in 2011 by Dunand and Mohr [35].

Notice the gauge section's shoulder is curved with radius R_s, whilst the lateral boundaries are also curved with radius R_l. The radius at the lateral boundaries is introduced to minimise the plastic strain at the specimen boundary.

2.4.4 Tensile SHPB Specimens

A challenge in testing the required specimens at dynamic strain rates is that the specimen must be designed for use in a tensile SHPB system. These specimens are typically several times smaller than the specimens traditionally used with a quasistatic tensile testing apparatus, and often require complex geometries in order to be secured to the bars. Designing a specimen

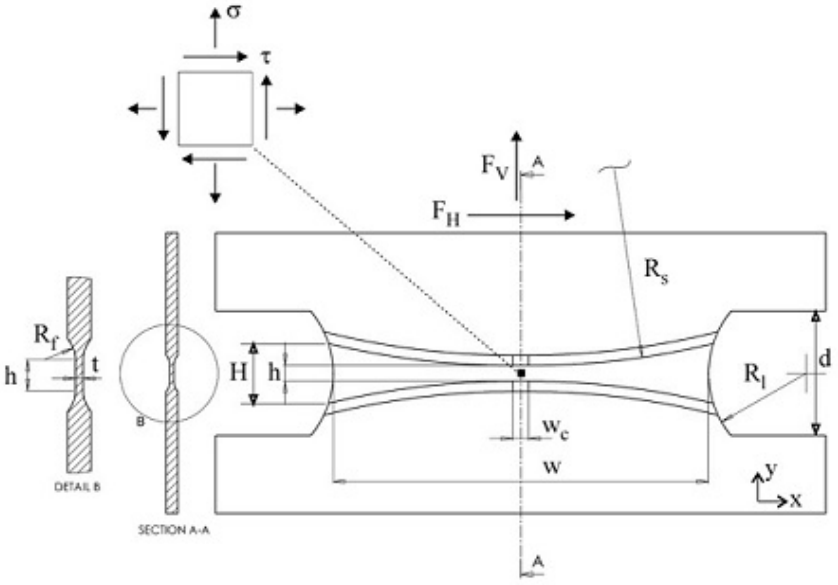

Figure 2.20: The butterfly specimen used by Dunand and Mohr [35]

and a securing mechanism capable of keeping the specimen secured to the bars during testing while providing minimum obstruction to the wave propagation from the input to output bars provides a unique challenge. A brief summary the various commonly used tensile SHPB systems is outlined below, ordered by the methods used.

Using the reflected pulse

In 1960, Harding et. al. used a tube and yoke apparatus to generate tensile deformation in a specimen using a compressive stress pulse [36]. The apparatus consists of a hollow cylindrical loading tube, inside which two pressure bars are coaxially aligned. The input bar is attached to the free end of the tube, and a specimen is connected between the bars via thread. A compressive pulse is generated in the loading bar, and the reflected tensile pulse travels through the input bar and deforms the specimen. In 1982 Ellwood et. al. [37] simplified this system by using a steel collar placed between the input and output bar with a specimen threaded into the bars as shown in Figure 2.21.

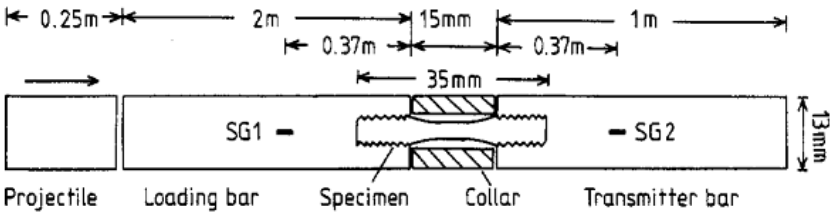

Figure 2.21: The tensile apparatus used by Ellwood et. al. [37].

The collar prevents the specimen from deforming plastically during the incident compressive pulse, and since a tensile load cannot be sustained between the collar and the bars, the collar does not restrict the tensile deformation of the specimen resulting from the reflected pulse.

The problem with this method is that the incident compressive pulse will not pass perfectly through the collar and specimen, resulting in a premature reflected wave which may interfere with the signals of interest. It is also difficult to control the shape of the incident tensile pulse, as the shape of the original compressive pulse changes due to both the reflection caused by the compressive pulse passing through the collar and the development of dispersion as the pulse travels along the length of the bars. Dispersion is the change of the pulse shape caused by the different frequency components of the pulse moving at slightly different wave speeds [38].

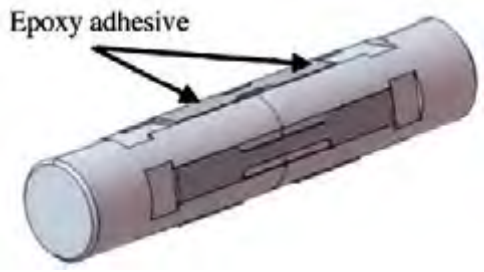

Figure 2.22: The specimens used by Haugou et. al. [39].

Haugou et. al. addressed the first problem by using four specimens glued symmetrically to the outside of the bars [39] as shown in Figure 2.22. Having the input and output bars in contact reduces the problem of spurious reflection as the compressive pulse passes the specimens, although the grooves machined into the outer surfaces of the bars still results in a small impedance mismatch. However, this solution does not solve the problem of excessive dispersion, and the multiple specimens makes extracting the individual load histories difficult, resulting in a loss of quality of data.

Inverting a compressive pulse

Another method used is to design the specimen or testing apparatus such that the specimen will experience tensile deformation using a compressive pulse. As early as 1968 Lindholm and Yeakley [40] designed a "hat-shaped" specimen, as shown in Figure 2.23, which consisted of a tube shaped specimen with a flange such that it could be seated within a tubular output bar. The deformation occurs in the walls of the specimen, as shown by the gauge length label L_0.

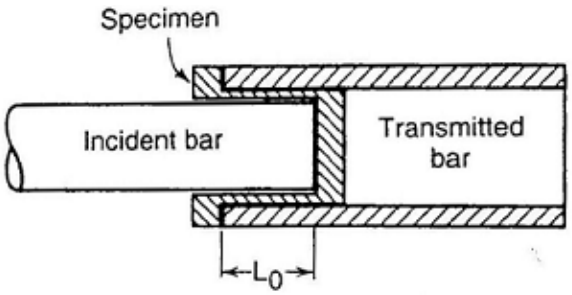

Figure 2.23: The "hat-shaped" specimen designed by Lndholm and Yeakley [40].

Although this method allows for relatively minor modifications to the SHPB apparatus, it does not allow for the testing of sheet metal specimens, and the results are difficult to analyse due to the complex specimen geometry.

A similar concept which did not require a hollow output bar is the "M-shaped" specimen designed by Mohr and Gary [41] (Figure 2.24).

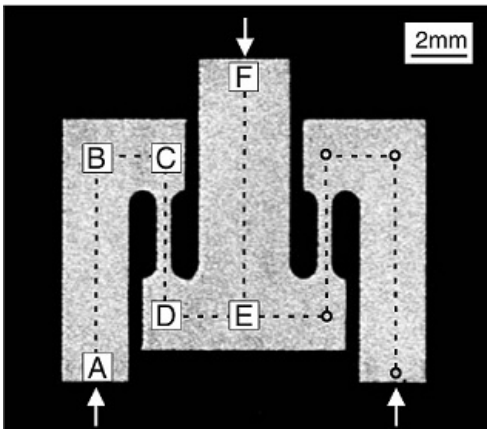

Figure 2.24: The "M-shaped" specimen designed by Mohr and Gary [41].

The solution is elegant as it does not require any mechanism to secure the specimen to the bars, but the convoluted loading path through which the incident pulse must travel makes it difficult to maintain quality of data, and the specimens do not lend themselves to ease and economy of manufacture.

Dunand, Gary and Mohr developed another load inversion technique [42] consisting of a pusher in contact with the input bar (shown in green in Figure 2.25) to which the specimen is attached at the opposite end via screws, as well as a stirrup (shown in red) in contact with two output bars to which the specimen is also attached.

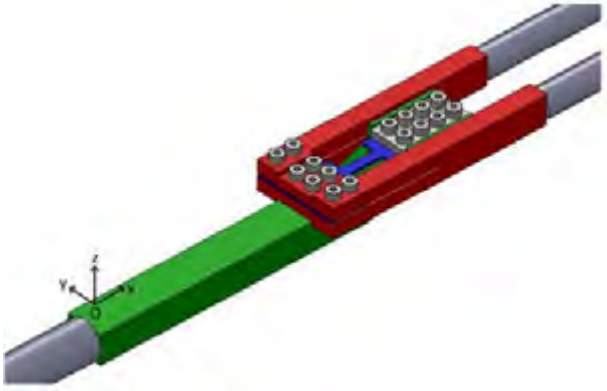

Figure 2.25: The load inversion device designed by Dunand, Gary and Mohr [42].

The solution allows for easy manufacture of sheet specimens, but the load inversion device results in a significant impedance mismatch at the specimen interface, which negatively affects the quality of data produced.

Directly generating a tensile pulse

While the techniques discussed in the preceding sections all involve the inversion of a tensile pulse, an alternative method of performing tensile tests using a SHPB apparatus, is to directly generate a tensile pulse in the input bar. However, the focus of this thesis is not how such a pulse is generated, but rather the various methods used to secure the specimens to the bars. The method used to generate a tensile pulse in the input bar is discussed in Section 3.3.1.

The majority of techniques currently employed use thread, glue, or a combination of the two to secure the specimen. An example of this is the design by Eskandari and Nemes [43], which consists of an aluminium fixture that is threaded onto the input and output bars, into which the specimen is glued, as illustrated in Figure 2.26.

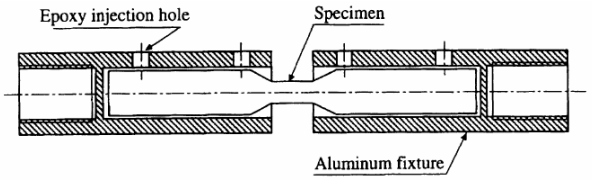

Figure 2.26: The specimen fixture design by Eskandari and Nemes [43].

A similar design was proposed by Gómez-del Río et. al. [44], which consisted of two fixtures with slots, into which a sheet specimen can be glued, that threaded directly into the bars. However, both these methods result in large impedance mismatches at the bar-specimen interfaces due to

the fixtures used, as well as time-consuming preparation processes due to the gluing required, which is undesirable.

A different approach without the use of glue is proposed by LeBlanc and Lassila [45], which also makes use of a fixture threaded into the bars, but uses a clamping mechanism with pins to secure the specimen, as shown in Figure 2.27a. A similar mechnism was employed by Koh et.al. [46], as seen in Figure 2.27b.

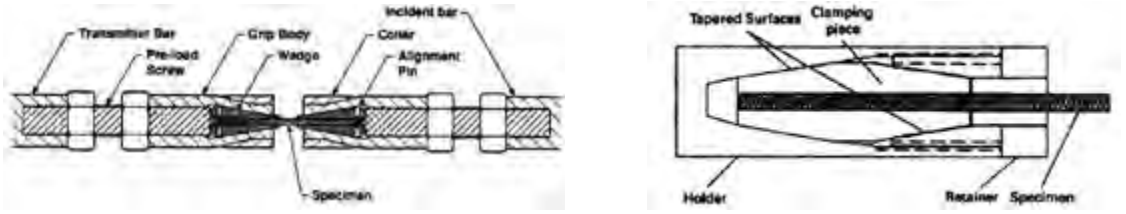

(a) The clamp assembly employed by LeBlanc and Lassila [45].

(b) The specimen clamp mechanism employed by Koh et. al. [46].

Figure 2.27: Securing tensile SHPB specimens via a clamping mechanism

The clamping mechanism in Figure 2.27a, consists of wedge grips surrounded by a tapered casing, onto which a collar was screwed. By tightening the collar onto the taper, the taper angle tightens the clamps onto the specimen. A similar concept holds for the mechanism proposed by Koh et. al., but again these fixtures result in a significant change in impedance due to the extra mass of the clamping mechanisms.

To avoid spurious reflections due to fixtures, a method of attaching the specimen directly to the bars can be used. A successful technique used by Wang and Xia [47], and later by Peirs et. al. [48], is to glue the specimen directly into the bars. Sheet specimens are designed with large grip sections that can be inserted and glued into slots in each bar (see Figure 2.28).

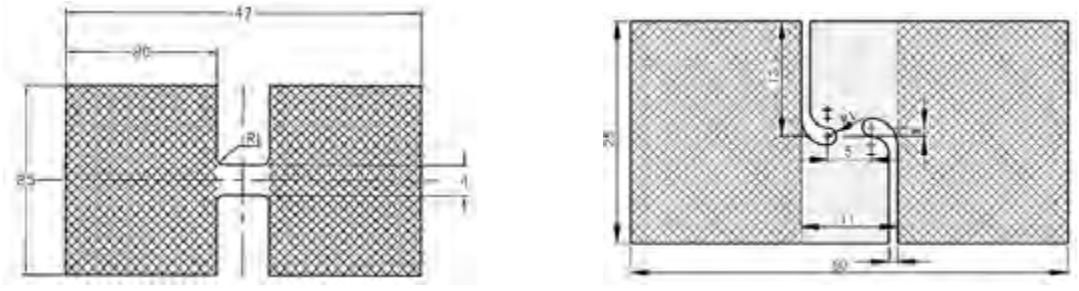

(a) Tensile.

(b) Shear.

Figure 2.28: The specimens used by Peirs et. al. The hatched area represents the glued zone [48].

This technique has been shown to produce accurate and repeatable results in terms of equilibrium at the specimen interface and quality of signal recorded, however the gluing processed

required between each test is time consuming and does not lend itself to routine testing. The impracticalities aside, the technique produces good results, and is well suited to more complex geometries with sheet specimens, such as the shear specimen seen in Figure 2.28b.

In summary, while clamped fixtures are convenient for routine testing, they lead to spurious reflections which interfere with the signal used for analysis. Glued slots in the bars provide the best quality of data, but are tedious to use due to the excessive time needed between tests. The specimens and fixtures used in this dissertation aim to find the best possible compromise between convenience and quality, and are described in Section 3.1.1.

Chapter 3

Experimental Method

In order to accurately calibrate any damage model, a number of tests must be designed to fill the design space required for calibration. Based on the options presented in Section 2.2, the Bai-Wierzbicki model is chosen to be calibrated at three different strain rates in order to study the effect of strain rate on the damage model. The chosen material is DOMEX 355MC high strength steel, as the material properties are consistent from batch to batch, and high strength steels are often used in protective structures, which is relevant to BISRU's scope of research. Quasistatic tests were performed using a Zwick static material testing machine, while the dynamic tests were performed using a tensile split Hopkinson Pressure Bar (SHPB) apparatus. In order to determine the triaxiality, Lode angle, strain rate and plastic strain locally at the point of fracture, numerical simulations were run to represent the experimental tests. The experimental procedure is shown in Figure 3.1 for a single strain rate.

This section outlines the information and techniques required to perform the experiments upon which the damage model is based.

3.1 Specimen Design

The scope of this dissertation is limited to uni-axial tensile tests, meaning the calibration of the damage model is limited to only one quadrant of the triaxiality-Lode angle plane. In order to obtain data over a sufficient range of triaxialities and Lode angles, straight, notched and grooved specimens are used, which are all designed to be used in the tensile SHPB apparatus.

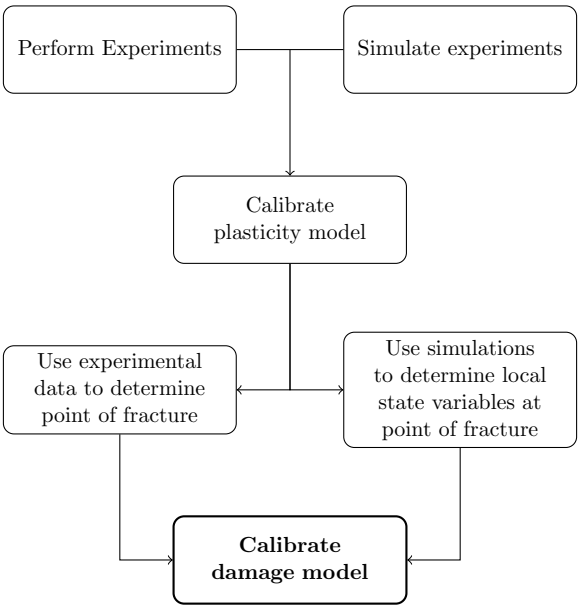

Figure 3.1: The procedure used to calibrate the proposed damage model.

Although larger specimens could be used for the quasistatic tests, the same specimens are used for both the Zwick and SHPB tests to eliminate any scaling effects which may be present.

3.1.1 The Fir-Tree Specimen

In order to secure the specimens into the input and output bars for the SHPB tests, a clamping design is required which will enable routine testing without sacrificing the quality of the data produced. Routine testing implies that a large volume of tests can be performed with a quick turn around between tests and good repeatability, for which the following requirements apply:

- Cost effective specimen manufacture. This is necessary in order to produce as many specimens as possible.
- Ease, versatility and accuracy of manufacture. In order to produce specimens in as short a time as possible, the specimen manufacture process must be as simple as possible, but accurate enough to ensure quality and repeatability of data. Additionally, the results must be reproducible using a number of different manufacturing processes, ensuring the design is accessible.
- No gluing required. The gluing process requires too much time between tests to be considered routine. The gluing and removing of specimens is time consuming, and requires considerable operator experience to reproduce results precisely from test to test.

Furthermore, in order to ensure the best quality of data possible, the following design features are required for the clamp and specimen.

- Minimum additional mass. This requirement is crucial as any additional mass will affect the impedance matching of the SHPB apparatus, which has an effect on the transmitted and reflected signals recorded. Since all forces on the specimen are inferred from the incdident, reflected, and transmitted signals in the bars, it is imperative that the change in geometry and mass of the bars at the specimen interface is minimal.
- No play between specimen and clamp. In order to ensure that the specimen enters a state of quasi-equilibrium as soon as possible, any play between the clamping mechanism and the specimen must be removed, as any relative movement between clamp and specimen will result in unequal forces at the input and output bar interfaces.
- The clamping mechanism must not rely on friction. Friction joins, in general, are not reliable under mechanical shock and impact conditions, such as those encountered during SHPB testing.
- Smooth load transfer from bar to specimen. High stress concentrations in the bar and specimen must be avoid to ensure the quality of signal transmitted from the input bar to the output bar, as well as to prevent the specimen, or even the bar, from plastically deforming outside the gauge section.
- Maximum clamping force on specimen. This is a requirement unique to the use of a clamping mechanism. In order to eliminate play using a clamping mechanism, the clamping force between the clamp and specimen must be as large as possible.
- Self-centering. Since the SHPB theory relies on one-dimensional wave propagation theory, the stress pulses in the bars must be axially symmetric, meaning the bars and specimen must all be axially aligned. Therefore any clamping mechanism must ensure axial alignment between the clamp and bars, as well as the clamp and specimen during its use.

From these requirements, the “Fir-Tree” specimen and clamp pair has been developed at BISRU, consisting of tapered, threaded clamps into which a lobed specimen is seated, as shown in Figure 3.2.

The design exhibits two main distinguishing features, the tapered, threaded clamp and a lobed specimen. The tapered thread design is chosen for several reasons:

Figure 3.2: The clamps used to secure the specimens in the Split Hopkinson Bar.

- The taper angle generates larger, more uniform clamping forces than could be generated using bolts within the size and mass constraint of a SHPB, due to the hoop forces generated in the bar as the thread is tightened. Unlike straight thread, as the conical thread is tightened, the change in thread diameter causes radial and hoop strains in the bar. The resulting stresses in the bar increase the clamping force on the specimen, much like a collet. Like a collet, grooves are machined into the clamp to allow for a certain amount of radial expansion or contraction. This is an elegant solution, as no extra apparatus is required to ensure adequate clamping force on the specimen, which means that the mass of the clamps is also kept to a minimum.

- The thread mechanism is inherently self-centering due to the taper angle. Because the fit between the male and female parts becomes progressively tighter, the clearance between the parts decreases, ensuring that the clamp and bar centres are aligned.

- Since the load transfer across the thread is not perfect, using a straight thread results in a sudden high stress concentration in the threaded section of the bar due to the reduced bar area, even for bars and clamps of the same material. The conical shape of the clamps allows the stress pulse transfer between the bar and the clamp thread to be more gradual, as the area of the bar begins to change linearly as the stress pulse reaches the clamp, resulting in a smoother transfer between bar and clamp, as well as clamp and specimen.

- The clamp design is simple to manufacture, as each clamp is manufactured from a single piece of titanium, using only wire-cutting and CNC milling processes.

The lobed, fir-tree shape of the clamped region of the specimen is inspired by turbine blade roots, which have a fir-tree shape to ensure even contact between the male and female parts, and reduce stress concentrations by producing a smooth and uniform load transfer between the rotor and blade root in high creep environments. As mentioned above, the taper angle results in a smooth load transfer between clamp and specimen. However, there are further consequences of using such a shape for application in a tensile SHPB apparatus:

- The tapered shape of each lobe ensures that as the clamp is compressed during tightening, each lobe will seat properly in the clamp. This means that two face contacts are guaranteed for each lobe, which minimises local stress concentrations due by removing any point contacts, and promotes equal loading for each lobe. The radius of the end of each lobe on the specimen is slightly larger than that in the clamp, and the converse is true at the base of each lobe. This ensures that contact occurs on the flat section of each lobe and not on the radii.

- The radii of the lobes further reduce stress concentrations and create a more equal stress distribution throughout the clamped section of the specimen. This is important to ensure the specimen does not plastically deform in the clamped region, and to obtain the best stress pulse transfer possible.

- The lobe to clamp contact mechanism ensures minimal play between the two, since each lobe is seated correctly as described above, and the conical shape of the clamps will ensure that the clamp will tighten sufficiently to locate the specimen.

In addition to these fundamental design features, certain features were motivated by practical considerations. In order to allow the clamps to contract sufficiently during tightening, grooves are cut parallel to the axis of the clamp as seen in Figure 3.2. This allows for small offset errors during the machining of the specimens ($\pm$0.1mm), providing the angle and radii of the lobes are correct. If the specimen is too large, the grooves allow for a certain amount of expansion of the clamp, whereas if the specimen is too small, the clamp will contract to grip the specimen during tightening. The three grooves allow the clamp halves to expand and contract asymmetrically, much like and independent four-jaw chuck, ensuring the specimen is centered within the clamp. The grooves also allow the clamps to snap onto the specimen, which increases the ease of handling during assembly and testing. The chosen clamp material is titanium, since it is the lightest metal next to aluminium, but generally exhibits greater strength and hardness,

which is important as the thread must not deform over repeated use. Additionally, by using dissimilar materials for the bars and clamps, any potential binding between the bars and clamps is prevented. Finally, a tool was designed to tighten the clamps. The tool needs to ensure that the clamp halves tightened evenly in order for the specimen to seat correctly. Additionally the tool must fit around the specimen during tightening. This is achieved by drilling four holes in the clamp, into which a tool with four pins can fit, as shown in Figure 3.3

Figure 3.3: The tool and clamps with holes drilled for use with tool.

3.1.2 Specimen Geometries

In order to calibrate the damage model for $0 \leq \eta \leq 1$ and $0 \leq \bar{\theta} \leq 1$, a straight specimen and three notched specimens are used to obtain data near the line $\bar{\theta} = 1$, while grooved specimens are used to obtain data near the line $\bar{\theta} = 0$. The notched and grooved specimens are designed based on the "Fir-tree" specimen. The notched specimen has a radius machined into the sides of the gauge section, whereas the grooved specimen is wider than the standard specimen to give enough width to result in a plane strain condition at the centre of the groove. Refer to Appendix C for more detailed drawings of the specimens. Figure 3.4 shows estimations for the different triaxialities and normalised Lode angles obtained from the empirical formulae outlined in Section 2.4, where the groove and notch radii range from 1.5mm to 5.0mm.

Note that the triaxiality of the grooved specimens is more closely grouped than that of the notched specimens. However, in practice, all of the triaxialities will be different, as the stress state evolution is affected by the change in geometry caused by local necking in the specimen. This usually results in an increase in triaxiality locally in the middle of the specimen gauge section. Since the grooves with smaller radii deform in a smaller local area, the change in triaxiality is greater throughout the test, meaning that in practice the spread of triaxialities for the different groove radii is greater than the estimates for the initial triaxialities. The notched and grooved specimens are designed such that the minimum specimen thickness is the same for each specimen, where the minimum thickness is 2mm for the notched specimens, and 1mm for

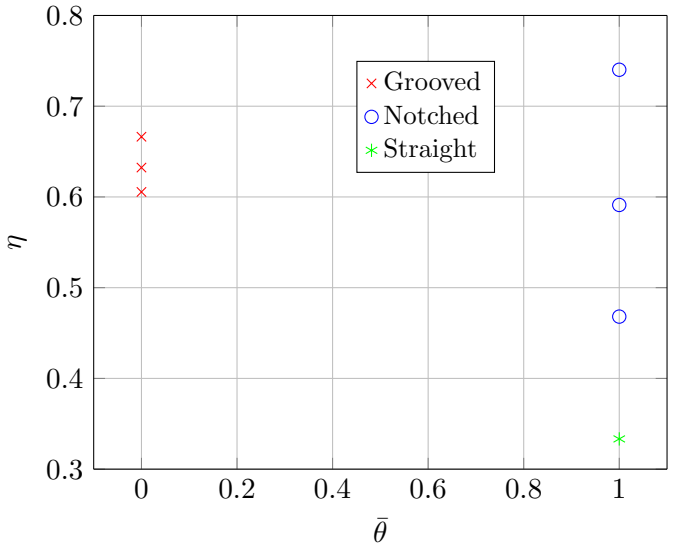

Figure 3.4: An estimate of the initial stress states for the different specimen geometries.

the grooved specimens. The minimum groove radius is determined by the minimum diameter cutter available, whereas the maximum radius is limited by the gauge length of the specimen.

The manufactured specimens are shown in Figure 3.5.

Figure 3.5: The notched, straight and grooved specimens.

For each strain rate, four specimens of each geometry are tested to ensure repeatability.

3.2 Quasistatic Zwick Tensile Tests

For quasistatic strain rate regime testing, the Zwick static material testing machine was used at crosshead displacement rates of 0.6 mm/min and 100 mm/min. The faster speed was selected based on the limits of the testing machine. Traditionally, standard dogbone specimens are used for quasistatic tests. However in order to ensure that no scaling effects would affect the results over the different strain rate regime, the same specimens were used for the quasistatic testing as for the dynamic testing. This meant an adaptor had to be made to clamp the specimens designed specifically for the tensile SHPB apparatus. The adaptors consists of two cylinders, into which the specimen clamps can be screwed, as seen in Figure 3.6, with holes for pins which attach each adaptor to the Zwick crosshead.

Figure 3.6: A specimen loaded in the Zwick tester

Because the specimen clamps had to be screwed into the adaptors a rose joint was used on the top adaptor to allow for rotational alignment, as well as to ensure no bending loads were present on the specimen. However, the number of adaptors used meant that the test fixture compliance is of a comparable magnitude to that of the specimen, and so corrections must be made to remove the test compliance. This means that the elastic compliance of the specimen is also removed from the data, but since the elastic strain is very small in comparison to the

plastic strain, this is not an issue. Figure 3.7 shows the original and adjusted force-displacement data from a Zwick test.

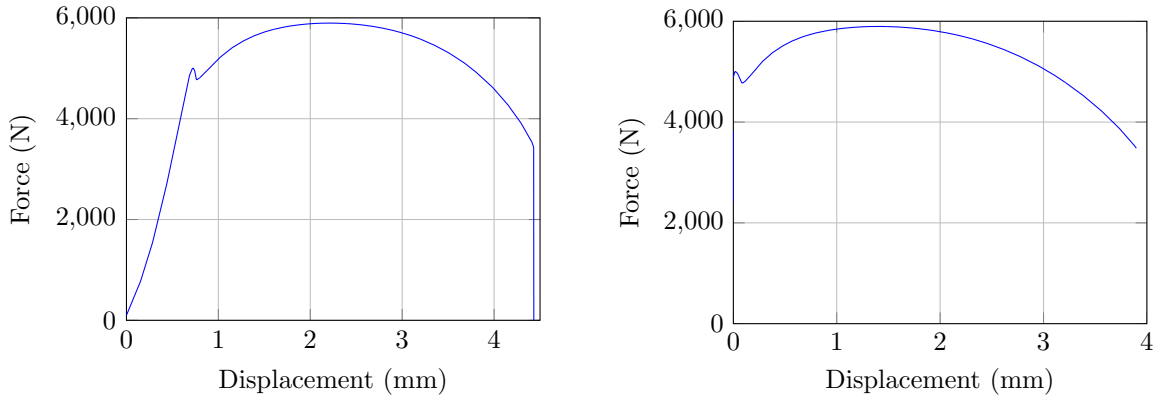

(a) The raw Zwick data.

(b) The adjusted Zwick data.

Figure 3.7: The raw (a) and processed (b) force-displacement data from a Zwick test.

Note that in the raw data there is an initial take-up period before the test enters a linear-elastic regime. By selecting a portion of the data within the linear region, the test stiffness can be calculated, and the elastic portion of the displacement can then be removed knowing that the force at any point during the test must be proportional to the test stiffness. Since the test has a small preload, the force can be calculated as:

$$F = k_{test} \times d_e + c \tag{3.1}$$

where k_{test} is the test fixture stiffness, d_e is the displacement due to elastic deformation, and c is a constant to take into account the preload. With this relationship, the displacement due to plastic deformation at any point may be calculated as:

$$d_p = d_{total} - \frac{F - c}{k_{test}} \tag{3.2}$$

This processed data is now useful for estimating parameters for plasticity models and comparing finite element simulation outputs.

3.2.1 Zwick Machine Challenges

The quasistatic strain rate tests generally show consistency in the results, particularly for the 0.6 mm/min tests, both in the force-displacement behaviour and the point of fracture. However,

two problems which arose were the need to account for the compliance of the Zwick tensile test machine, and the inertia of the Zwick machine when testing at faster speeds.

Accounting for the compliance was necessary due to the relatively low stiffness of the load path in the apparatus in comparison to the specimen. Because a chain of adaptors were required to secure the specimen in the Zwick apparatus, the effective stiffness of the test was lowered, which means that the portion of the displacement measured due to elastic compliance is not negligible in comparison to that due plastic deformation. This was especially noticeable for the grooved specimens where the portion of displacement due to elastic deformation is compliance than its plastic counterpart. Figure 3.8a illustrates the difference in the measured displacement for a R1.5 mm grooved specimen using the extensometer and the crosshead, while Figure 3.8b shows the difference in the force-displacement data obtained for the two cases after correcting for elastic deformation. Not that because the strain in the grooved specimens in localised, these specimens yield the most exaggerated results.

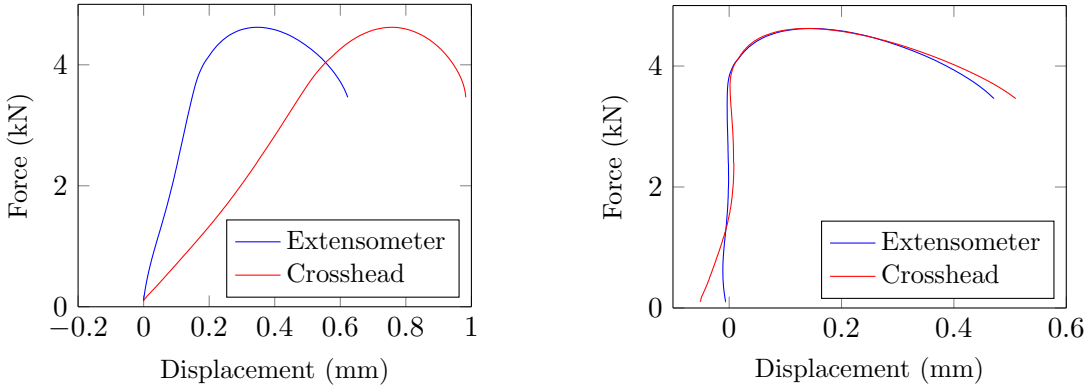

(a) Measured displacements.

(b) Corrected displacements.

Figure 3.8: An illustration of the difference in results obtained using an extensometer and the Zwick crosshead displacement.

Notice that the displacement obtained using the extensometer is significantly less than the crosshead displacement, and the force-displacement curve obtained during the elastic deformation regime is more linear. This results in a more accurate stiffness value used to remove the elastic component of deformation from the data, which can be seen in Figure 3.8b, where the linear region of deformation in effectively vertical for the data obtained using the extensometer, but non-linear for the data obtained using the Zwick crosshead. Although the two curves are visually very similar, the small difference in displacement at failure can yield a large difference in the local variables at failure obtained from the finite element simulations. Unfortunately the data obtained using the extensometer was very inconsistent due to the difficulty of securing

the extensometer to the specimen adaptors, hence the crosshead displacement data was used. It should be noted that this may be a source of some of error, particularly for the grooved specimens, where the least consistency in results is observed.

Running the Zwick testing machine at 100 mm/min poses an additional challenge due to the inertia of the tensile testing machine. Figure 3.9 shows the time history of the crosshead displacement for a R1.5mm grooved specimen tested at 100 mm/min.

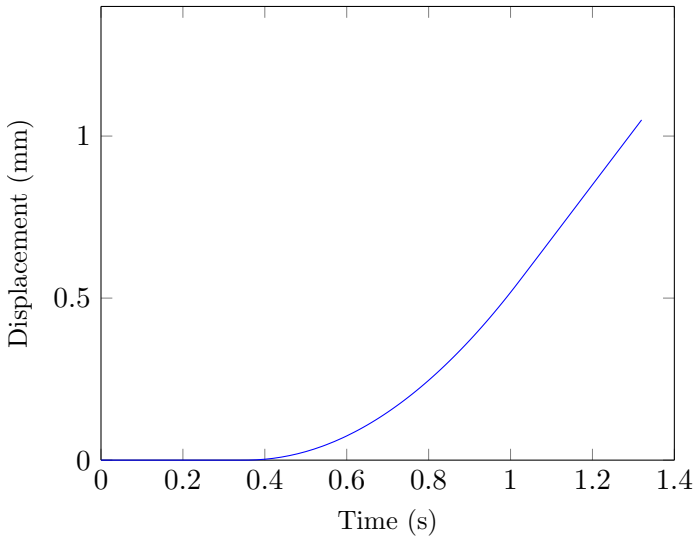

Figure 3.9: The time history of a 100 mm/min test for a R1.5mm grooved specimen, illustrating the time taken for the Zwick to reach maximum speed.

It is evident that the time taken for the crosshead to reach maximum speed is a significant portion of the test duration, as yielding occurs at a displacement of approximately 0.7 mm, meaning that the test can no longer be considered a constant speed test. Another problem which arose was that the chosen sampling frequency of the testing machine was not high enough to capture the deformation behaviour close to yield. The total duration of the plastic deformation for the test shown in Figure 3.9 is approximately 0.6 seconds, and since the sampling frequency was set at 50 Hz for all the tests, only ± 80 data points were recorded during the plastic deformation period. This is especially problematic during localised necking and failure, which occurs very quickly relative to the duration of rest of the deformation, meaning that the data acquisition unit only recorded approximately half the deformation profile of the test, as the necking process occurred faster than the sampling period. For this reason the data from 100 mm/min grooved specimen test was not used. This issue could possibly be resolved by testing at crosshead speeds in the region of 20 mm/min or less, which would still yield local strain rates similar to that of the straight specimens.

3.3 Tensile Split Hopkinson Pressure Bar

The conventional SHPB apparatus allows for compressive tests at high strain rates. However, in order to study fracture in metals at high strain rates, the apparatus must be adapted to be compatible with tensile testing. The steps taken to achieve such compatibility, as well as the procedure used to capture and process the test data are outlined below.

3.3.1 Tensile Modification

In order to perform tensile SHPB tests, two challenges must be overcome:

- securing the specimen between the bars.
- generating a tensile pressure pulse in the input bar.

The specimens are secured using a novel design described in Section 3.1.1, and a tensile striker configuration developed at BISRU [9, 49], is used such that a gas gun for use with a compressive test can be used, as described in this Section. The basic principle of the tensile striker configuration used involves firing a tubular striker at a collar secured to the input bar, as demonstrated in Figure 3.10.

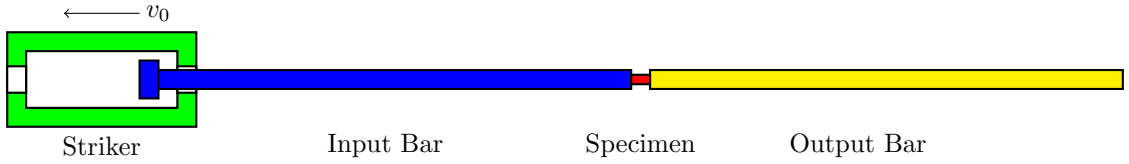

Figure 3.10: A schematic of the tensile adaptor used with the SHPB apparatus.

In order to generate the initial velocity of the striker using a gas gun designed for use with a compressive test apparatus, a modified barrel is used, around which the striker is positioned. The barrel has holes drilled radially near its end, and a plug at the end preventing air from travelling further down the striker. Pressurised air escapes from the holes, pressurising the volume of the striker surrounding the barrel before the plug. A pressure cap on the end of the striker prevents air from leaking between the striker and barrel allowing pressure to build, and experiences a force from the increased pressure, causing the striker to move back towards the gas gun. A schematic of the system is shown in Figure 3.11.

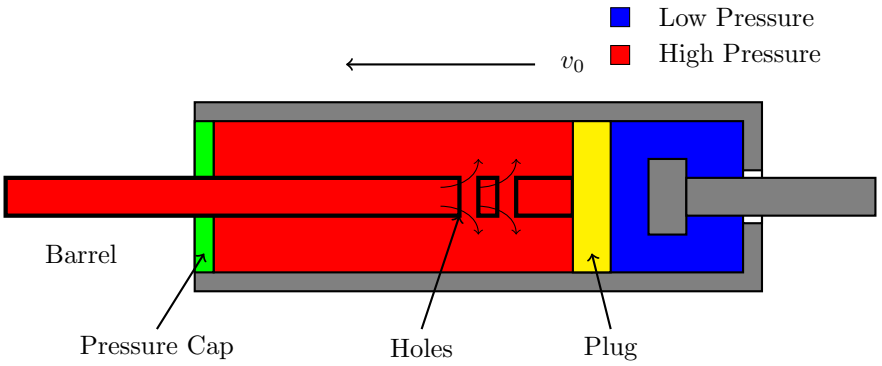

Figure 3.11: A schematic of the tensile adaptor mechanism.

The area of the tubular striker is chosen such that the ρcA value, or the mechanical impedance, of the striker is less than or equal to that of the input bar, which ensures the striker will remain stationary or rebound after impact. This is necessary to produce a square stress pulse, otherwise the striker would remain in contact with the input bar after the initial stress pulse had developed, resulting in a pulse with stepwise-decreasing plateaus. The length of the striker is chosen such that the generated pulse is close to, but less than half the length of the input bar. The pulse should be as long as possible in order to ensure the specimen strains to failure, but must be less than half the length of the bar to prevent interference between the incident and reflected pulses. Since the length of the input bar is 3.66m, the striker could theoretically be up to 1.83m long, since the wave speed in the striker is the same as that in the input bar. However, in practice the generated pulse has a finite rise time, and so the pulse lasts slightly longer than expected. Consequently, a striker length of 1.29m was used.

3.3.2 Calibration

In order to convert the recorded voltage signals from the strain gauges to stresses in the bars, the test apparatus must be calibrated. The calibration involves determining the wave speed of the bars, as well as a calibration factor to relate the measured voltage to stress, such that:

$$\sigma = KV_{read} \tag{3.3}$$

In order to determine the wave speed of a bar, careful measurements of the lengths, diameters, and masses of each bar and a striker must be taken, before the striker is fired at each bar separately. Note that the bars are calibrated using a compressive stress pulse in order to

accurately measure the impedance and velocity of the striker. A small ball of putty is placed on the end of the bar to smooth the resulting stress pulse generated, which minimises the effect of dispersion as the pulse propagates along the bar. Since the distance from the gauge to the bar end is known, the wave speed can be calculated using the time taken from when the incident pulse arrives at the gauge to when the reflected pulse arrives at the gauge. This is done by splitting the recorded signal and shifting the reflected pulse in time such that the sum of the incident and incident and reflected signals is minimised, as shown in Figures 3.12a and 3.12b.

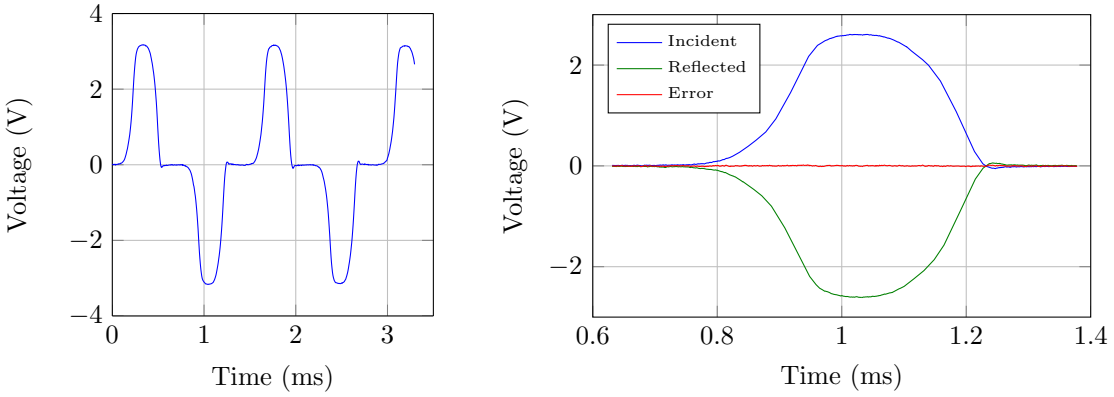

(a) The measured strain gauge data.

(b) The shifted reflected signal.

Figure 3.12: The process used to determine the time taken between incident and reflected pulses.

Once the wavespeed has been determined, the calibration factor can be calculated by striking the bar with a very small amount of putty to generate a pulse with a short rise time and square shape. Three different methods of determining calibration factors for bars are outlined.

Theoretical Calibration Factor

The theoretical calibration factor requires the bar's elastic modulus must be determined to obtain a relationship between stress and strain. This is done using the wave speed, from which the elastic modulus can be determined since the density is known through measurement of the mass and dimensions. For the SHPB system used in BISRU, a bridge circuit with four active arms is used, meaning the ratio of the output voltage to the bridge voltage from the strain gauges can be calculated as:

$$\frac{V_{out}}{V_{in}} = GF\varepsilon \tag{3.4}$$

where ε is the strain measured by the gauge, and GF is the gauge factor. Using the linear relationship between stress and strain and rearranging yields:

$$\sigma = \frac{E}{G_{amp} GF V_{in}} V_{read} \tag{3.5}$$

$$\Rightarrow K = \frac{E}{G_{amp} GF V_{in}} \tag{3.6}$$

where G_{amp} is the amplification factor of the amplifier used. This means that for a known gauge factor, the calibration factor is dependent only on the elastic modulus of the bar and the input voltage. This method is sensitive to the measured value of the gauge factor and the elastic modulus, as well as any deviations in the gauge factor caused by the pasting of the gauge.

Momentum Balance Calibration Factor

This method compares the impulse transferred from the striker to the bar during impact to the impulse calculated from the time integration of the stress pulse, so as to determine the calibration factor experimentally. The impulse transfer can be calculating by considering the change in momentum of the striker, which requires the velocities of the striker before and after impact. The velocity of the striker before impact is measured using a light trap, which consists of two pairs of diode emitters and receivers connected to an oscilloscope. When the striker passes between a single pair, a signal drop will be recorded. Since the distance between the two pairs is known, the time between signal drops can be measured and the velocity inferred.

The velocity after impact can be determined using one dimensional wave propagation theory assuming both the striker and bar have the same material properties. Consider the striker and bar during the time of impact. Assuming contact is made over the entire area, and the striker and bar remain in contact during impact, the interface between the two ends must have the same velocity during impact, and the forces on the faces must be equal and opposite. These conditions result in the following conditions:

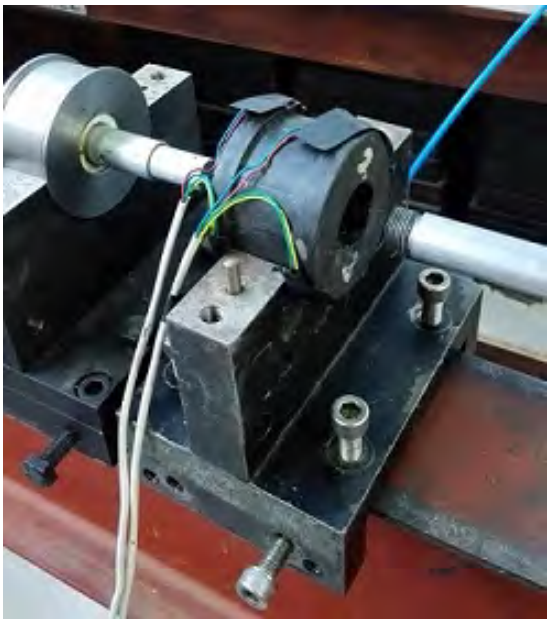

Figure 3.13: The light trap used to record the striker impact velocity.

$$v_s - v_b = 0 \tag{3.7}$$

$$\Rightarrow v_0 = \left(\frac{\sigma_s + \sigma_b}{\rho c}\right)$$

$$\sigma_s A_s = \sigma_b A_b$$

$$\Rightarrow \sigma_b = \frac{A_s}{A_s + A_b}\rho c v_0 \tag{3.8}$$

$$\sigma_s = \frac{A_b}{A_s + A_b}\rho c v_0 \tag{3.9}$$

The subscripts s, and b stand for striker and bar respecitively, and v_0 represents the initial velocity of the striker before impact. The rebound velocity of the striker can be calculated by considering the effect of the stress wave in the striker as it reaches the contact interface after reflecting off the free end. During contact the striker velocity is reduced by $\sigma_s/\rho c$, and once the wave returns, the velocity will be reduced by the same amount. It can be shown that if the area of the striker is smaller than that of the bar, the striker will rebound in the opposite direction to its original velocity [50]. The rebound velocity, v_r, is calculated as:

$$v_r = v_0 \left(\frac{A_s - A_b}{A_s + A_b}\right) \tag{3.10}$$

and the total impulse transferred is then calculated as:

$$I = m_s(v_0 - v_r) \tag{3.11}$$

From the resulting stress pulse measured in the bar, the voltage history can be integrated numerically and the impulse can be calculated as:

$$I = \int_0^t A_b \sigma(t) \mathrm{d}t \tag{3.12}$$

$$= A_b K \int_0^t V_{read} \mathrm{d}t \tag{3.13}$$

Solving for K yields:

$$K = \frac{I}{A_b \int_0^t V_{read} \mathrm{d}t} \tag{3.14}$$

This method is strongly dependent on the calculation of the striker rebound velocity, which requires the impact conditions assumed in the derivation to be close to perfect.

Maximum Stress Calibration Factor

This method is a very simple method of experimentally determining the calibration factor. From Equation 3.8, the stress in the bar can be determined from the initial striker velocity, assuming the stress pulse shape is square, which, providing the pulse length is long enough in comparison to the rise time, is a reasonable assumption. By measuring plateau voltage from the strain gauge, the gauge factor can be determined simply from Equation 3.15.

$$K = \frac{\sigma_b}{V_{read}} \tag{3.15}$$

Figure 3.14a shows an example of signal used to calculate the calibration factor in the input bar.

This method is used for this dissertation because of its simplicity, and the relatively low number of assumptions made. In practice, the two bars' calibration factors are determined simultaneously by placing the bars end-on-end. The input bar is calibrated as outlined above, and output

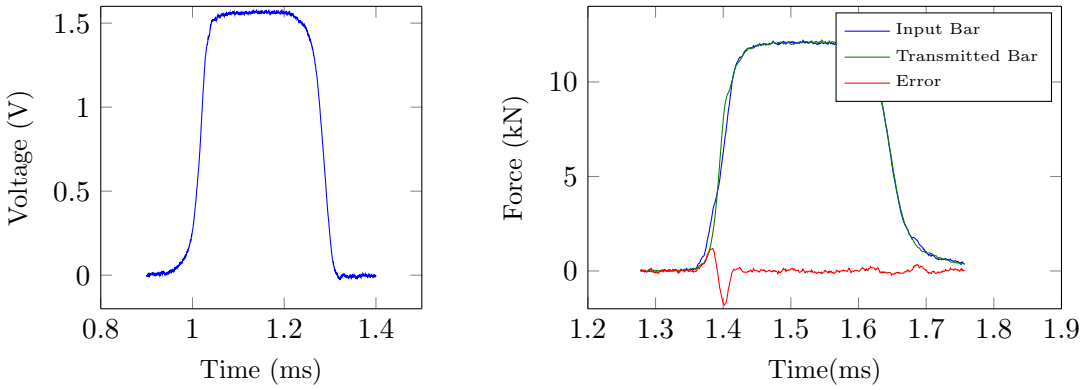

(a) A squarer wave for calibration.

(b) Force equilibrium.

Figure 3.14: The signals used to calculate the calibration factors for the input and output bars.

bar is calibrated by shifting the signals to ensure force equilibrium at the interface between the two bars, as illustrated in Figure 3.14b. This ensures that any small errors which may be present in the calibration will not effect the equilibrium at the specimen interface in the processed data. The error between the two signals is sufficiently small that the issue of dispersion can be ignored when shifting signals. Figure 3.15 shows the two bars placed end on end, with clamps inserted to minimise the reflection at the specimen interface.

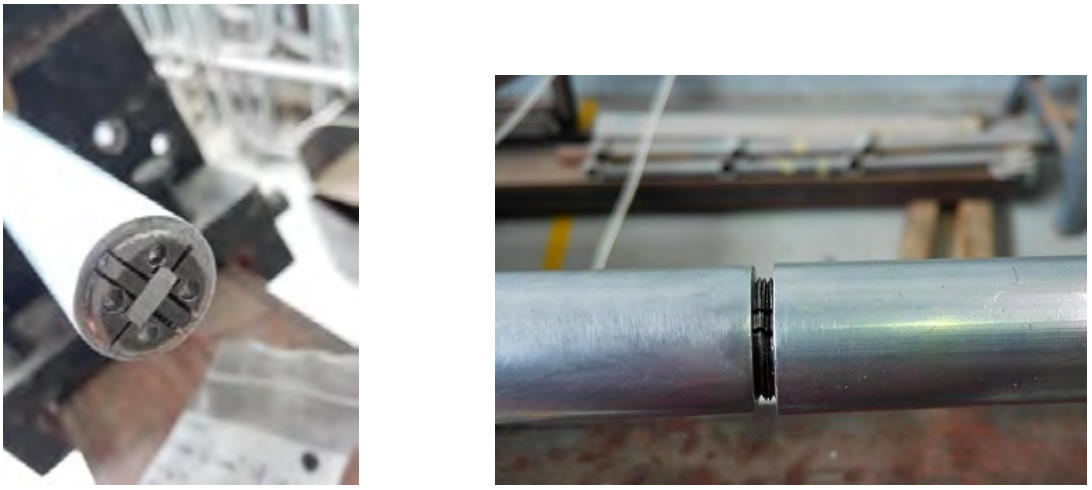

(a) Bar end with clamp and ground specimen.

(b) The bars placed end-on-end.

Figure 3.15: The configuration used to calibrate the input and output bars.

Note that for both experimental calibration methods, the input voltage used during calibration must be recorded so that the calibration factor can be adjusted depending on the input voltage used during testing. Ideally, the same input voltage should be used during calibration and testing. Table 3.1 shows the values obtained from the input and output bar calibration.

Bar	c (m/s)	E (GPa)	V_{in} (V)	K_{theory}	K_{exp}
Input	5121	74.37	1.49	23.11	24.29
Output	5123	74.42	2.40	14.36	11.72

Table 3.1: The calibration parameters measured for the tensile SHPB apparatus.

3.3.3 Data Processing

In order to determine the stress-strain history in a SHPB specimen, the raw signals from the strain gauges must be processed. Figure 3.16 shows a typical set of signals obtained from a tensile test. Note that the input bar signal compromises of an incident and reflected wave, while the output bar signal consists of a single transmitted wave. However, in the case for the example given, the output bar was shorter than the pulse length, meaning the reflection of the transmitted pulse reached the strain gauge before the pulse was complete, meaning a correction must be made.

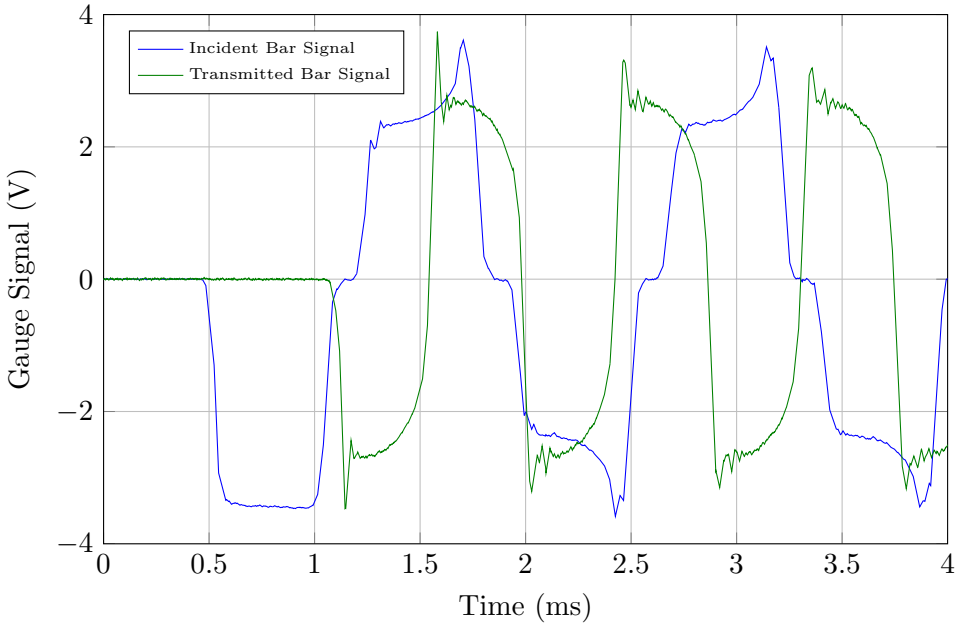

Figure 3.16: An example of raw signals obtained from a tensile SHPB test.

The length of the bars (L_{in}, L_{out}), as well as the distances from the gauges to the specimen interfaces (l_{in}, l_{out}) must be known, as well as the wave speeds and areas of the bars. The input signal is split between the incident and reflected pulses, and they are shifted forward and backward in time respectively to determine the force on the specimen from the input bar. Similarly the output signal is shifted backward in time. The time shifts are given in Equations 3.16 and 3.17.

$$t_{shift(input)} = l_{in}/c \tag{3.16}$$

$$t_{shift(output)} = l_{out}/c \tag{3.17}$$

As mentioned above, the transmitted pulse needed to be corrected due to the reflection off the output bar end interfering with the signal before the pulse had ended. Providing the interference occurs over a relatively small portion of the pulse, it can be assumed that the reflected pulse has the same shape as the transmitted pulse, but is shifted in time according to the length of the bar. Knowing this, the reflected portion of the wave may be removed from the output bar signal. Using the gauge factor found from calibration, the signals can be converted to the stresses at the bar ends in contact with the specimen. Figure 3.17 shows the shifted and corrected signals.

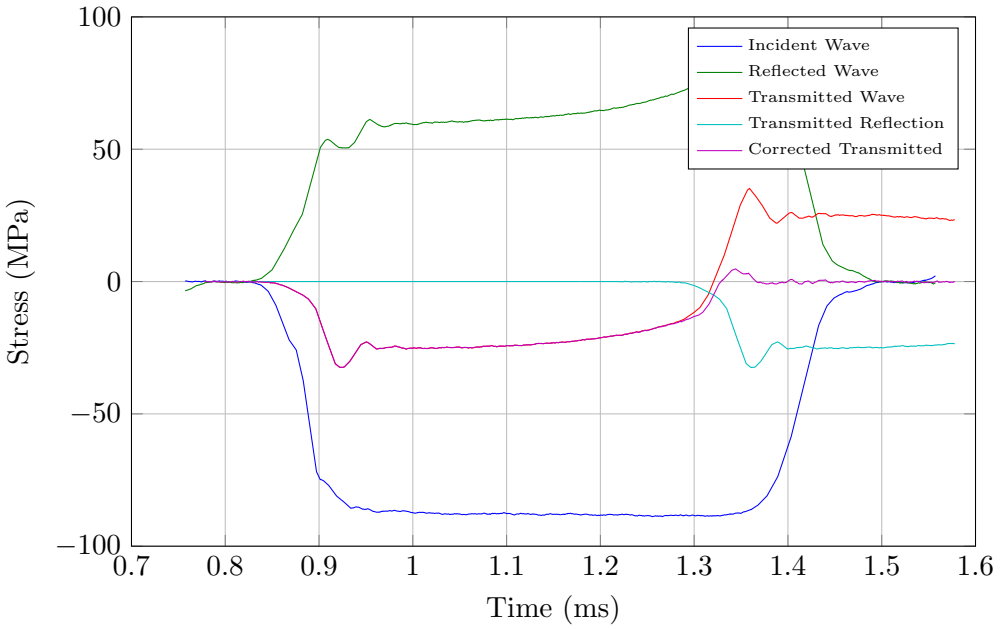

Figure 3.17: An example of shifted signals obtained from a tensile SHPB test.

Once this processing has been completed, the bar end displacements can easily be calculated using the relationship between stress and velocity. The stress in the specimen can either be determined using only the transmitted signal, which generally give a smoother signal, or using an average of the input and output signals. To ensure that the force is constant throughout the specimen gauge section, it is necessary to check for force equilibrium between the input and output bar ends, as shown in Figure 3.18.

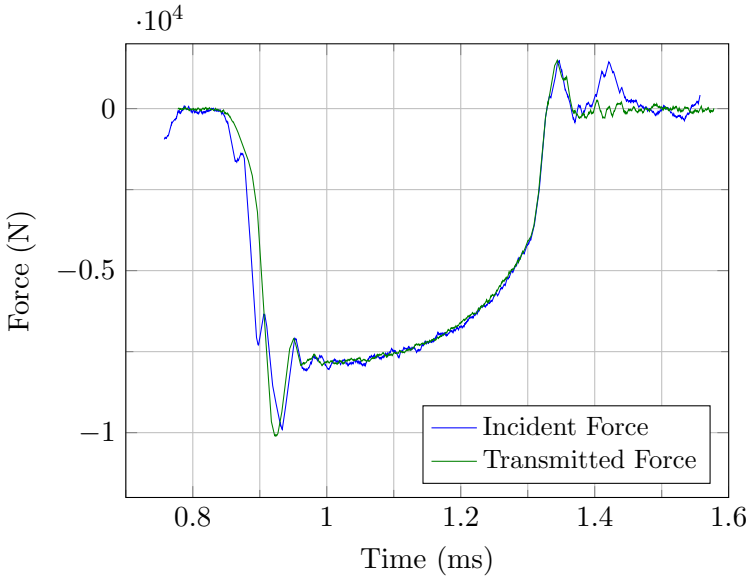

Figure 3.18: Force equilibrium at the specimen interfaces.

To find the true stress in the specimen, the deformation is assumed to be isochoric since the elastic component of the strain is small in comparison to the plastic component. This means that the total gauge volume is preserved, meaning that $A_0, l_0 = A_s l_s$, where the subscript 0 refers to the original properties and s refers to the instantaneous properties. As a consequence, the instantaneous specimen area can be expressed in terms of the original volume and the instantaneous gauge length, which is known from bar end displacements. With this information, the true stress and strain can be found at any point in time using Equations 3.18 and 3.19 respectively.

$$\sigma = \frac{F}{A_s} \tag{3.18}$$

$$\varepsilon = = ln\left(\frac{l_s}{l_0}\right) \tag{3.19}$$

The processed stress-strain and bar end displacement data from the signals given in the above example are shown in Figures 3.19b and 3.19a.

Note the stress overshoot at yield. The material tested does display a less exaggerated upper and lower yield point at quasistatic strain rates, suggesting it is likely that the overshoot exhibited during the tensile SHPB tests is due to a combination of the testing apparatus and material behaviour, the extent of which is yet to be determined.

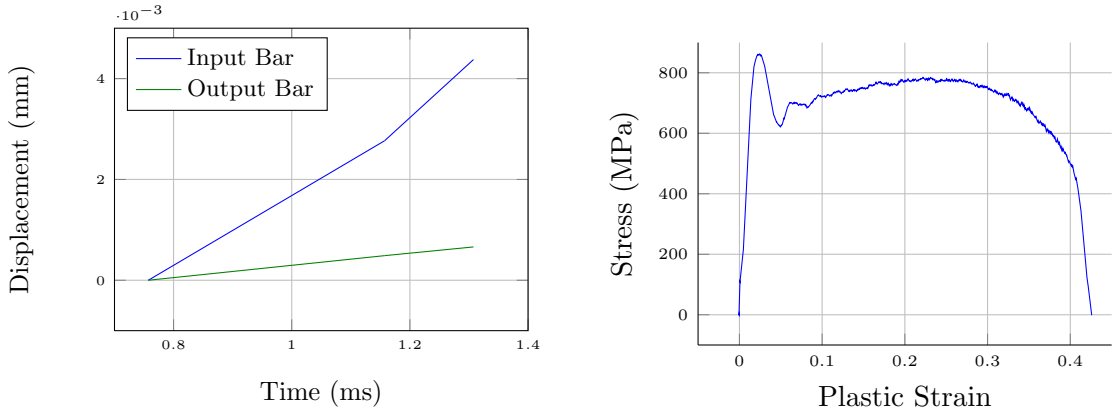

(a) The bar end displacements during a SHPB test.

(b) The stress-strain data.

Figure 3.19: The processed data from a tensile SHPB test.

Chapter 4

Numerical Modelling

As described earlier in Figure 3.1, in order to calibrate the chosen damage model, parallel numerical simulations must be performed along with the experiments to determine the required variables locally at the point of fracture. In order to accurately determine these variables, a constitutive model is required which accurately describes the plasticity behaviour of the material over the entire range of conditions encountered in experiments performed. Additionally, it is important that the finite element simulation accurately represents the experimental test and can be compared directly to the experimental force displacement data. Finally a repeatable procedure is required to calibrate the damage model using the experimental and finite element data.

4.1 Plasticity Model

For the purpose of this dissertation, a user-defined material model was written for use in LS-DYNA [51] such that the plasticity model could be customised to any desired form, and the Bai-Wierzbicki damage model could be implemented. The aim of this section is describe the process of implementing a user-defined material model in LS-DYNA. The theory on which the material model is based will be described, as well as how the theory is implemented in LS-DYNA. The elastic-plastic plastic material model to be implemented is based on the von Mises yield criterion, and therefore the Radial Return method [52, 53] is used as a non-linear solver for the plastic deformation. Furthermore, the material model will only be implemented for use with

the explicit solver to avoid extra complications such as defining elastic-plastic tangent stiffness matrices.

An explicit solver steps through time for a single element, using the element's nodal forces, displacements and velocities from the previous time-step to update the current nodal displacements. Using the current nodal displacements, the strain increment from the previous to the current time step can be determined. In order to update the current stress state, a constitutive relation is needed to relate the strain increment, which was calculated using the explicit solver, to the stress increment. This is why the material model is required, and determines how the material will deform. Figure 4.1 shows a simplified diagram of how the user-defined material model is used with the explicit solver.

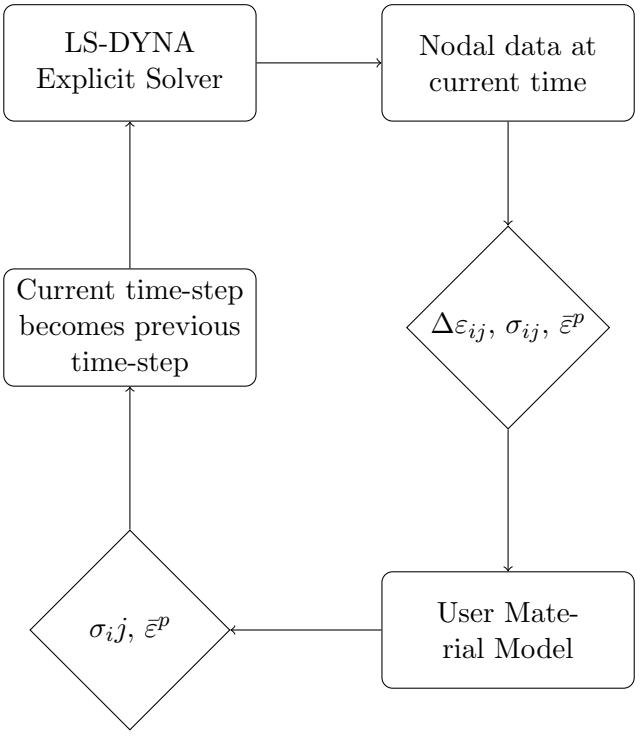

Figure 4.1: A description of how a material model is used in conjunction with an explicit solver

The material model is provided with the current strain increment as well the current stress and any variable which are history dependent and therefore required, such as the total effective plastic strain, $\bar{\varepsilon}^p$. The material model then updates the stress and any other history dependent variables according the constitutive relation.

4.1.1 Plasticity Theory

In order to implement a numerical plasticity model, the basic theory of plasticity is required for an isotropic, strain-hardening material. Determining the material behaviour in the plastic regime requires a description of the multi-axial deformation be described in both the plastic and elastic regime. For the purpose of this dissertation, only small deformation isotropic J_2 plasticity theory will be described. This is sufficient to implement a plasticity model in an explicit dynamic finite element solver, where the time steps are sufficiently small such that the assumption of small deformation holds for each strain increment between steps.

Linear Elasticity

In the elastic regime of deformation, the total stress increment can be linearly related to the strain increment, as shown in Equation 4.1 [10].

$$\sigma_{ij} = \mathbb{C}_{ijkl}\varepsilon_{kl} \tag{4.1}$$

where $\mathbb{C}$ is a fourth order elasticity tensor relating the second order stress and strain tensors. For the case of isotropy, the stress-strain relationship can be simplified to:

$$\sigma_{ij} = \lambda\varepsilon_{kk}\delta ij + 2\mu\varepsilon_{ij} \tag{4.2}$$

where λ and μ are Lamé coefficients which are material specific. μ is also known as the shear modulus, G.

Furthermore, the stress and strain tensors can be decomposed into their hydrostatic and deviatoric parts, ash shown is Equations 4.3 and 4.4.

$$\sigma_{ij} = \frac{1}{3}\sigma_{kk}\delta_{ij} + S_{ij} \tag{4.3}$$

$$\varepsilon_{ij} = \frac{1}{3}\varepsilon_{kk}\delta_{ij} + e_{ij} \tag{4.4}$$

The hydrostatic, or volumetric part of the stress tensor is the average of the three normal stresses, whilst the deviatoric, or distortional part, S_{ij}, represents the stress causing volume preserving deformation, and can be calculated by removing the hydrostatic stress from the total stress. Similar principles hold for the strains.

However, once the material reaches its yield stress, it enters the elastic-plastic regime of deformation, where the total strain is additively decomposed into its elastic and plastic parts.

$$\varepsilon_{ij} = \varepsilon^e_{ij} + \varepsilon^p_{ij} \tag{4.5}$$

In the elastic-plastic regime, the stress can no longer be linearly related to the strain as in the linearly elastic regime. In order solve this non linear problem, the stress is solved incrementally by updating the strain in small strain increments. In order to do this, three functions must be defined:

- A yield criterion describing the yield surface of a material under multiaxial loading.
- A flow law governing the direction of plastic strain.
- A hardening law describing how the yield surface changes due to parameters such as plastic strain.

The von Mises Yield Criterion

In a uniaxial tension problem, yielding will occur when the stress reaches a critical value. However, in a multiaxial problem, a single equivalent measure of stress can be derived which represents the various stress components as a single value which can be compared to yield value. Similarly, to measure the effect of plastic strain, an equivalent measure of plastic strain is required. For this reason, the yield criterion is introduced. For the purpose of this report, only the von Mises (Levy-Mises) yield criterion for isotropic materials will be discussed, as the criterion is suitable for ductile materials such as steel [10].

A yield criterion is a function which describes the evolution of the yield point of a material undergoing some deformation in the elastic or elastic-plastic regime. The form of a typical yield criterion is shown is Equation 4.6.

$$\phi(\sigma_{ij}, \bar{\varepsilon}^p) = f(\sigma_{ij}) - H(\bar{\varepsilon}^p) \leq 0 \tag{4.6}$$

In the above equation, $f(\sigma_{ij})$ is a function describing the equivalent stress from the current stress state, and $H(\bar{\varepsilon}^p)$ is a hardening function which describes the current yield value depending on the current equivalent plastic strain. The yield criterion states that the current equivalent stress must be less than or equal to the current yield value. In the case of incremental strain theory, linear elasticity holds so long as the current stress state does not violate the yield criterion. However, if the yield criterion is violated, the plastic strain must be updated so as to satisfy the criterion.

The difference between various yield criteria lies in the definition of $f(\sigma_{ij})$. The basis of the von Mises criterion is that the plastic strain is a function of the distortional stress and not the hydrostatic stress. The von Mises criterion can be interpreted as yielding occurring when the elastic distortional energy reaches a critical value. Mathematically, this can be written as:

$$J_2 - k^2 \leq 0 \tag{4.7}$$

where J_2 is the second invariant of the deviatoric stress tensor, given as $\frac{1}{2}S_{ii}S_{ii}$, and k is the critical value of the distortional energy at which yielding occurs. Considering the case of uniaxial tension at the point of yielding and ignoring hardening effects:

$$J_2 = \frac{1}{3}\sigma_{11}^2 = \frac{1}{3}\sigma_y^2 = k^2 \tag{4.8}$$

$$\Rightarrow k = \frac{\sigma_y}{\sqrt{3}} \tag{4.9}$$

Taking strain hardening into account, the von Mises yield criterion can be written as:

$$\sqrt{3J_2} - H \leq 0 \tag{4.10}$$

$$\Rightarrow \sqrt{\frac{3}{2}S_{ij}S_{ij}} - H \leq 0 \tag{4.11}$$

By including the factor of 3, the yield criterion can be expressed in terms of a uniaxial yield stress, H, rather than the shear stress, k. The equivalent stress, or von Mises stress, is given as:

$$f(\sigma_{ij}) = \bar{\sigma} = \sqrt{\frac{3}{2} S_{ij} S_{ij}} \tag{4.12}$$

In the principle stress space, the yield criterion simplifies to:

$$\frac{1}{2}\left[(\sigma_1 - \sigma_2)^2 + (\sigma_2 - \sigma_3)^2 + (\sigma_3 - \sigma_1)^2\right] - H^2 \leq 0 \tag{4.13}$$

which represents a cylinder, the axis of which coincides with the $(1, 1, 1)$ vector in the principle stress space, and the radius of which is $\sqrt{\frac{2}{3}}H$. The factor of $\sqrt{\frac{2}{3}}$ in the radius can be explained by considering the projection of any of the principle stresses onto the plane with normal in the direction $(1, 1, 1)$, since the cosine of the angle between any of the principle axes is given as $\cos\theta = \sqrt{\frac{2}{3}}$. Any stress state must lie within or on the yield surface. Figure 4.2 shows the von Mises yield surface.

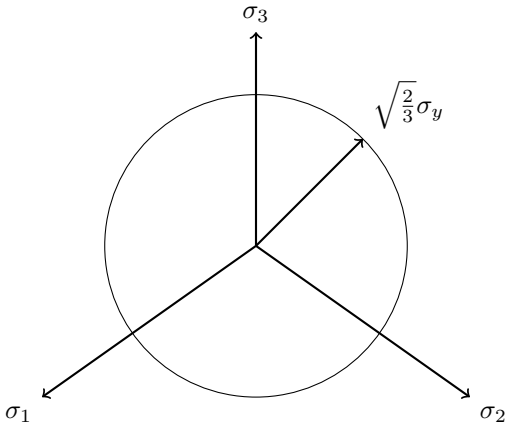

Figure 4.2: The von Mises yield surface as seen from the pi plane with normal in the $(1, 1, 1)$ direction.

Given a small strain increment, $d\varepsilon$, if the calculated elastic stress state lies outside the yield surface, the material has begun plastic deformation, meaning the calculated elastic stress is invalid, and a non-linearity arises due to the fact that the yield value, H, is a function of the effective plastic strain increment, $\Delta\bar{\varepsilon}^p$.

The Flow Law

The flow law governs the direction of plastic flow once the material reaches the elastic-plastic regime. The Levy-Mises flow law [10] is an associated flow law, meaning the direction of plastic flow is always normal to the yield surface. This can be expressed mathematically as:

$$d\varepsilon_{ij}^{p} = d\lambda \frac{\partial \phi}{\partial \sigma_{ij}} \tag{4.14}$$

Equation 4.14 states that the plastic strain tensor is a scalar multiple of the derivative of the yield function with respect to the stress tensor. In the principle stress space, this derivative is normal to the yield surface, and $d\lambda$ represents the plastic multiplier, which must be obtained to calculate the plastic strain increment. In the case of the von Mises yield surface, the derivative of the yield function with respect to the stress tensor yields the deviatoric yield tensor, as shown in Equation 4.15.

$$d\varepsilon_{ij}^{p} = S_{ij} d\lambda \tag{4.15}$$

Lastly, the effective plastic strain should be defined such that the change in the effective plastic strain increment is consistent with the change in strain in the direction of the tensile stress for a uniaxial tensile test, as shown in Equation 4.18.

$$\begin{pmatrix} d\varepsilon_{11}^{p} & 0 & 0 \\ 0 & d\varepsilon_{22}^{p} & 0 \\ 0 & 0 & d\varepsilon_{33}^{p} \end{pmatrix} = \begin{pmatrix} \frac{2}{3}\sigma_{11} & 0 & 0 \\ 0 & -\frac{1}{3}\sigma_{11} & 0 \\ 0 & 0 & -\frac{1}{3}\sigma_{11} \end{pmatrix} d\lambda \tag{4.16}$$

$$d\bar{\varepsilon}^{p} = k\sqrt{d\varepsilon_{ij}^{p} d\varepsilon_{ij}^{p}} = d\varepsilon_{11}^{p}$$

$$\Rightarrow k\sqrt{\frac{2}{3}}\sigma_{11} d\lambda = \frac{2}{3}\sigma_{11} d\lambda$$

$$\Rightarrow k = \sqrt{\frac{2}{3}} \tag{4.17}$$

$$\boxed{\Rightarrow d\bar{\varepsilon}^{p} = \sqrt{\frac{2}{3} d\varepsilon_{ij}^{p} d\varepsilon_{ij}^{p}}} \tag{4.18}$$

The Hardening Law

In order to define how the yield surface changes as the plastic strain increases, a hardening law is required. For an isotropic material, the effect of hardening is independent of the direction of plastic strain [10]. This means that the radius of the yield surface will grow uniformly regardless of the direction of loading. However, the amount of hardening is history dependent, since the hardening value is dependent on cumulative amount of plastic strain. Mathematically, the consequence of isotropy is that the hardening function. H, is a function of the total effective plastic strain, where the total effective plastic strain is the integral of the effective plastic strain increments over a loading cycle, as shown in Equation 4.19.

$$\bar{\varepsilon}^p = \int_{\varepsilon_0}^{\varepsilon_f} \mathrm{d}\bar{\varepsilon}^p \tag{4.19}$$

The hardening effect is shown graphically in Figure 4.3. H_0 is the initial value of the hardening function before any plastic strain has occurred.

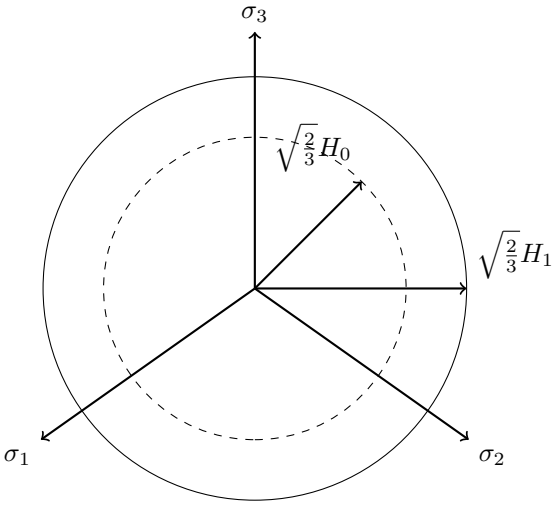

Figure 4.3: The effect of strain hardening for an isotropic material.

4.1.2 The Radial Return Method

When the material enters the plastic regime, a method of solving the non-linear equation given by the yield function is required. The yield function must always be less than or equal to zero, so for a given strain increment, the plastic strain increment must be solved such that the yield function is equal to zero. This can be done iteratively using a non-linear solver such as

Newton's Method or the Bisection Method Alternatively, by making certain assumptions, the plastic strain increment can be solved directly, which is the basis of the Radial Return Method. This method is a return mapping algorithm [52, 53], whereby a trial stress is predicted using the elastic constitutive relation, and using the trial stress, the new yield surface is calculated and the stress returned to the new yield surface on the assumption that the plastic strain increment is normal to the updated yield surface.

Elastic Predictor

Consider a material under a stress state in the elastic region at time t given by σ_{ij}^{t}. The strain is then increased by $d\varepsilon$ such that the material enters the elastic-plastic regime. The updated stress is given by:

$$\sigma_{ij}^{t+\Delta t} = \sigma_{ij}^{t} + \mathbb{C}_{ijkl}[d\varepsilon_{kl} - d\varepsilon_{kl}^{p}] \tag{4.20}$$

An initial guess for the stress is made by assuming the material responds elastically. This is known as the elastic trial or predictor stress, and is given by:

$$\sigma_{ij}^{trial} = \sigma_{ij}^{t} + \mathbb{C}_{ijkl}d\varepsilon_{kl} \tag{4.21}$$

From Equations 4.20 and 4.21, the final stress can be calculated as:

$$\sigma_{ij}^{t+\Delta t} = \sigma_{ij}^{trial} - \mathbb{C}_{ijkl}d\varepsilon_{kl}^{p} \tag{4.22}$$

Calculating the Plastic Strain Increment

In order to solve for the final stress, the plastic strain increment is required. Using the flow law, and assuming the plastic flow over the entire strain increment is normal to the yield surface calculated using the trial stress, the final stress can be written as:

$$\begin{aligned}\sigma_{ij}^{t+\Delta t} &\approx \sigma_{ij}^{trial} - \mathbb{C}_{ijkl} S_{kl}^{trial} d\lambda \\ &= \sigma_{ij}^{trial} - 2G S_{ij}^{trial} d\lambda \qquad (4.23)\\ \Rightarrow S_{ij}^{t+\Delta t} &\approx S_{ij}^{trial} - 2G S_{ij}^{trial} d\lambda \\ &= S_{ij}^{trial}(1 - 2G d\lambda) \qquad (4.24)\end{aligned}$$

Note that the elastic constitutive tensor is simplified to $2G$ since the plastic strain increment is dependent on the distortional stress only, and, consequently, the final deviatoric stress can be written as a scalar multiple of the trial deviatoric stress, hence the name "Radial Return Method" since the trial stress is scaled back along the radius of the yield surface.

To calculate the required plastic strain increment, the approximation for $S_{ij}^{t+\Delta t}$ is calculated such that the new stress satisfies the yield criterion, as shown in Equation 4.28.

$$\begin{aligned}\phi(\sigma_{ij}, \bar{\varepsilon}^p) &= \sqrt{\frac{3}{2} S_{ij}^{t+\Delta t} S_{ij}^{t+\Delta t}} - H^{t+\Delta t} = 0 \\ \Rightarrow (1 - 2G d\lambda) &\sqrt{\frac{3}{2} S_{ij}^{trial} S_{ij}^{trial}} - H^{t+\Delta t} = 0 \qquad (4.25)\\ \Rightarrow (1 - 2G d\lambda)\bar{\sigma}^{trial} &- H^t - \left.\frac{\partial H}{\partial \bar{\varepsilon}^p}\right|_t d\bar{\varepsilon}^p = 0 \qquad (4.26)\\ \Rightarrow (1 - 2G d\lambda)\bar{\sigma}^{trial} &- H^t - \frac{\partial H}{\partial \bar{\varepsilon}^p}\left(\frac{2}{3}\bar{\sigma}^{trial} d\lambda\right) = 0 \qquad (4.27)\\ &\boxed{\Rightarrow d\lambda = \frac{3}{2}\left(\frac{\bar{\sigma}^{trial} - H^t}{3G + \frac{\partial H}{\partial \bar{\varepsilon}^p}}\right)} \qquad (4.28)\end{aligned}$$

Note the hardening function is approximated using the tangent at the current time step. This approximation is valid providing the strain increment is sufficiently small. If greater accuracy is required, an iterative method can be used to solve Equation 4.26. Finally using the flow law, the plastic strain increment can then be calculated as:

$$d\varepsilon_{ij}^p = S_{ij}^{trial} d\lambda \qquad (4.29)$$

Updating the Stress

The final step is to use the calculated plastic strain increment to update the stress using Equation 4.22. Additionally the effective plastic strain and any other history dependent variables can be calculated and stored. Figure 4.4 shows a graphical representation of the Radial Return Method.

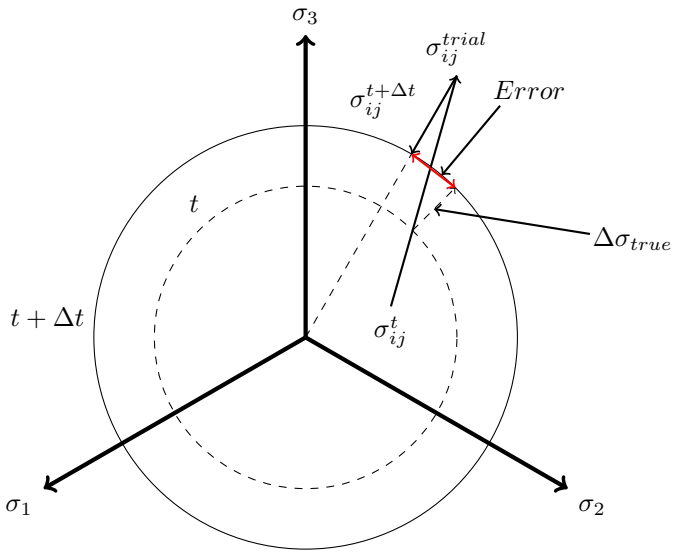

Figure 4.4: A graphical representation of the Radial Return Method

Using this algorithm, any constitutive relationship between stress and plastic strain can be implemented, providing the displacement increments are small enough. Strain rate and temperature effects can also be included with relative ease.

4.1.3 Strain Rate Dependency

Including the effect of strain rate in the plasticity is critical for the calibration of a damage model over different strain rates, as the plasticity model must accurately predict the stress state parameters at failure required to calibrate the damage model, and must do so over the full range of strain rates tested. In order to incorporate strain rate effects into the radial return algorithm, a minor adjustment must be made to the linear approximation of the hardening function gradient, so as to include the strain rate derivative.

$$H^{t+\Delta t} = H^t + \left.\frac{\partial H}{\partial \bar{\varepsilon}^p}\right|_t d\bar{\varepsilon}^p + \left.\frac{\partial H}{\partial \dot{\varepsilon}^p}\right|_t d\dot{\varepsilon}^p \tag{4.30}$$

In Equation 4.30, the hardening function is approximated by a Taylor expansion where the hardening rate is a function of plastic strain and plastic strain rate. As mentioned in Section 2.1, the plastic strain rate is generally used to quantify the effect of strain rate on the material hardening.

Calculating the strain rate poses a challenge when using the Radial Return algorithm. Consider a material deforming under an elevated strain rate in the elastic regime. At this point the material has not undergone any plastic strain, and so the plastic strain rate must be zero. However, at the point where the material first undergoes a plastic strain increment, the plastic strain increment steps from zero to a non-zero number, which increases the radius of the yield surface for the next time step due to strain rate effects.

The discontinuity in plastic strain rate can mean that the material will enter the elastic regime again for the next time step, provided that the stress increment is smaller than the change in the radius of the yield surface. Essentially, at the point where yielding occurs, the yield surface will instantaneously grow due to the onset of plastic strain rate effects, and the model will evaluate the material as falling in the elastic regime for the *next* time-step. If next time step results in an elastic strain increment, the plastic strain rate will instantaneously step back to zero, resulting in the yield surface shrinking to its original size. The model now evaluates the material as falling in the plastic regime again, resulting in the plastic strain rate becoming non-zero again, and so on. This instability prevents the material from exhibiting the desired strain rate behaviour, causing the yielding behaviour to be much more gradual than desired.

The discrepancy in yield behaviour suggests that perhaps plastic strain alone is not a suitable parameter to predict plasticity behaviour. However, since majority of the constitutive models available in literature use plastic strain as a material parameter, corrections are made to use the plastic strain rate. In order to prevent the above problems, four possible implementations are considered:

- Using the total strain rate.
- Using the deviatoric strain rate.
- Using a weighted moving average of the plastic strain rates.
- Storing the plastic strain rate as a history variable.

The first option is a simple solution to the problem, as total strain rate is non-zero during elastic deformation. However, the total strain rate will always be greater than the plastic strain rate due to the elastic portion of strain, although the elastic strain increment will generally be much smaller than the plastic strain increment. A slightly better approximation can be made using the deviatoric strain rate, since the plastic yield is assumed to be due to the distortional component of deformation only.

Another option is to use weighted moving average of the plastic strain rates, which prevents the value for strain rate from stepping back and forth between zero and a non-zero value. The value for strain rate is taken as an average between the current and previous strain rate values, where the contribution of the previous averaged value is weighted by some given weighting factor.

$$\dot{\varepsilon}_{ave} = \frac{\dot{\varepsilon}_i + N\dot{\varepsilon}_{i-1}}{N+1} \tag{4.31}$$

This method causes a lag in the response, since any sudden changes in strain rate are affected by the previous averaged value. However, providing the time step is small enough, this may be acceptable.

Finally, the option of storing the plastic strain rate as an internal variable was considered. This means that the previous strain rate is stored in memory and updated during the element subroutine. If the element is in the elastic regime, the plastic strain rate is left unchanged, meaning the plastic strain rate will remain non-zero after the first plastic step and still update accurately providing the material is in the plastic regime. This solves the problem of the yield surface growing and shrinking during yield, and provides the most stable and smoothest response. For these reasons, this simple approach was used in the material model.

4.1.4 Temperature Dependency

It has been shown that metals exhibit less strength at elevated temperatures, as discussed in [11–13]. As the material undergoes the non-reversible process of plastic strain during a tensile test, a percentage of the energy dissipated will be converted into thermal energy within the specimen. Kapoor and Nematt-Nasser [54] suggest that all the plastic work done will be converted into thermal energy. This increase in thermal energy will cause a rise in temperature in the specimen, given by:

$$\Delta T = \frac{1}{\rho C_v} \int_0^{\varepsilon^p} \sigma \mathrm{d}\varepsilon^p \tag{4.32}$$

where C_v is the specific heat capacity of the material. Providing the rate of change in temperature is low enough, the temperature can be updated using the current stress and plastic strain increment after each time step, meaning that temperature is effectively treated as a constant during the radial return algorithm and does not need to be included in the hardening function gradient.

Temperature is generally treated as an internal variable [28], meaning that the temperature is updated during the element subroutine using Equation 4.32, and adiabatic conditions are assumed, meaning that no heat leaves the element boundary. This assumption depends on the rate at which the heat is generated, which depends on the plastic strain rate. For global strain rates (i.e. the strain rate calculated using the specimen boundary conditions) of $\dot{\varepsilon}^p >> 1000^{-1}$, this assumption is fairly accurate, however for strain rates lower than $1000s^{-1}$ the assumption become less valid, although the rise in temperature is still significant. A simple model representing a SHPB specimen under constant strain rate deformation was made to estimate the effect of strain rate on temperature in the gauge section of the specimen. The model consists of two blocks, one representing the gauge section and the other representing the clamped section of the specimen. The strain is updated according to the strain rate, and thermal energy is generated according to the plastic strain increment. Additionally, heat is allowed to flow from the gauge section to the clamped section, assuming no heat leaves the specimen boundaries. Figure 4.5 shows a comparison of the temperature in the specimen gauge section between a strain rate of $0.1s^{-1}$ and $1000s^{-1}$.

The assumption of adiabatic conditions becomes particularly invalid during the local necking stage of deformation, where the plastic strain field is highly localised, resulting in high temperature spacial gradients in the area of necking. Since heat flow is proportional to the spatial gradient of the temperature, the rate of heat flow increases significantly in the necked region. For this reason a coupled thermal-structural analysis was performed in LS-DYNA, such that the temperature is calculated similarly to that described in Equation 4.32, but linear isotropic heat conduction is used to account for the flow of heat between elements. Figure 4.6 shows a comparison between the plastic strain and temperature fields developed during the simulation of a SHPB test.

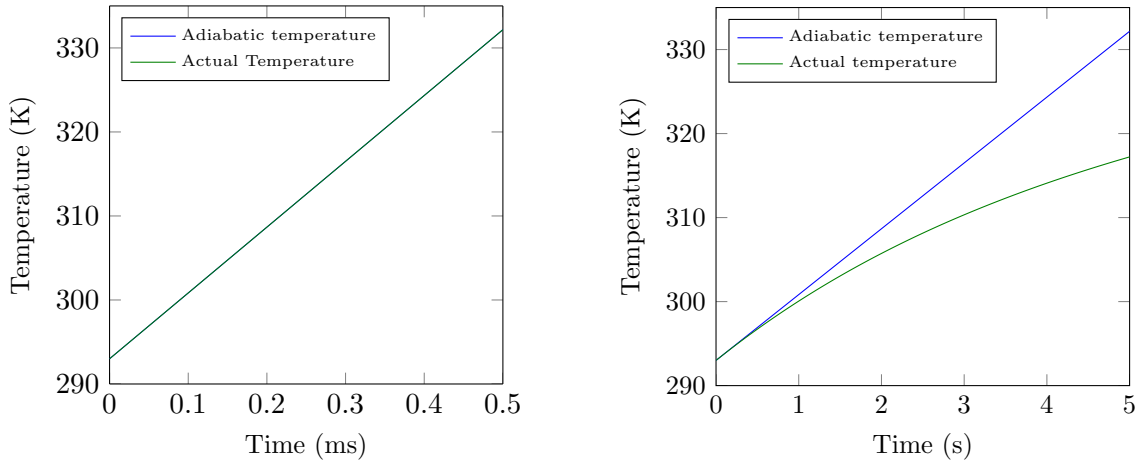

(a) $\dot{\varepsilon} = 1000s^{-1}$. (b) $\dot{\varepsilon} = 0.1s^{-1}$.

Figure 4.5: An illustration of the effect of strain rate on temperature evolution in a SHPB specimen.

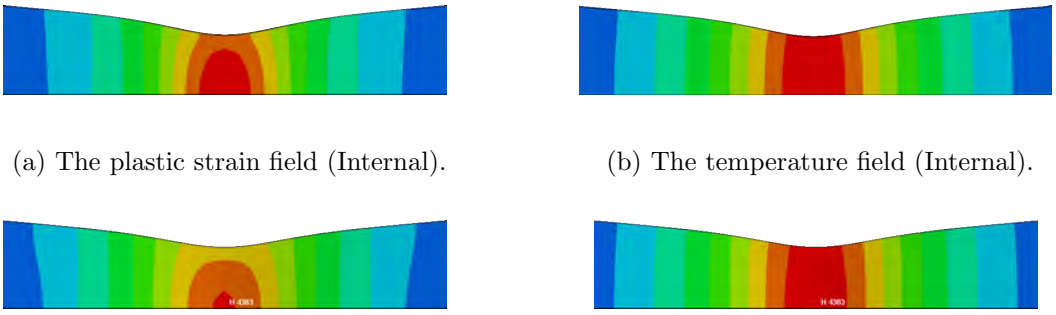

(a) The plastic strain field (Internal). (b) The temperature field (Internal).

(c) The plastic strain field (Surface). (d) The temperature field (Surface).

Figure 4.6: A comparison of plastic strain and temperature fields in a SHPB specimen.

Note that the temperature is much less localised than the strain field across the gauge section of the specimen. As a consequence of this, the temperature at the centre of the gauge section is significantly less than the adiabatic temperature rise in the element. Figure 4.7 shows the temperature calculated using the LS-DYNA thermal solver compared to the adiabatic temperature calculated using the stress and plastic strain histories at the center of the specimen gauge section.

Note that the adiabatic temperature shown is an estimate as it is calculated using stress and strain values obtained from the simulation that used the thermal solver. However the difference in values between the actual and adiabatic temperatures is large enough to illustrate a trend. For this dissertation, the LS-DYNA thermal solver was used in conjunction with the structural solver for the SHPB simulations in order to increase the accuracy of the temperature field in

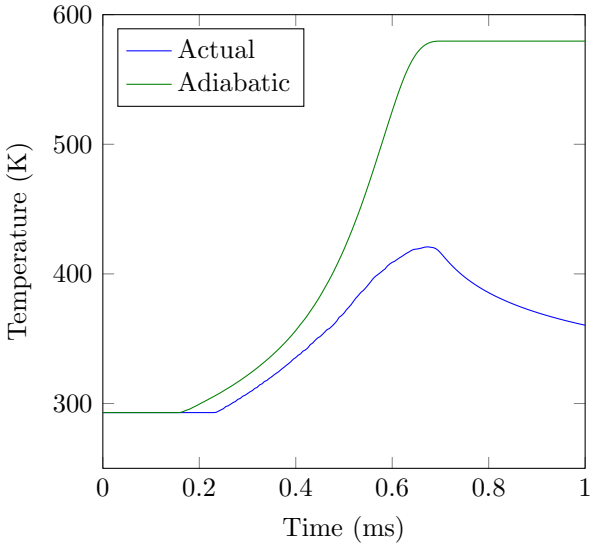

Figure 4.7: A comparison of the temperature generated using the LS-DYNA thermal solver and the adiabatic temperature for a SHPB test simulation ($\dot{\varepsilon} \approx 600s^{-1}$.

the specimen.

4.1.5 Calibration

In order to calibrate the plasticity model, an optimisation routine is used to determine the parameters resulting in the best fit between the simulated and experimental force-displacement curves. LS-OPT is used to generate the optimisation routine, which involves parameterising the desired design variables such that a number of simulations can be generated which will sufficiently fill the design space to determine an objective function. In the case of the calibration of the plasticity model, the objective function represents the mean square error of the simulated force displacement curve compared to the experimental force-displacement curve. By sampling the mean square error for different combinations of the design parameters, the mean square error can be expressed as a function of the design parameters. By minimising the function, the optimum parameters can be determined, which completes a single loop of the optimisation routine. This process is repeated until enough sample points are recorded to minimise the error within a given tolerance. Figure 4.8 shows an example of an optimisation routine set up in LS-OPT.

Based on the advantages and disadvantages of the models discuessed in Section 2.1, the Zhao plasticity model is chosen as it is validated for mild steel, and simple to calibrate. The process used to calibrate the model is as follows:

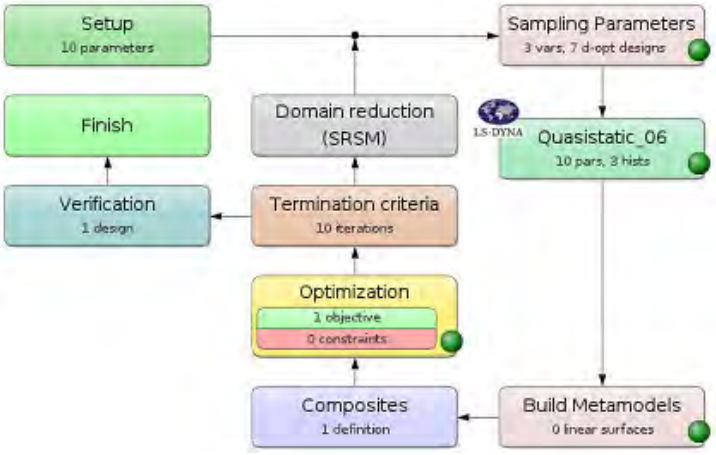

Figure 4.8: The optimisation routine used to determine the required parameters for the 0.6 mm/min quasistatic test.

1. Estimate starting values for the quasistatic strain hardening material parameters by fitting a curve to the stress strain data obtained from processed experimental data for the 0.6 mm/min quasistatic straight specimens.

2. Plot the yield stress values against strain rate for the three different strain rates on a logarithmic scale. Using data from the two quasistatic rates, determine the gradient of the logarithmic strain rate term, and using the dynamic rate data, determine the coefficient for the exponential strain rate term.

3. Set up numerical model for the 0.6 mm/min quasistatic straight specimen using the Zhao constitutive relation, but removing the softening term in the logarithmic strain rate dependency portion of the Zhao function.

4. Run an LS-OPT optimisation routine using the calculated starting values, varying the material constants which define the quasistatic strain hardening portion of the function.

5. Using the optimised results, set up a numerical model for the 100 mm/min quasistatic straight specimen, including the logarithmic strain rate term.

6. Run an LS-OPT optimisation routine varying the strain rate softening term constants to fit the simulation to the 100 mm/min experimental data.

7. Validate plasticity model using dynamic simulation.

8. Make adjustments to strain rate constants if needed and repeat process.

Note that the temperature dependence constants are taken from literature [11], and the temperature effects are only included for the dynamic tests, as the quasistatic tests are assumed to be isothermal, as shown in Section 4.1.4.

4.2 Quasistatic Tests

Modelling a quasistatic tensile test is a relatively simple process in terms of generating the mesh, as a displacement or velocity boundary condition can be applied directly to the specimen, meaning the only mesh required is that of the specimen. Additionally, to reduce the computational time required, the test can be modelled with $^1/_8$ symmetry with the velocity of the boundary condition in the simulation half that of the experimental cross-head speed, and the force recorded in the simulation a quarter of the experimentally observed force. However, the difficulty of simulating a quasistatic test lies in the length of time over which the test takes place, or more specifically the time step size relative to the test duration. Explicit time integration methods are conditionally stable depending on the critical time step size, which is dependent on the highest modal frequency of the mesh. Physically, this can be interpreted as the shortest time taken for information to propagate through any element in the mesh, meaning the time step used in the integration scheme must be small enough such that information will not propagate across more than one element during a single time step [55]. The critical time step size can be estimated by:

$$\Delta t_c \approx \frac{L_e}{c} \tag{4.33}$$

where L_e is the effective element length and c is the material wave speed, which is dependent on density and the elastic modulus. Consequentially, in a homogeneous isotropic mesh, the critical time step is dictated by the smallest element.

Because a fine mesh is required, particularly in the gauge section, to accurately record the history variables locally at the point of failure, the critical time step required for stability for any explicit solver is very small in comparison to the test duration, meaning the amount of computational time required to solve the problem using any explicit finite element analysis is unfeasible.

Traditionally, an implicit analysis would be used for this type of problem, where the integration scheme is unconditionally stable meaning the time step size can be arbitrarily large and needs only to be small enough to obtained the desired accuracy. However, an implicit scheme requires a global tangent-stiffness matrix which must be assembled as the sum of the contributions from each element subroutine. Since a user defined element subroutine was written for this dissertation, defining a tangent-stiffness matrix assembly subroutine would add complexity beyond the scope of this dissertation.

A far simpler method of increasing the time step size is to make use of a mass-scaled solution. By artificially increasing the density of the material, the wave speed is decreased which results in a larger critical time step size, meaning fewer time steps can be used to complete the analysis. For a quasistatic test where the inertia of the specimen is negligible in comparison to the internal forces generated during deformation, increasing the density will have no effect on the accuracy of the solution, providing the density is kept low enough such that the total kinetic energy remains negligible in comparison to the total strain energy energy. Scaling factors of approximately 1×10^8 and 1×10^4 were used for the 0.6 mm/min and 100 mm/min tests respectively with kinetic energies of the order 1×10^{10} times smaller than the internal energies.

4.3 SHPB Tests

Simulating SHPB tests poses a challenge due to the nature of the SHPB apparatus. In order to compare the experimental SHPB data to the numerical data, it is necessary to model the SHPB apparatus as well as the specimen due to the nature of the boundary conditions at the specimen interface. During quasistatic tests, the forces and displacements recorded by the data acquisition unit are essentially identical to the forces and displacements of the clamped region of the specimen. However, due to inertial effects present during a SHPB test, applying boundary conditions directly to the specimen while still accurately representing the boundary velocities and forces is difficult.

An alternative is to to model both the input and output bars as well as the specimen and apply the stress pulse measured during testing to the end of the input bar, as was done by Verleysen et. al. [56]. She found that modelling 2 m portions of the bars is sufficient to prevent any reflections off the bar ends from interfering with the specimen, and that the mesh used for the bars can be relatively coarse since the wave propagation is effectively one-dimensional in

the region of the bars where the strain is measured. However, the mesh at the bar-specimen interface needs to be finer in order to accurately capture the load transfer from bar to specimen, which can no longer be considered one-dimensional. For the modelling of round specimens, an axisymmetric model using 2D-axisymmetric elements can accurately represent the experiment. However, since the problem is no longer axisymmetric with the use of sheet specimens, a $^1/_4$ symmetry model is used. In modelling the interface between the specimen and bars, a tied contact was used. Verleysen used specimens, an example of which is shown in Figure 4.9, that are glued into slots in the bars, meaning that the interfaces are only tied on the sides of the specimen glue zone, where the glue is able to transmit high stresses, and not on the butt of the specimen.

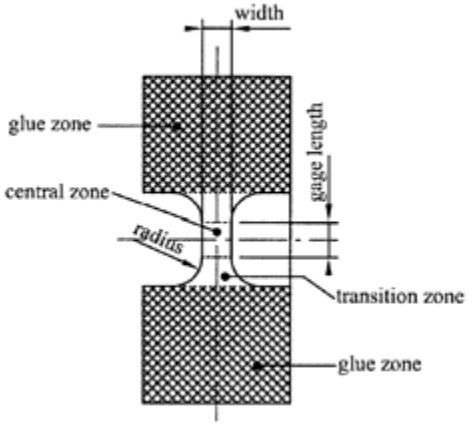

Figure 4.9: The sheet specimen used by Verleysen for tensile SHPB experiments [56].

Although modelling the full SHPB apparatus is ideal in order to correctly simulate the specimen boundary conditions, the extra computational time added is significant, as the total number of nodes is increased due to the extra parts in the model, and the total simulation time must be increased in order to allow the stress pulse to travel through both bars. As a solution to this problem, Bowden was able to eliminate the effect of reflections off the bar ends using infinite elements at the bar ends [9], which meant that the length of the bars required in the numerical model had only to be sufficient to ensure one-dimensional wave propagation at the portion where the strain output is recorded for analysis.

Infinite elements are specially formulated elements which impose a negative boundary stress proportional to the nodal velocities to the current stress in the element, as proposed in 1969 by Lysmer and Kuhlemeyer [57]. Since the magnitude of the stress is proportional to the particle velocity according to one-dimensional wave theory, the nodal velocities can be used to determine the exact value of the stress wave arriving at the boundary, and a stress can be imposed in the

opposite direction at the element boundary, thus preventing a reflected wave, and effectively behaving as if the wave were to propagate into an infinite medium. A similar option is available in LS-DYNA called the non-reflecting boundary condition.

4.3.1 Non-Reflecting Boundary Condition in LS-DYNA

The non-reflecting boundary condition in LS-DYNA behaves in precisely the same manner as the infinite elements described above, however rather than adding an element to the mesh, the condition is applied to the boundary of an existing element. The boundary condition is applied both in shear and normal directions, such that the non-zero imposed stress components are as given in Equation 4.34.

$$\sigma_{11} = -d_p v_1 \quad \sigma_{12} = -d_s v_2 \quad \sigma_{13} = -d_s v_3 \tag{4.34}$$

Here d_p represents a damping coefficient in the normal direction and d_s in the shear direction, and subscripts represent the component directions, where 1 represents the normal direction, 2 and 3 represent the transverse directions. The damping coefficients are calculated using the density and wave speed by:

$$d_p = \rho c_p \tag{4.35}$$

$$d_s = \rho c_s \tag{4.36}$$

where c_p is the dilatational or primary wave speed, and c_s is the shear or secondary wave speed. Although this is a low order non-reflecting boundary condition, and higher order methods have been investigated [58], such methods are not necessary for the scope of this problem and are not available in LS-DYNA. According to the LS-DYNA Theory Manual [51], the acoustic wave speed used to calculate the minimum time step is:

$$c = \left[\frac{4G}{3\rho_0} + \left. \frac{\partial p}{\partial \rho} \right|_s \right]^{\frac{1}{2}} \tag{4.37}$$

and assuming an isotropic elastic material, Equation 4.37 can be simplified to:

$$c = \sqrt{\frac{E(1-\nu)}{\rho(1+\nu)(1-2\nu)}} \tag{4.38}$$

Note it can be shown that Equation 4.38 represents the wave speed for one dimensional wave propagation through an infinite medium, i.e. a dilatational wave under plan strain conditions. This wave speed is therefore used as the value for c_p in the non-reflecting boundary condition in LS-DYNA, as in most cases where the boundary condition is needed there is sufficient material in the direction transverse to the direction of travel of the wave for the plane strain assumption to be valid. However, for the case of one-dimensional wave propagation through a slender bar, the assumption of plane strain is no longer valid, meaning the dilatational wave speed changes to:

$$c_p = \sqrt{\frac{E}{\rho}} \tag{4.39}$$

For a material such as aluminium with a Poisson's ratio of $\nu \approx 0.35$, it can be seen that the dilatational wave speed through a slender bar is slower than that through an infinite medium. This means that the non-reflecting boundary condition will overestimate the stress required to prevent a reflection at the bar end. Figure 4.10 confirms this, showing the results of a simulation in LS-DYNA where a 1 MPa compressive trapezoidal wave travels along a slender bar with a non-reflecting boundary condition on one end. Note that the compressive wave results in a compressive reflection at the non-reflecting boundary due to the over-estimation of the impedance of the bar.

This problem can be solved by constraining the surface nodes of the bar in the radial direction, effectively creating a plane strain condition in the bar. This causes the wave speed to change, as given by Equation 4.38, meaning the non-reflecting boundary behaves as intended and the stress pulse does not reflect off the bar end. However, the radial constraint is not representative of the experiment, as experimentally the wave speed matches that given in Equation 4.39. This problem is solved by adding an extra row of elements at the end of the bar with the cross-sectional mesh matching that the bar exactly. A tied contact is defined between the bar and the extra elements, but while the bar is unconstrained apart from symmetry boundary conditions, the surface nodes of the extra elements are constrained in the radial direction and

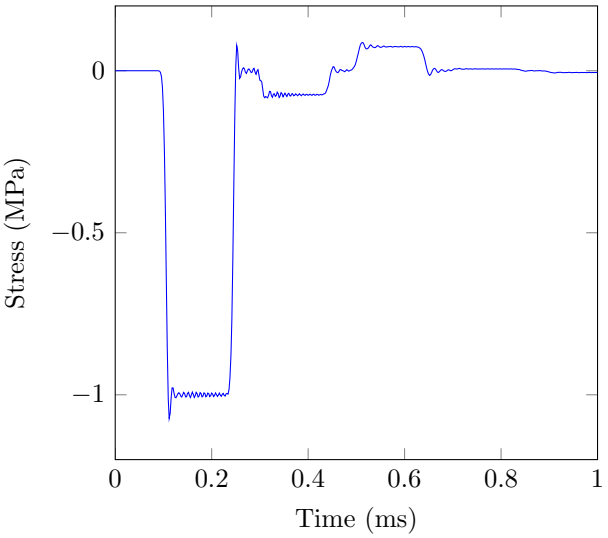

Figure 4.10: An imperfect non-reflecting boundary condition.

a non reflecting boundary condition is added to the free end. This allows the stress pulse to travel through the extra row of elements and not reflect off the free end because of the change in wave speed caused by the radial constraint, thus creating a row of elements which exhibit the same behaviour as infinite elements. However, in order to prevent a reflection as the wave passes from the bar into the infinite elements, the impedances of the bar and infinite elements must be matched, meaning the values for ρcA must be identical. Since the areas are the same, the density of the infinite elements must be the same as that of the bar, and the elastic modulus adjusted as shown in Equation 4.40 such that the wave speed of the bar and infinite elements are identical.

$$E_{mod} = \frac{E(1+\nu)(1-2\nu)}{(1-\nu)} \tag{4.40}$$

Figures 4.11a and 4.11b show the infinite element mesh, and the results of using the infinite elements respectively.

Note that there are very small reflections due to the dispersion in the stress pulse, since the different frequency components of the pulse travel at slightly different wave speeds. However, the reflections are small enough to be considered negligible, and providing the dispersion in the both the experiment and simulation is minimised, any reflections resulting from dispersion of the stress pulse can be ignored.

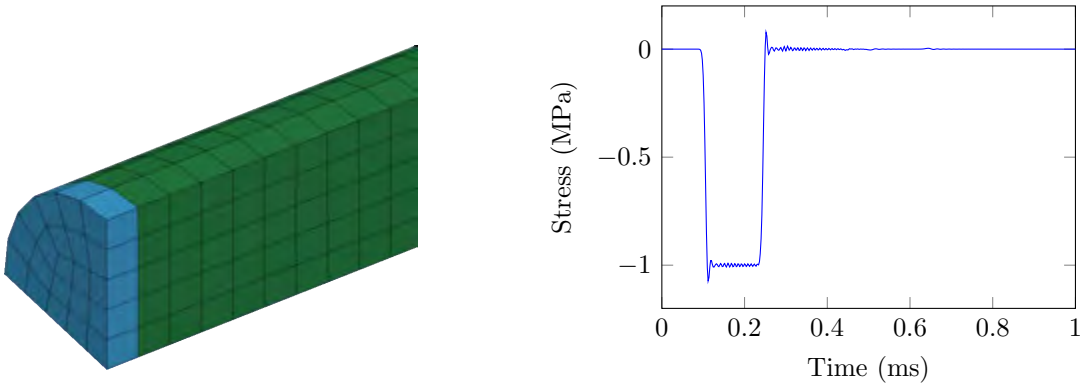

(a) The infinite elements mesh.

(b) The succesfully absorbed stress pulse.

Figure 4.11: The infinite elements concept implemented in LS-DYNA for use with SHPB simulations.

4.3.2 Determining Bar Length

In order to successfully model the SHPB tests using only a portion of the bars, a method of preventing reflections is needed, as described previously, and a sufficient length of the bars must be modelled in order to accurately represent the experiment. To determine the value of this length, a representative model was made consisting of a solid length of bar modelled with linear elastic axisymmetric shell elements, with a reduction in diameter at the centre representing the specimen as shown in Figure 4.12.

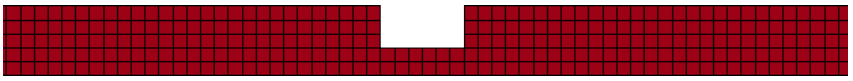

Figure 4.12: A portion of the axisymmetric mesh used to represent a SHPB test.

Each bar has a length of 3 m, while the section representing the specimen has a length of 12mm. Having obtained results using the full apparatus length, simulations were performed with bar lengths of 2m, 1m, 500mm, 300mm, 200mm, and 100mm, after which the results were compared. To minimise the effect of dispersion, the rise and fall of the pulse were defined using a sinusoidal function. The strain reading is taken from the outermost element at the center of each bar, meaning that the signals must be shifted in time such that the stress pulse arrives at the element from which the strain reading is taken at the same time for each simulation. The signal can then be compared to the reference simulation, and the maximum error can be calculated for each bar length, as shown in Figure 4.13a.

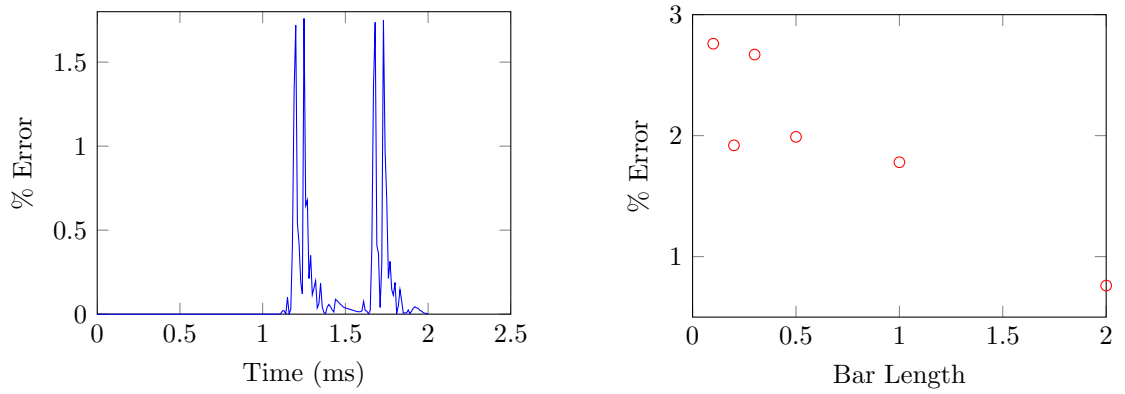

(a) The error for the 200mm bar simulation.

(b) The errors for the different bar lengths.

Figure 4.13: The effect of reducing the length of the bars in a SHPB finite element simulation.

It is unclear why the error is less for the 200mm simulation than the 300mm and 500mm simulations, however the data appears to show an increase in signal error as bar length decreases. Ultimately, a length of 200mm was chosen as the error is within an acceptable bound, and the length is slightly greater than 10 diameters of ⌀19.05mm the bar, which is sufficient to ensure 1D wave propagation conditions [59].

4.3.3 Modelling the Clamps and Specimen

It is important to model the clamps in the bars because the effect of the mass of the clamps on the load transfer between bar and specimen must be taken into account. Similarly to the method used by Verlysen [56], the interfaces between the bar and clamp, as well as the clamp and specimen were modelled as tied contacts between the relevant surfaces. Figure 4.14 shows the specimen interface in the mesh used for the SHPB simulations.

For the clamps, the threaded portion is modelled as a smooth surface to avoid a complicated mesh geometry, and the contact between bar and clamp is defined for the threaded portion only and not the end of the clamp. In order to accommodate the change in geometry of the bar at the portion wherein the clamp is screwed without decreasing the mesh size of the bar, a small section of the bar end is modelled separately and a tied contact defined between the rest of the bar and the bar end. Similarly, the interface between the clamp and specimen is simplified to minimise the mesh complexity. The clamped region of the specimen is modelled as a tapered section with the top line passing through the centres of the lobes, and the contact between the clamp and specimen is defined only on this section and not on the sides or end of the specimen. Simulations were performed to determine the effect of the clamp material, by modelling both

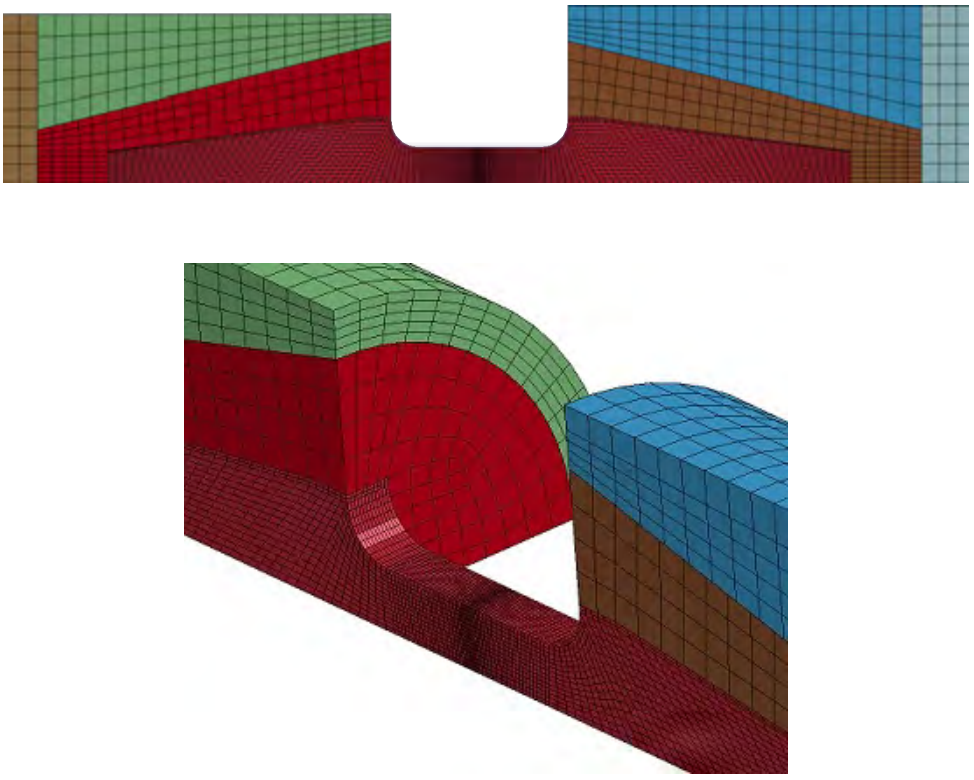

Figure 4.14: The mesh used for the bar ends, clamps and specimen.

an aluminium and titanium clamp and comparing the results, as shown in Figure 4.15. The specimen was modelled as steel with power law plasticity.

Note that a stress overshoot is evident in the input bar (front face), which is consistent with the experimental observations, but the overshoot is not as pronounced in the output bar, which is not true experimentally. It is not clear from the simulation whether the stress overshoot seen experimentally is solely due to the impedance of the clamps. However, it is clear that the effect of clamp material is greatest at yield, and negligible during the majority of the specimen deformation, suggesting that the influence of the clamps on the accuracy of the processed data is small enough to be ignored.

4.4 Damage Model

To calibrate the Bai-Wierzbicki damage model for a single strain rate, a range of local average triaxialities, normalised Lode angles and plastic strains at the point of failure are needed. The data points can be plotted, and a surface can be fitted to the data representing the effective

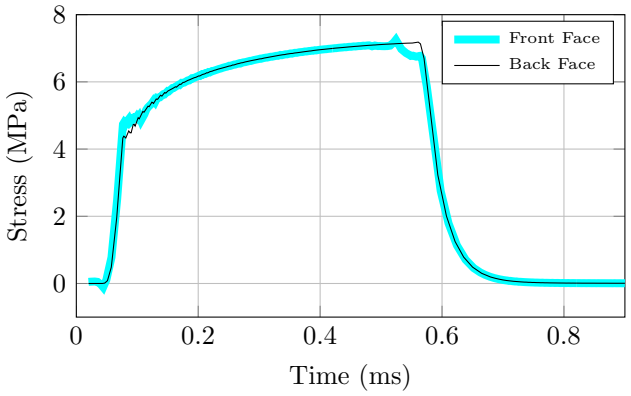

(a) Aluminium clamps.

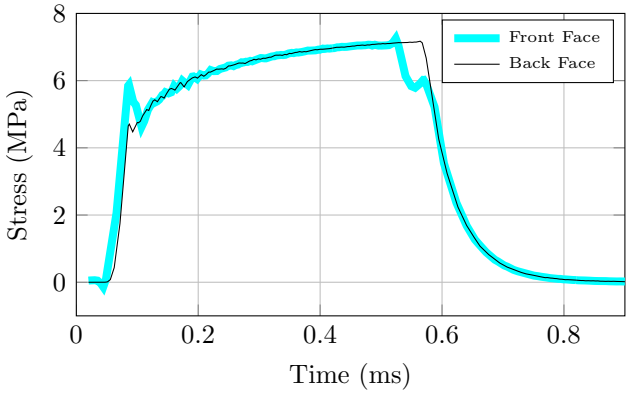

(b) Titanium clamps.

Figure 4.15: The effect of the clamp material on the stresses at the bar ends.

plastic strain as a function of average triaxiality and normalised Lode angle. The function describing the surface is given in Equation 4.41.

$$\varepsilon_f(\eta, \bar{\theta}) = D_1 e^{-D_2 \eta} \left(D_3 \bar{\theta}^2 + D_4 \right) \tag{4.41}$$

Note the chosen equation is essentially the symmetric version of the Bai-Wierzbicki model, since no data is recorded in the negative normalised Lode angle region, so calibrating for a non-symmetric model would be misleading. As mentioned above, the stress state parameters used to determine the strain at failure are averaged, since the damage mechanisms are history dependent. As described in Section 2.2.2, the parameters are strain averaged rather than time averaged, as the plastic strain is the driving force behind the formation of voids and shear bands. Since this dissertation focusses on the effect of strain rate on ductile damage, the average plastic strain rate is also recorded.

$$\eta_{ave} = \frac{1}{\varepsilon^p} \int_0^{\varepsilon_f} \eta \mathrm{d}\varepsilon^p \tag{4.42}$$

$$\bar{\theta}_{ave} = \frac{1}{\varepsilon^p} \int_0^{\varepsilon_f} \bar{\theta} \mathrm{d}\varepsilon^p \tag{4.43}$$

$$\dot{\varepsilon}^p_{ave} = \frac{1}{\varepsilon^p} \int_0^{\varepsilon_f} \dot{\varepsilon}^p \mathrm{d}\varepsilon^p \tag{4.44}$$

To calibrate the model, the element in the finite element model at which failure first occurs is located visually by inspecting the plastic strain field. In the case of all the tests performed in this dissertation, the centre of the specimen is used. From the experimental data, the displacement at which failure occurred is determined by inspection, and the corresponding displacement in the finite element model is used to find the time of failure in the model. Note that a more robust method of determining the element at which failure first occurs, could be to use initial estimates of the damage model parameters to identify the element, and then verify that the same element is the first to fail once the model has been calibrated. If it is not, then the process must be repeated and the element can be found iteratively. However, since the plastic strain, Lode angle, and triaxiality fields were all localised at the same point for the specimens used, this was not necessary for this research.

The average triaxiality and normalised Lode angle are output as history variables, and the values as well as the plastic strain at the time of failure are recorded as data points for each test. The results from all the tests are imported into a Matlab script which fits a surface of the form given in Equation 4.41 to the data.

Chapter 5

Experimental Results

The following chapter presents and analyses the quasistatic and dynamic experimental data obtained during the full range of tests. The results are grouped by specimen geometry and the quasistatic and dynamic tests are compared using both the force-displacement data and a qualitative visual analysis of the specimens post-failure.

Tables 5.1 and 5.2 show the test matrices for the full set of quasistatic and dynamic experiments performed.

Geometry	Cross-head speed (mm/min)	No. of tests
Straight	100	4
Notch (R5.0)	100	4
Notch (R2.5)	100	5
Notch (R1.5)	100	4
Groove (R5.0)	100	4
Groove (R2.5)	100	4
Groove (R1.5)	100	4
Straight	0.6	4
Notch (R5.0)	0.6	4
Notch (R2.5)	0.6	4
Notch (R1.5)	0.6	4
Groove (R5.0)	0.6	4
Groove (R2.5)	0.6	4
Groove (R1.5)	0.6	4

Table 5.1: The quasistatic tests performed at two different cross-head speeds.

Geometry	Average velocity (m/s)	No. of tests
Straight	8.2	6
Notch (R5.0)	7.5	5
Notch (R2.5)	7.3	4
Notch (R1.5)	7.4	4
Groove (R5.0)	6.6	4
Groove (R2.5)	6.8	4
Groove (R1.5)	5.9	4

Table 5.2: The dynamic SHPB tests.

5.1 Straight Specimens

Both the quasistatic and dynamic data sets show consistently repeatable results with very little variation between tests, which is most likely due to the close tolerances achieved during the wire cutting process and the consistent thickness of the DOMEX 355MC steel sheet. All the specimens were cut from the centre of the sheet with no preferred orientation, which suggests that the material is homogeneous and isotropic at the centre of the received sheet at least if not at the boundaries. Encouragingly, the specimens all failed at the centre of the gauge section. The force-displacement data (Figure 5.1) shows a slight rate hardening between the 0.6 mm/min and 100 mm/min tests, which correspond to initial strain rates of approximately 1.4×10^{-3} s^{-1} and 0.2 s^{-1} respectively. The final displacement is very slightly less ($\approx$ 1% difference in displacements) for the faster test than that of the slower test, and the force is also closely grouped but slightly higher for the faster test, suggesting a decrease in ductility with an increase in strain rate.

An inspection of the dynamic strain rate data further reinforces this observation, as the displacement at failure is decreased by approximately 0.5 mm, or 12%, with a similar force at failure.

Note that two of the specimens did not fail, as seen by the two data lines which unload significantly earlier than the rest of the data. Although the data does exhibit an initial stress over-shoot, the spread of data is small and the over-shoot region is of a small enough portion of the total displacement to show the material behaviour. The dynamic strain rate corresponds to approximately 600 s^{-1}, as seen in Figure 5.2, and exhibits a yield stress approximately 30% larger than that of the quasistatic tests, however the hardening rate is lower than that of the quasistatic tests. This could partly be the reason the dynamic tests exhibit less displacement at failure, as necking appears to occur earlier in the dynamic specimens than the quasistatic.

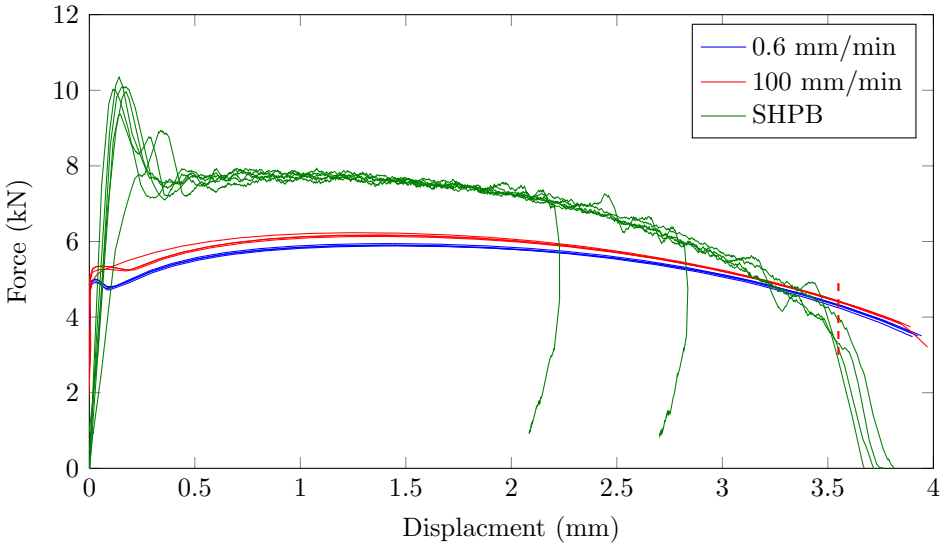

Figure 5.1: The force-displacement data for the straight specimens.

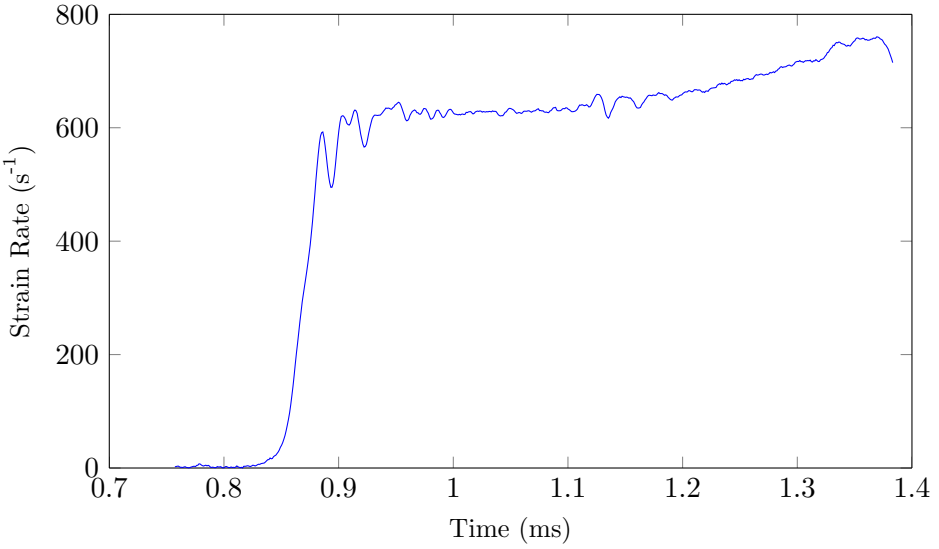

Figure 5.2: The strain rate in a straight specimen calculated using the bar velocities.

The Considére criterion [60] states that necking will occur when the hardening rate is equal to the true stress:

$$\frac{d\sigma}{d\varepsilon} = \sigma \tag{5.1}$$

and since the hardening rate is lower for the dynamic tests than the quasistatic, necking will occur earlier for the dynamic tests as stress will reach the hardening rate much sooner, particularly since the stress is higher in the dynamic tests. This complicates the analysis of the data, as most of the plastic deformation in the local region of failure occurs during the necking phase

of deformation, meaning that the local plastic strain at failure is not necessarily less for the dynamic tests. This is the reason numerical simulations are required to determine the local plastic strain in the region of failure. However the data can be qualitatively analysed by examining the failed specimens, seen in Figure 5.3.

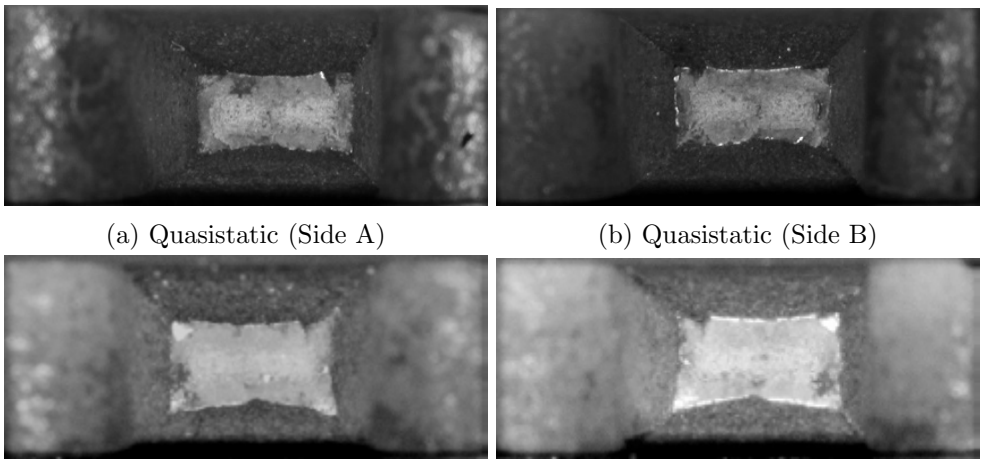

(a) Quasistatic (Side A) (b) Quasistatic (Side B)

(c) Dynamic (Side A) (d) Dynamic (Side B)

Figure 5.3: Straight specimens post-failure viewed down the longitudinal axis of the specimens.

Note that the specimens from the dynamic tests have larger areas at the failure surface, which suggest a lower strain at failure, which is consistent with the initial observations made from the force-displacement data.

5.2 Notched Specimens

The notched specimens fail at significantly lower displacements than the straight specimens due to the smaller area at the centre of the gauge section, which is half that of the straight specimen. Due to the notch, the strain field is localised at the centre of the specimen as soon as the specimen begins deforming, meaning that the gauge length used to determine the stress and strain from the force-displacement curve would be at best an estimate. For this reason, comparing the displacements at failure for the different notch radii would be extraneous, as the effective gauge lengths for the different radii are different, meaning that it is not possible to directly compare the strains at failure by comparing the displacements at failure. However, strain rate effects can observed for each specimen.

5.2.1 R5.0mm Notch

The R5.0mm notched specimens have the lowest triaxiality of the notched specimens, which should translate to increased ductility in comparison to the smaller radii notched, but less ductility than the straight specimens. The data (Figure 5.4) exhibits behaviour similar to that of the straight test data, but with lower displacements as expected.

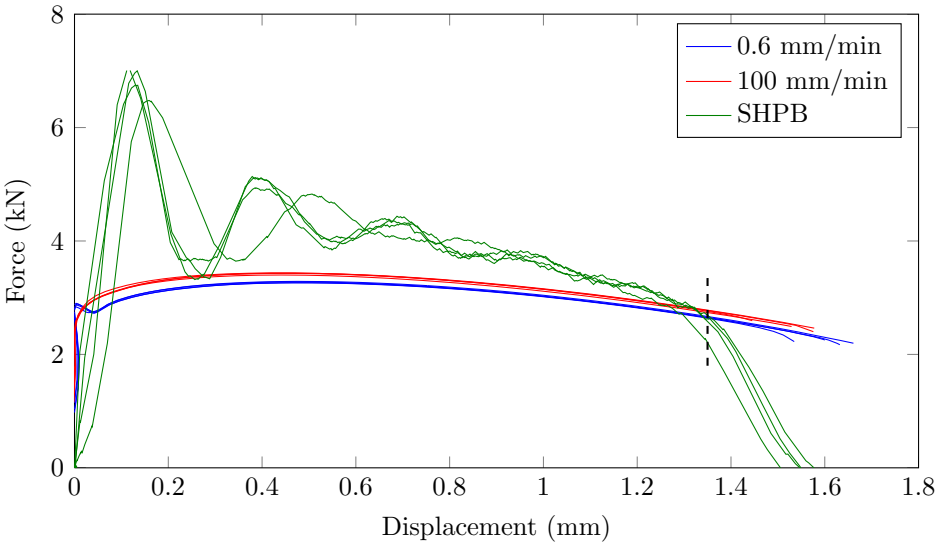

Figure 5.4: The force-displacement data for the R5.0mm notched specimens.

Note that the strain rate effect is very similar to that of the straight specimens, with the faster quasistatic tests displaying a slightly higher strength than that of the slower tests, and the dynamic tests showing an increase in strength in the region of 30%. Additionally, the faster quasistatic tests fail at a lower displacement than the slower tests, and the dynamic tests fail at a lower displacement than both, as indicated by the dashed line.

The initial transient behaviour exhibited by the SHPB tests is more pronounced in the notched specimens as it lasts for a greater portion of displacement, and the force over-shoot is a larger fraction of steady-state force. The reason the transient solution appears to be present for a greater portion of the duration of each test, is that failure occurred in the specimen much earlier than in the straight specimens. As can be seen in Figure 5.5, the length of the transmitted stress pulse is only approximately half that of the incident pulse, meaning that providing the transient behaviour lasts for the same amount of time as in the straight tests, the portion of the duration of the test where the transient behaviour dominates will double from the straight to the notched tests.

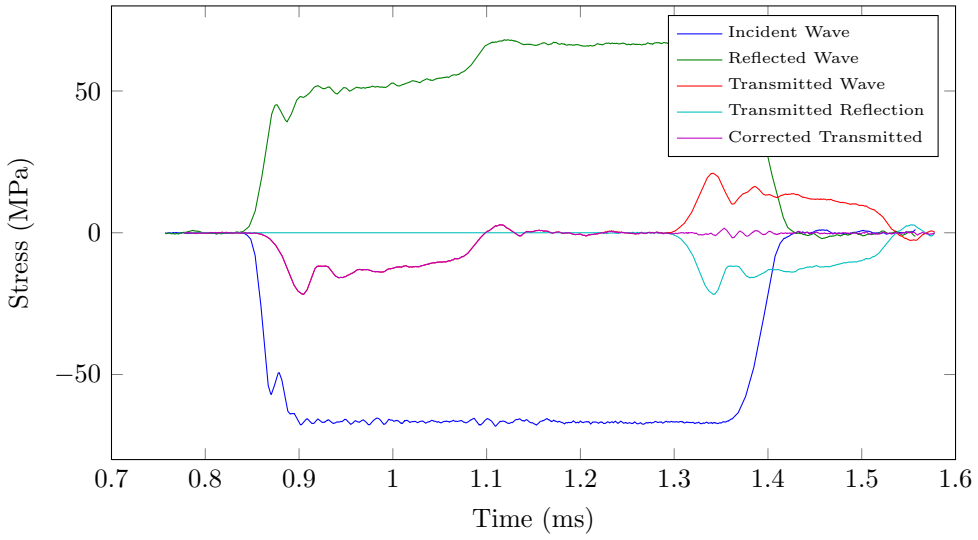

Figure 5.5: The incident, reflected and transmitted signals for a R5.0mm notched specimen.

5.2.2 R2.5mm Notch

The R2.5mm notched specimens exhibit very similar behaviour to those with larger notches, although the displacement at failure is lower, which is to be expected as the region of deformation is more localised due to the smaller notch radius. Figure 5.6 shows the displacement at failure for the 100 mm/min tests is not distinctly less than that of the 0.6 mm/min tests, as is the case with the R5.0mm notched tests, but the rate effects are very similar.

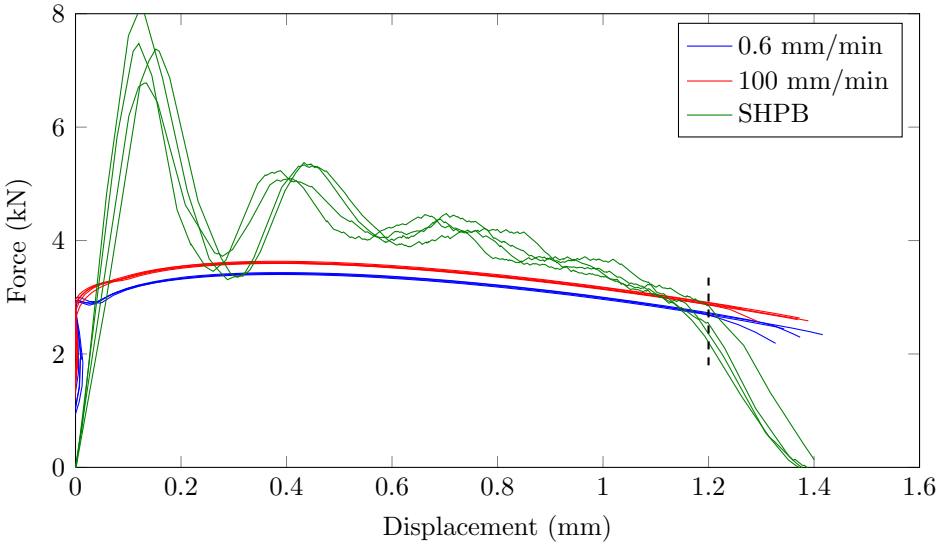

Figure 5.6: The force-displacement data for the R2.5mm notched specimens.

The dynamic data is also very consistent with the R5.0mm specimens, but also showing a lower displacement at failure (1.2mm) which again is significantly lower than that seen in the

quasistatic data.

5.2.3 R1.5mm Notch

The R1.5mm specimens deform under the highest triaxiality due to the small notch radius, meaning they should exhibit the least ductility. Although the quasistatic and dynamic data (Figure 5.7) shows a significant decrease in displacement at failure in comparison to the R5.0mm and R2.5mm specimens, as discussed previously the deformation is more localised, and so observation regarding the local strain at failure cannot be inferred.

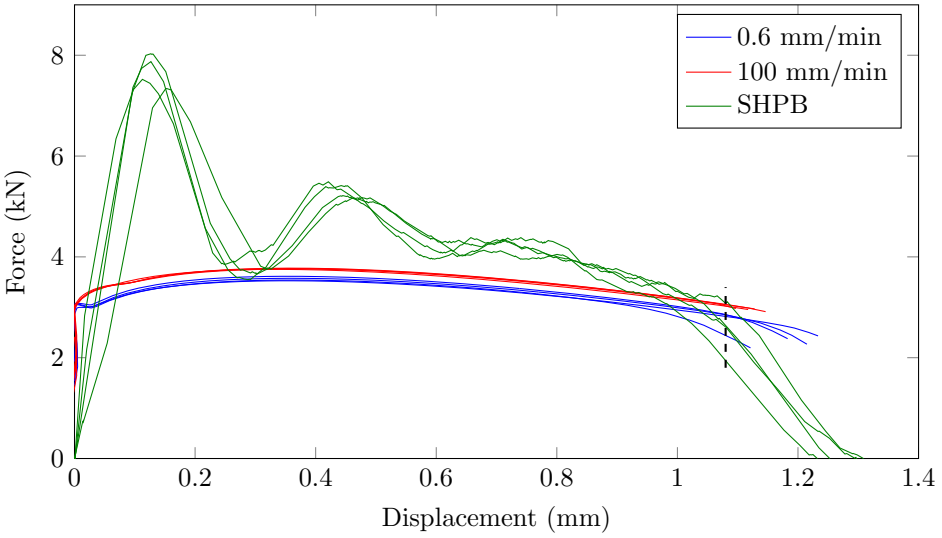

Figure 5.7: The force-displacement data for the R1.5mm notched specimens.

Note that the maximum force is noticeably larger than that of the R5.0mm specimens, and on closer inspection the R2.5mm specimens yield a maximum force between the two sets of data. This is most likely because of the more localised strains for the smaller radii, as a more localised strain field will result in a higher local strain rate for the same boundary velocity. Since the material exhibits an increase in strength with an increase in strain rate, the smaller radii notches will harden more due to the higher local strain rates.

Figure 5.8 shows a comparison of the notched specimens from the quasistatic tests post-failure. The difference between the sizes of the failed surfaces is not obvious, although the area of the failure surface for the R1.5mm specimen does appear slightly larger than that of the R5.0mm specimen.

However, comparing the failure surfaces from the quasistatic tests to those from the dynamic tests, as seen in Figure 5.9, it is clear that the corresponding failure surface areas are larger

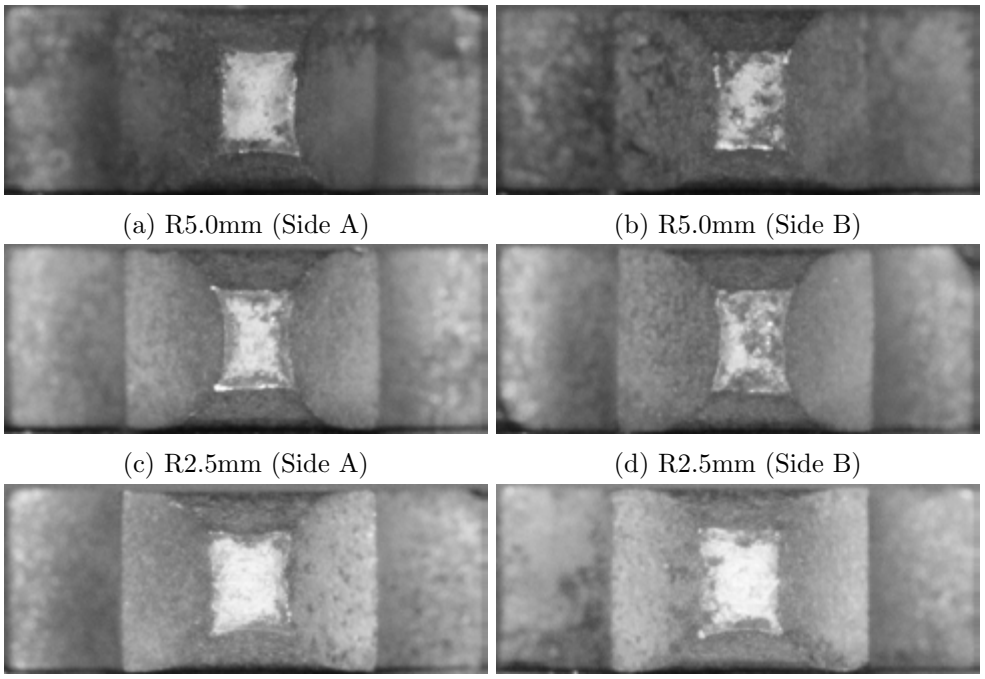

(a) R5.0mm (Side A) (b) R5.0mm (Side B)

(c) R2.5mm (Side A) (d) R2.5mm (Side B)

(e) R1.5mm (Side A) (f) R1.5mm (Side B)

Figure 5.8: Notched specimens from SHPB tests post-failure.

from the dynamic tests, which further reiterates the observation that an increase in strain rate causes a decrease in ductility.

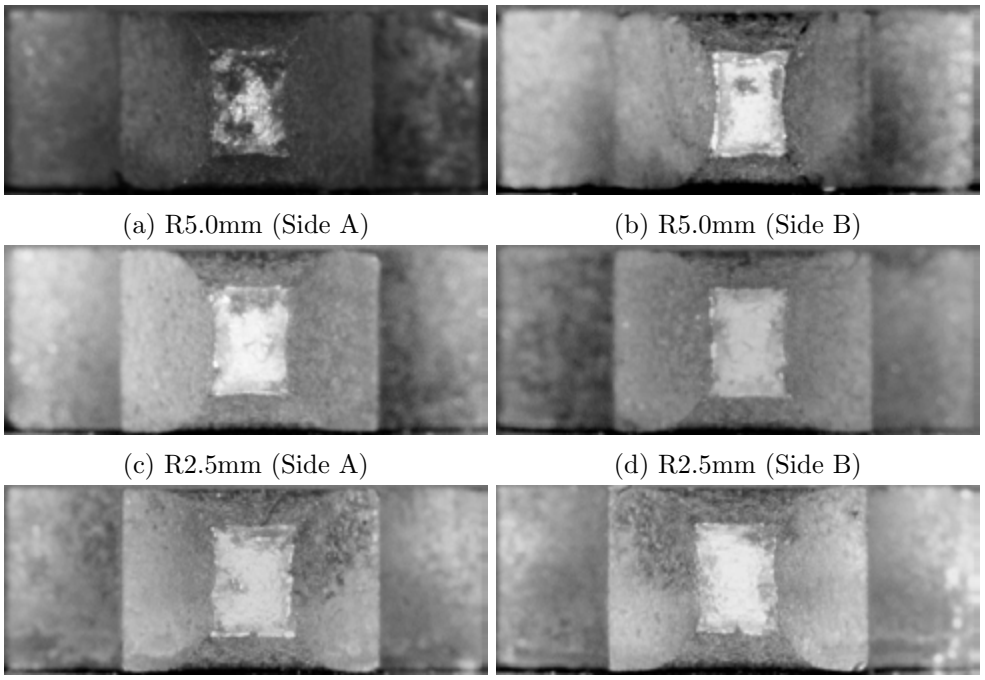

(a) R5.0mm (Side A) (b) R5.0mm (Side B)

(c) R2.5mm (Side A) (d) R2.5mm (Side B)

(e) R1.5mm (Side A) (f) R1.5mm (Side B)

Figure 5.9: Notched specimens from SHPB tests post-failure.

5.3 Grooved Specimens

Testing and analysing the deformation of the grooved specimens was more problematic than the other specimens as the strain is highly localised at the centre of the specimen, meaning the displacement to failure is small in comparison to the other tests. This poses a problem for the quasistatic tests, as the elastic deformation component of the displacement is of the same order of magnitude as the plastic component, which makes it difficult to determine the stiffness of the test and separate the components. The difficulty with the dynamic tests lies in the fact that the SHPB tests were tested such that the boundary velocities were similar throughout all the test geometries. However, as discussed regarding the notched specimens, the specimens fail much earlier, which intensifies the effect of the initial transient behaviour of the transmitted stress pulse. This makes it difficult to analyse the data from the grooved specimens, particularly when determining the point at which the specimen failed. The results for the different groove radii are shown in the following sections. Note that the results for the 100 mm/min tests are not included, as the specimens failed too quickly for the data acquisition unit to correctly capture the force-displacement data.

5.3.1 R5.0mm Groove

The most noticible characteristic of the quasistatic data (Figure 5.10) for the R5.0mm grooved specimens is that there is a much larger variation in strength than any of the other tests. This could possibly be due to the handling of the specimens before testing, as the minimum thickness of the groove cross section is only 1mm, which results in a very low bending stiffness in the region of maximum deformation. During the process of screwing the specimens into the tensile adaptors, it is possible that a small amount of bending occurred, hardening the specimen slightly before the test began.

However, the tests still exhibit a range of displacements at failure larger than that of the smaller radius grooves. The dynamic data shows a smaller variation in results, but the oscillations caused by the test apparatus dominate the response, making it very difficult to locate the point at which failure occurred.

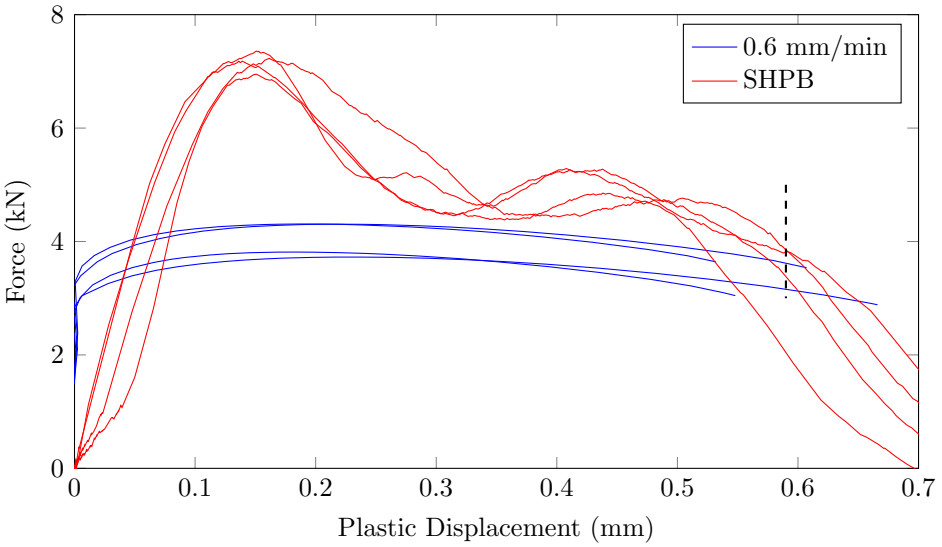

Figure 5.10: The force-displacement data for the R5.0mm grooved specimens.

5.3.2 R2.5mm Groove

The quasistatic R2.5mm grooved specimen tests showed much more repeatability in the results (Figure 5.11), showing one outlier which hardened more than the rest of the tests.

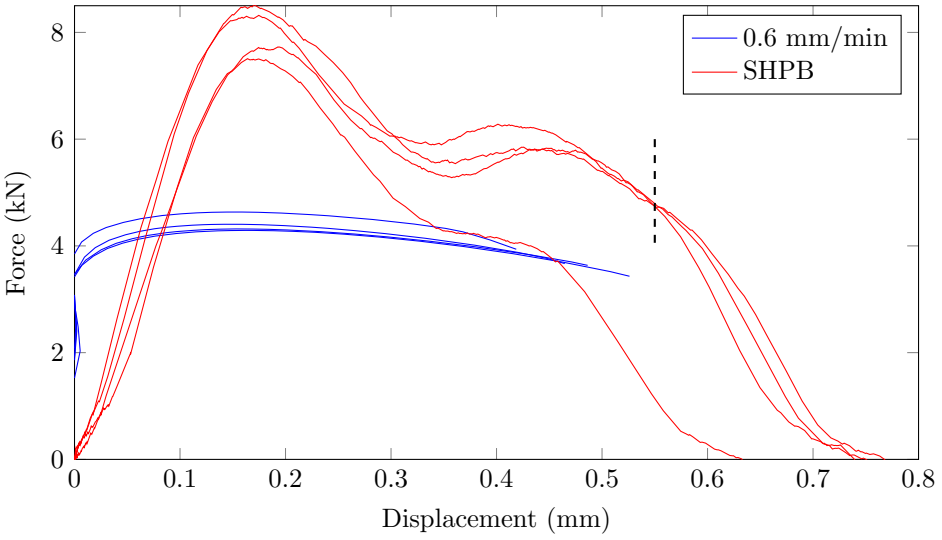

Figure 5.11: The force-displacement data for the R2.5mm grooved specimens.

Similarly, the dynamic test data showed repeatable results, with a single outlier which hardened less than the rest of the tests. Like the notched specimens, the specimens with smaller groove radii exhibit lower displacements at failure and greater hardening strength due to the increase in localisation of the strain fields.

5.3.3 R1.5mm Groove

The quasistatic data for the R1.5mm specimens (Figure 5.12) shows very good repeatability both in terms of the variation in the force-displacement curves, and the displacements at failure. Interestingly the displacement at failure is not significantly less than that of the R2.5mm tests, and on average is actually greater than some of the R2.5mm tests.

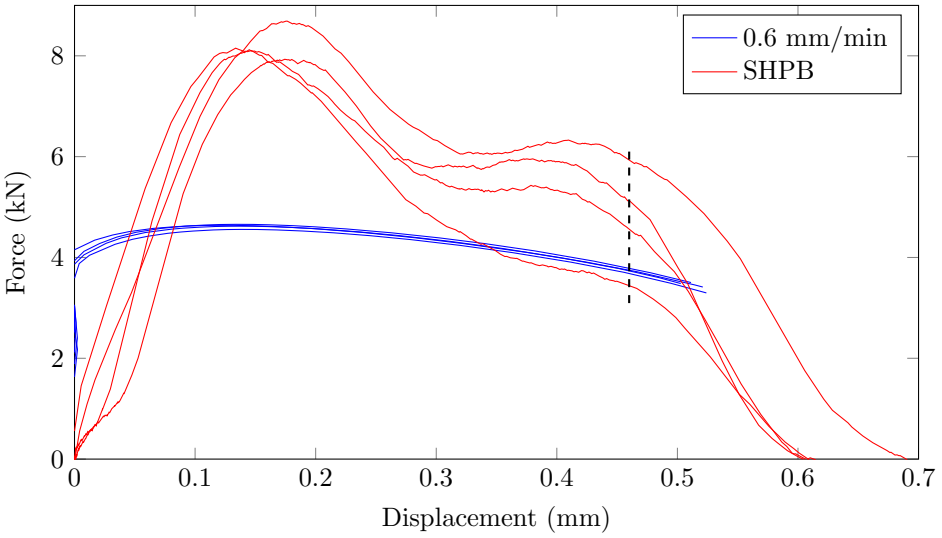

Figure 5.12: The force-displacement data for the R1.5mm grooved specimens.

Figure 5.13 shows a comparison of the failure surfaces for the different groove radii tested at quasistatic strain rates. Visually, the R1.5mm specimen has a noticeably larger surface area at the point of failure than the other specimens, which suggests a lower strain at failure, while the surface areas of the failure surfaces for the R2.5mm and R5.0mm tests are not as noticeably different to one another.

Note that the surface finish of the groove, by visual inspection, is considerably better for the R1.5mm specimen, since the specimen had to be milled using more passes due to the size of the cutter used. This could have some effect on response of the specimen, and may explain why the quasistatic data for the R1.5mm specimens was so much more repeatable than the other grooved specimens.

The dynamic data is slightly more spread than the data from the other geometries, but still exhibits failure at very similar displacements which is encouraging.

Figure 5.14 shows a comparison of the grooved specimens from the SHPB post-failure. A visual inspection of the failure surfaces suggests the surface areas of the failure surfaces decreases as

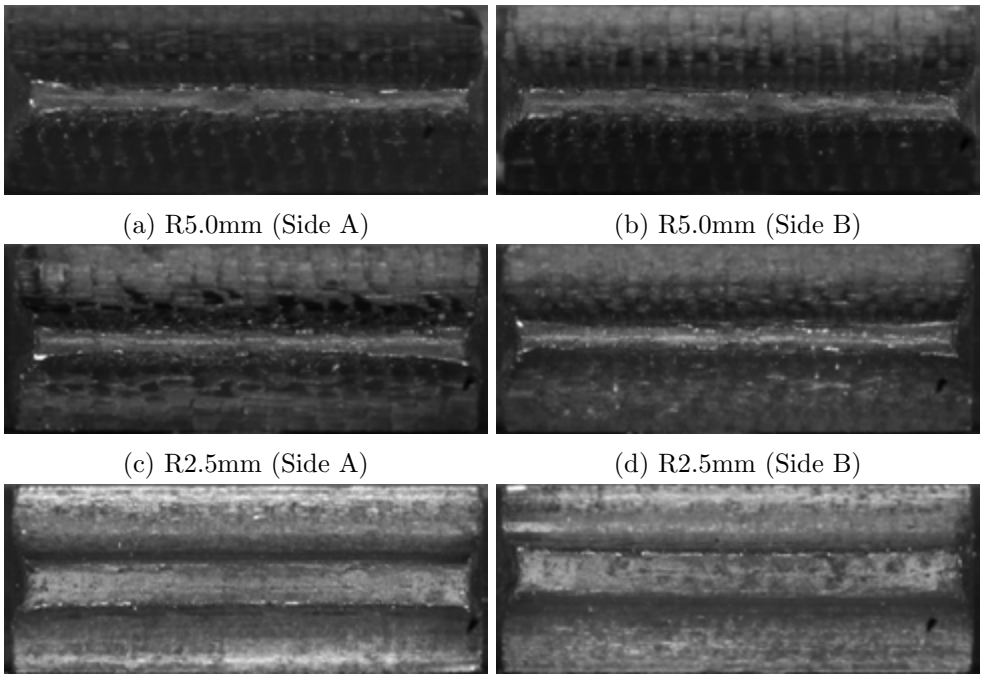

(a) R5.0mm (Side A) (b) R5.0mm (Side B)

(c) R2.5mm (Side A) (d) R2.5mm (Side B)

(e) R1.5mm (Side A) (f) R1.5mm (Side B)

Figure 5.13: Grooved specimens from quasistatic tests post-failure.

the radius increases, which suggests an increase in ductility with an increasing radius. This is consistent with theory that an increase in hydrostatic tension in the specimen will decrease the ductility.

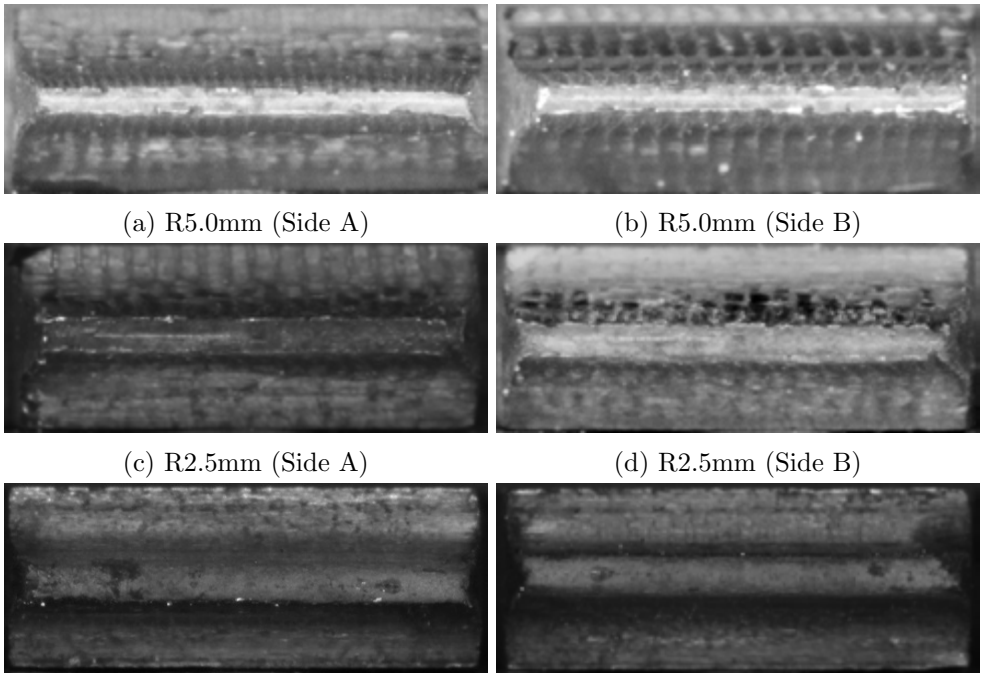

(a) R5.0mm (Side A) (b) R5.0mm (Side B)

(c) R2.5mm (Side A) (d) R2.5mm (Side B)

(e) R1.5mm (Side A) (f) R1.5mm (Side B)

Figure 5.14: Grooved specimens from SHPB tests post-failure.

Visually, a difference can be seen between the failure surfaces for the R2.5mm specimen at quasistatic and dynamic strain rates. The failure surface is larger with straighter edges for the dynamic rate, while at the quasistatic rate the specimen thins toward the centre of the failure surface. This is consistent with previous observations suggesting a decrease in ductility with increasing strain rate.

Chapter 6

Numerical Results

6.1 Plasticity Model

As described in Section 4.1.5, the plasticity model is calibrated using several steps. The strain hardening function is calibrated using the force-displacement data from the slowest quasistatic tests, while the strain-rate function is calibrated using the change in yield stress for the various different strain rates, and the temperature dependence function is taken from literature.

6.1.1 Strain Rate Dependency

Using the three different different test speeds, a relationship between yield stress and strain rate is determined. The strain rate can be estimated using the boundary velocity and the gauge length:

$$\dot{\varepsilon} \approx \frac{v}{L} \tag{6.1}$$

Note that because the material exhibits an upper and lower yield point, and the SHPB tests exhibit a stress overshoot at yield, the yield stress cannot be read directly off a stress-strain curve. For this reason, the stress-strain data was extrapolated from the point after the lower yield point to the region of elastic deformation in order to estimate the yield stress required by the constitutive model. Figure 6.1 shows the yield stress taken from experimental data plotted against the logarithmic strain rate. A similar concept is illustrated in Figure 2.2. Note that

an extra data point is added corresponding to a boundary velocity of 2 mm/min. This data was taken from an extra test which was performed to ensure the quasistatic test procedure was performing as expected.

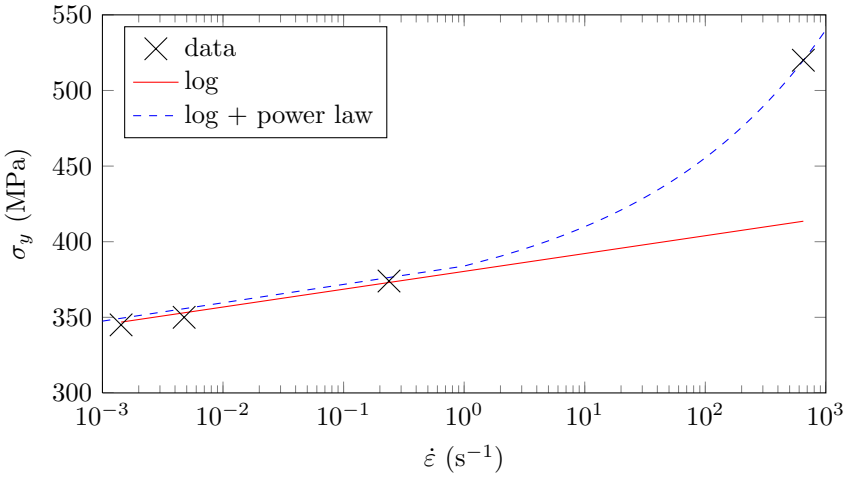

Figure 6.1: The effect of strain rate on the yield stress.

The data shows a linear relationship on the logarithmic scale between strain rate and stress in the quasistatic strain rate range. However, as discussed by Zhao [13], the effect of strain rate on the yield stress is greater as the strain rate enters the dynamic region. Adding the power law term yields a better fit to the data throughout the full range of strain rates. Equation 6.2 gives the function used describing the yield stress (excluding any temperature effects).

$$\sigma_y = \bar{\sigma}_y + A \cdot ln\left(\frac{\dot{\varepsilon}}{\dot{\varepsilon}_0}\right) + B\dot{\varepsilon}^k \tag{6.2}$$

Note that the reference strain rate, $\dot{\varepsilon}_0$, was taken as 0.001s^{-1} such that the effect of strain rate would be close to zero at the lowest strain rate tested, which was close to 0.001s^{-1}, although traditionally 1s^{-1} is used [11–13]. Below the reference strain rate, the function is set equal to zero to avoid very low or even negative flow stresses in elements with strain rates close to zero. The constants were verified by using the estimated values in simulations and comparing the results to the experimental data, after which small adjustments were made to obtain a better fit to the experimental data at the yield point. The final values used for the constants in the material model are given in Table 6.1.

A (MPa)	B (MPa)	k
5.8	15	0.3

Table 6.1: The constants used for the Zhao rate dependency function.

6.1.2 The Strain Hardening Function

Determining the parameters for any form of strain hardening curve requires data showing a relationship between true stress and plastic strain. However the specimen geometry required for SHPB tests is not conducive to accurately converting force-displacement data to stress-strain data. This is because due to the length of the specimen the strain field is much less uniform throughout the gauge length of the specimen than that of a standard dogbone specimen, and necking occurs earlier. This means that the gauge length, required for converting displacement to strain, must be estimated to determine a stress-strain relationship, and any resulting stress-strain curve is only valid before necking occurs, which corresponds to a very small plastic strain range. Figure 6.2 shows the non-uniform plastic strain field generated in a SHPB specimen shortly after yielding.

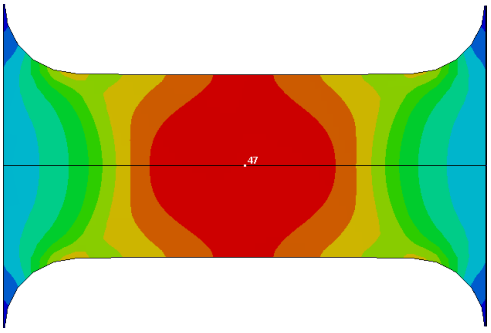

Figure 6.2: The plastic strain field in a SHPB specimen shortly after yielding.

A more reliable solution is to simulate the test from which the experimental force-displacement data is gathered, and compare the experimental and numerical force-displacement curves. Using an optimisation routine, the constitutive parameters can be adjusted such that the curves match as closely as desired. LS-OPT is used to generate a number of simulations, each with different values for the material model parameters, and compare the mean square error (MSE) between the experimental and numerical force-displacement curves for the different combinations of values used for the material parameters. An objective function is generated defining the MSE as a function of the different parameters which are varied in the optimisation routine. The strain hardening function taken from the Zhao model is a power law plasticity relationship given by:

$$\bar{\sigma}(\varepsilon) = C_1 + C_2\varepsilon^n \tag{6.3}$$

where ε is the plastic strain. The data used in the optimisation routine was taken from the experimental data post-yield, such that the initial yielding behaviour will not affect the results, since the power law plasticity model cannot capture the upper and lower yield point behaviour. The optimised values are given in Table 6.2.

C_1 (MPa)	C_2 (MPa)	n
301.5	555.4	0.407

Table 6.2: The constants used for the Zhao strain hardening function.

Having determined the material parameters for the hardening function, the 100 mm/min test was simulated and the resulting force-displacement curve compared to the experimental data as shown in Figure 6.3a. As can be seen, the experimental data does not fit the numerical data well, which is why the extra term in the Zhao rate dependency function was introduced. The full Zhao model, excluding temperature dependency, is given as:

$$\bar{\sigma} = C_1 + C_2\varepsilon^{n_1} + (C_3 - C_4\varepsilon^{n_2}) \cdot ln\left(\frac{\dot{\varepsilon}}{\dot{\varepsilon}_0}\right) + C_5\dot{\varepsilon}^k \tag{6.4}$$

The term $C_4\varepsilon^{n_2}$ allows for a decrease in hardening rate as the strain rate increases. Values for C_4 and n_2 were chosen such that the correlation between experimental and numerical data for the 100 mm/min tests was acceptable. Figure 6.3b shows the improvement in correlation achieved by including the extra term in the strain rate dependency function.

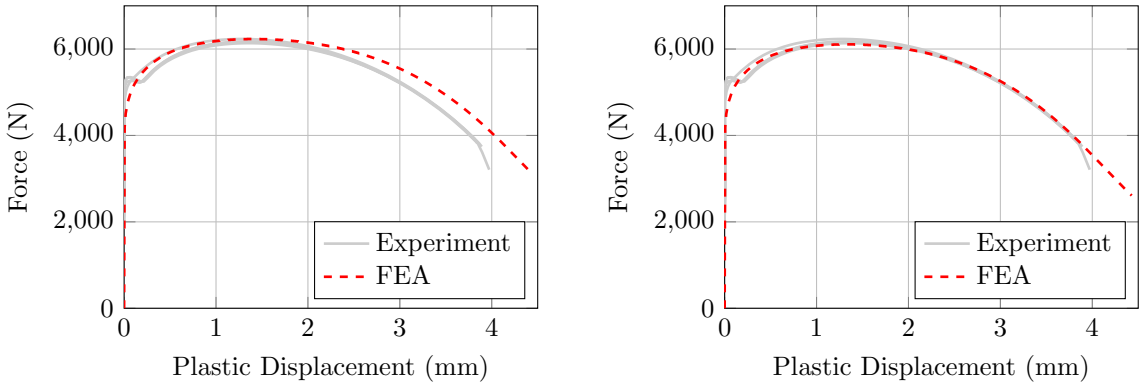

(a) $C_4 = 0.0$ MPa (b) $C_4 = 5.0$, $n_2 = 0.45$.

Figure 6.3: The effect of adding in the term $C_4\varepsilon^{n_2}$ to the Zhao rate dependency function.

The final parameter values used in all the numerical are given in Table 6.3.

The temperature dependency function was taken from the Johnson-Cook plasticity model, given by:

C_1 (MPa)	C_2 (MPa)	n_1	C_3 (MPa)	C_4 (MPa)	n_2	$\dot{\varepsilon_0}$ (s^{-1})	C_5 (MPa)	k
301.5	555.4	0.407	5.8	5.0	0.45	0.001	15.0	0.3

Table 6.3: The constants used for the Zhao plasticity model.

$$f(T) = \left(\frac{T - T_{ref}}{T_m - T_{ref}} \right)^m \tag{6.5}$$

and the values for the parameters taken from the parameters calibrated by Johnson and Cook for Armco-Iron [11], as given in Table 6.4.

T_{ref} (K)	T_m (K)	m	c_p (J/kgK)
293	1811	0.9	452

Table 6.4: The constants used for the Johnson-Cook temperature dependency function.

Note that the value used for m was varied from the value used in the literature (0.55) in order to obtain a better fit to the data at the dynamic rate, as the softening due to temperature in the specimen occurred too early during deformation, and caused an underestimation of the force. Figure 6.4 shows experimental and numerical data is shown over the full range of strain rates for the straight specimens.

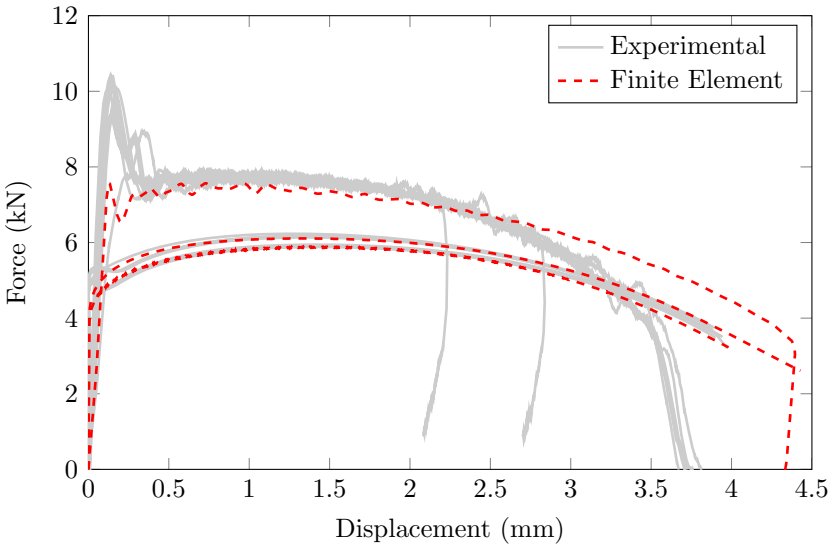

Figure 6.4: The numerical results over the full range of strain rates for the straight specimens.

Note that the model overestimates the force during the latter stage of deformation for the dynamic tests. Numerous attempts were made to address this problem by changing both the temperature dependency exponent, m, and the rate dependency parameters, however it was found that a trade-off between accuracy during the early stages of deformation and accuracy

during the latter stages of deformation had to be made, and so it was decided that obtaining accuracy during as large a portion of the deformation as possible was preferable, such that the stress state evolution was as accurate as possible. It is possible that some mechanism causing a change in deformation behaviour during the latter stages of deformation at high strain rates is present but not accounted for in the constitutive model, but is beyond the scope of this investigation.

6.2 Damage Model

Once the plasticity model has been satisfactorily calibrated, the calibration of the damage model can begin, for which a simulation for each test configuration is required. For 7 different specimen geometries and 3 different test velocities, the damage model calibration requires 21 different simulations. The simulations are compared to the experimental data, and the time at which the displacements are matched is found and used to determine the effective plastic strain as well as the average triaxiality, Lode angle and plastic strain rate at failure. Using this data, the damage model is calibrated for the 0.6 mm/min tests, and the effect of strain rate is then examined both qualitatively and quantitatively.

6.2.1 Simulation Results

Figures 6.5 to 6.10 show the fit of the calibrated plasticity model to the notched and grooved tests.

The numerical data fits the experimental data very well for the notched specimens. Interestingly the model yields a very good fit for the 0.6 mm/min tests, slightly underestimating the force initially but matching most of each force-displacement curve, but underestimates the force for the 100 mm/min test. The model matches the dynamic tests well, slightly overestimating the force in the latter stages of deformation, which is similar behaviour to the straight tests and so is to be expected.

In contrast to the notched tests, the model significantly overestimates the force for the groove tests, and is difficult to analyse for the dynamic tests due to the dominant oscillations in the experimental data. This could possibly be due to the effect of the Lode angle. Bai and Wierzbicki

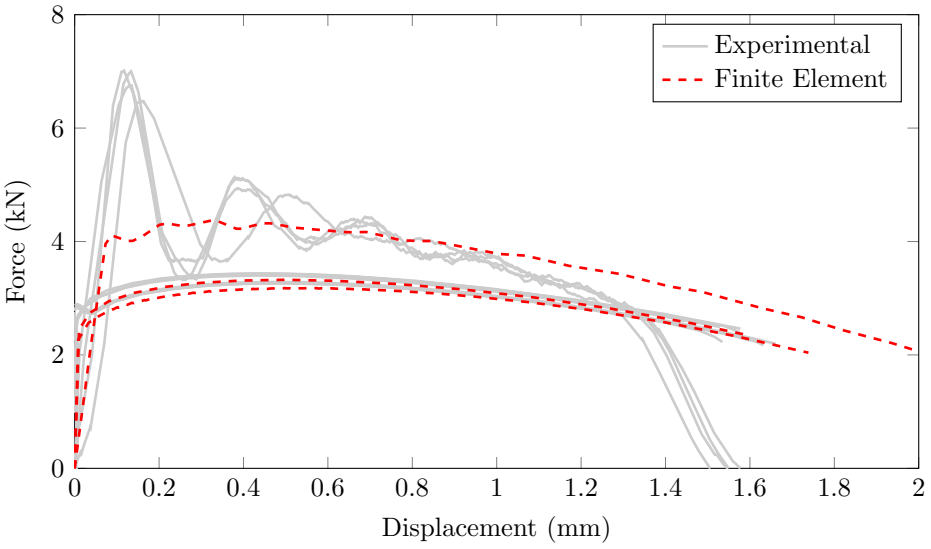

Figure 6.5: The experimental and numerical data for the R5.0mm notched specimen.

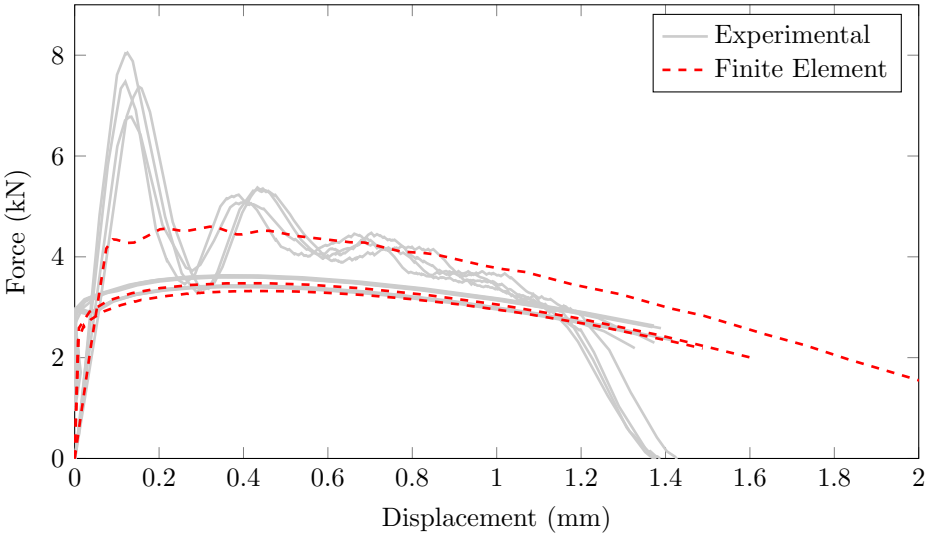

Figure 6.6: The experimental and numerical data for the R2.5mm notched specimen.

[8] proposed a yield surface which takes into account the effects of both pressure and Lode angle, as shown in Figure 6.11a.

This surface results in a lower flow stress for $\bar{\theta} = 0$ than $\bar{\theta} = 1$, which would reduce the force in the grooved specimen simulations. Figure 6.11b shows the effect of the Lode angle correction on grooved specimen simulations. The effect of including Lode angle and pressure dependence on the plasticity behaviour is not investigated in this dissertation, and would need to be analysed to determine whether or not it is the cause of the relatively poor fit of the plasticity model to the grooved specimen test data. However, the maximum error is within 15%, and so the model is deemed accurate enough to at least identify trends in the effect of strain rate on ductile fracture.

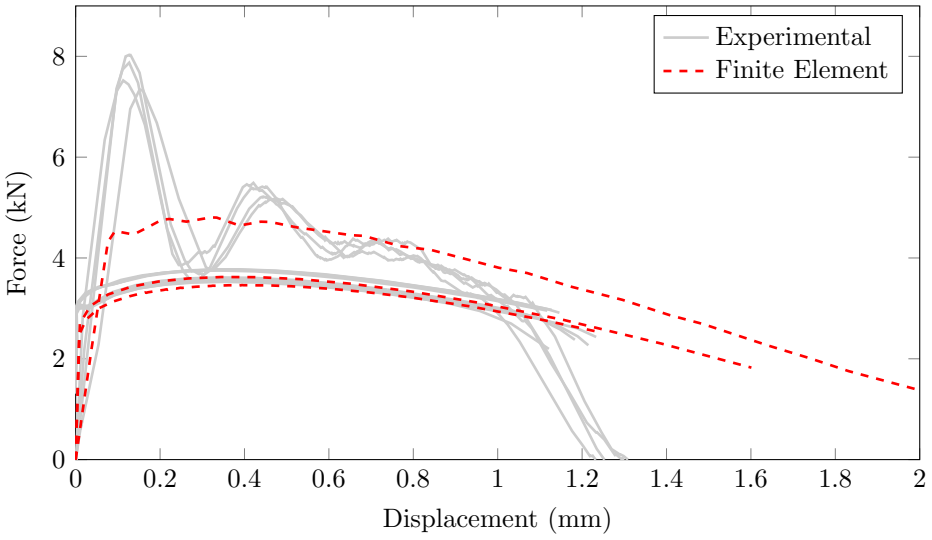

Figure 6.7: The experimental and numerical data for the R1.5mm notched specimen.

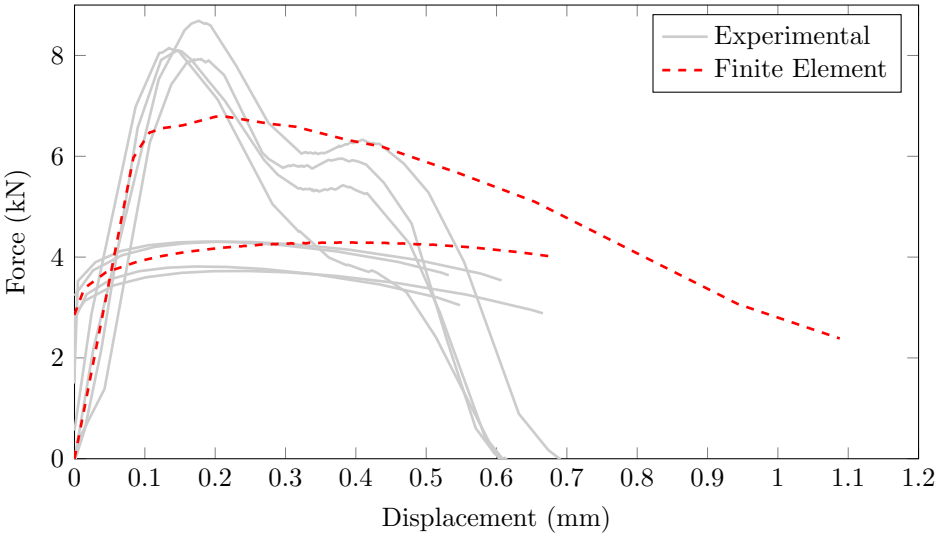

Figure 6.8: The experimental and numerical data for the R5.0mm grooved specimen.

6.2.2 Loading Range

As described in Section 3.1.2, the initial triaxiality and Lode angle can be estimated for each test, but will not be constant throughout the test, which results in a variation in the actual average values at failure from the initial estimated values. Figure 6.12 shows the average values taken from the simulations at the point of failure for the full range of tests.

Note that the triaxialities are all higher than the initial estimates, while the Lode angles are higher for the grooved specimens and lower for the straight and notched specimens. Figure 6.13 illustrates the triaxiality and Lode angle evolutions for the R1.5mm notched and grooved specimens.

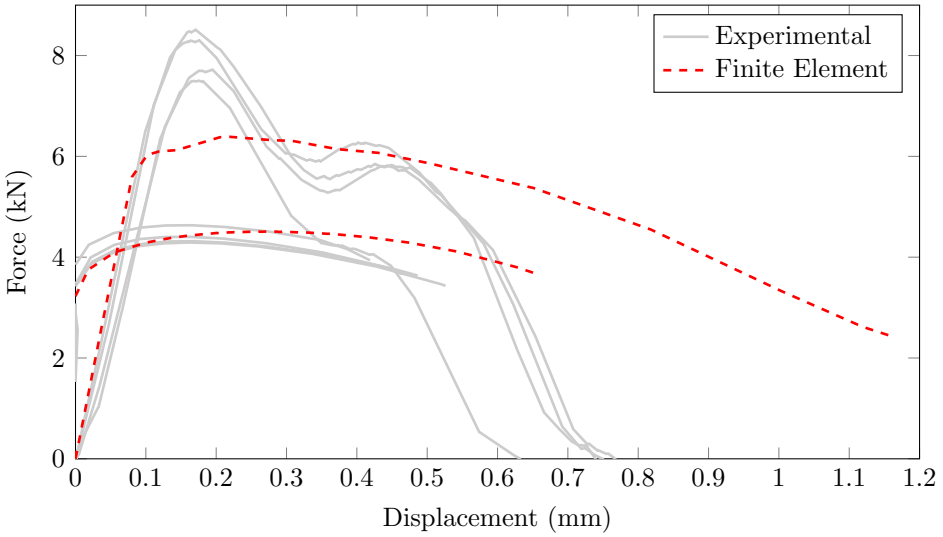

Figure 6.9: The experimental and numerical data for the R2.5mm grooved specimen.

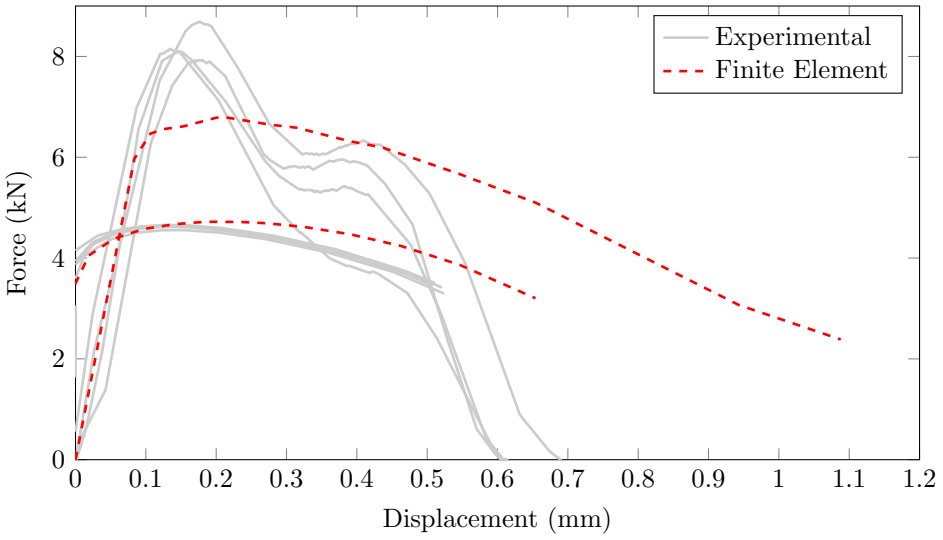

Figure 6.10: The experimental and numerical data for the R1.5mm grooved specimen.

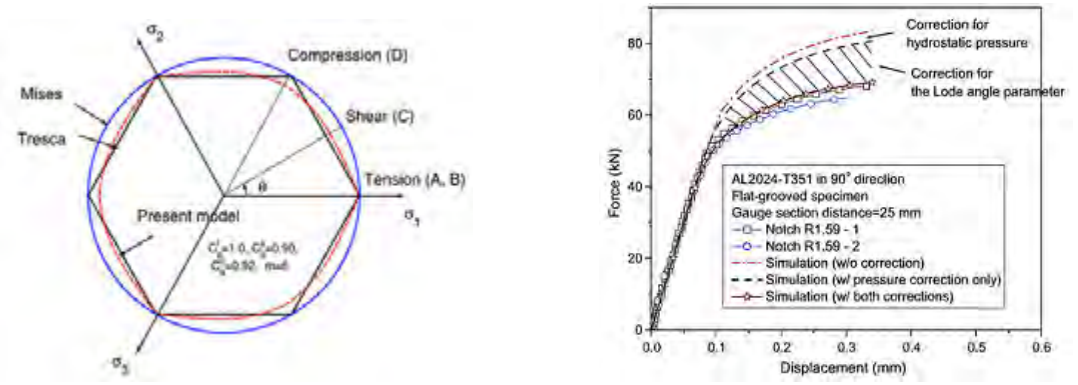

(a) The yield surface proposed by Bai and Wierzbicki [8].

(b) The effect of including Lode angle correction on grooved specimen simulations [8].

Figure 6.11: The pressure and Lode angle modified yield surface proposed by Bai and Wierzbicki.

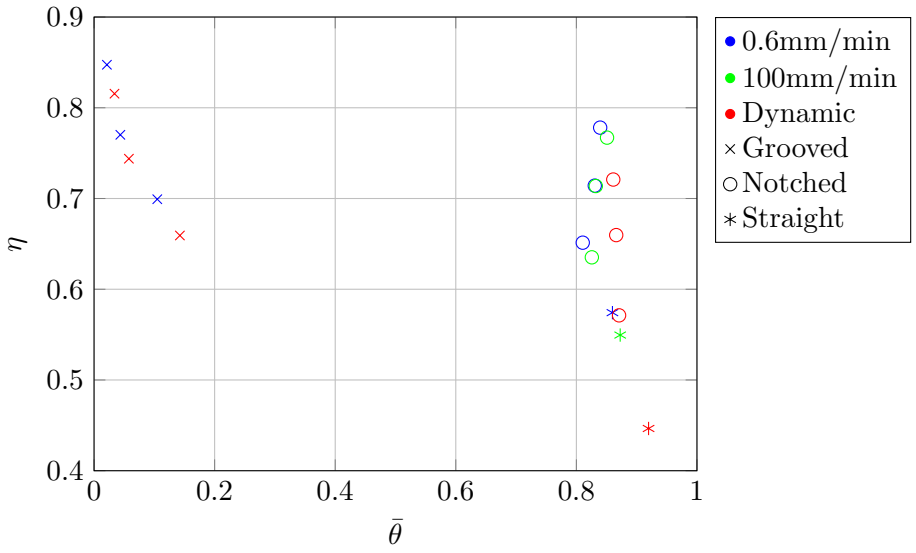

Figure 6.12: The average triaxiality and Lode angle taken from the numerical simulations for each test.

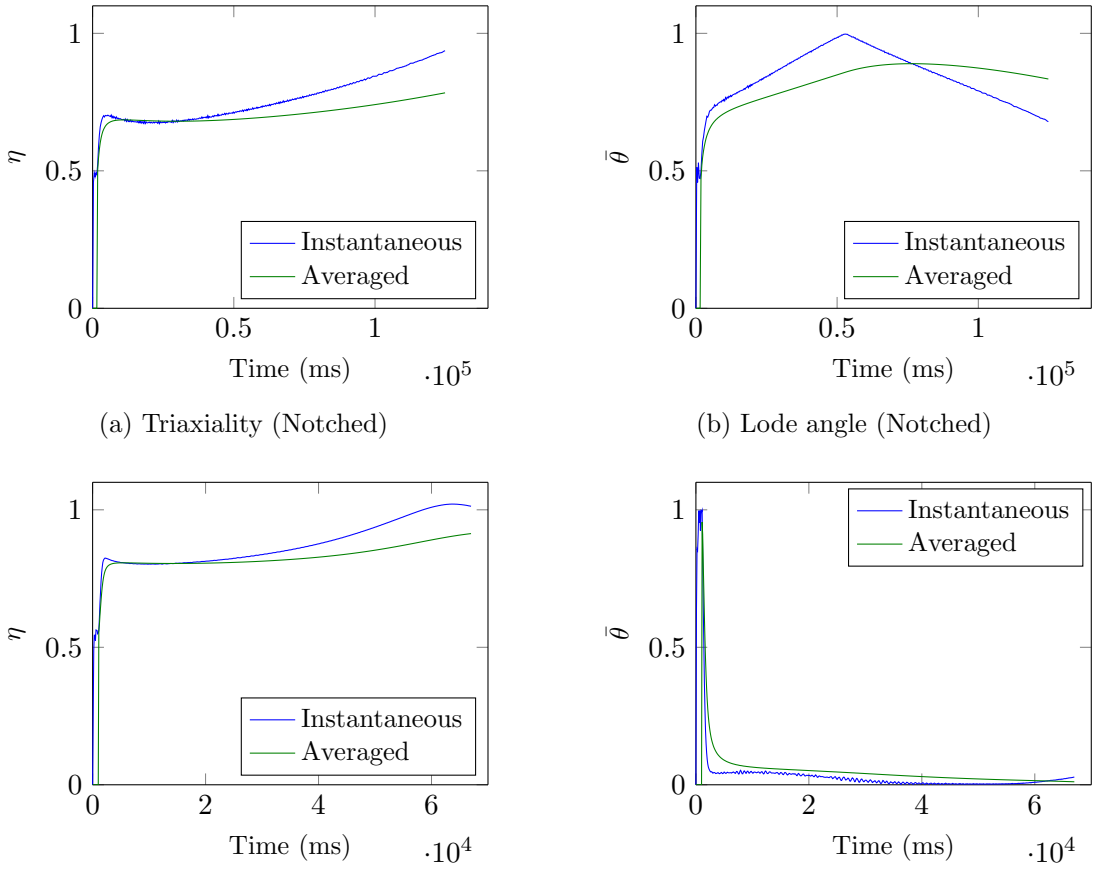

(a) Triaxiality (Notched)

(b) Lode angle (Notched)

(c) Triaxiality (Grooved)

(d) Lode angle (Grooved)

Figure 6.13: The triaxiality and normalised Lode angle evolutions for grooved and notched specimens, as taken from the 0.6 mm/min test simulations.

Notice that the triaxiality increases during the test due to the increase in hydrostatic tension caused by necking in the specimen, which explains why the observed averaged triaxialities are higher than the predicted values. The Lode angle history is more complex, and shows different trends for the notched and grooved specimens. For the notched specimens, the normalised Lode angle is initially less than 1, since the specimen is not axisymmetric, and increases as the specimen deforms. When the normalised Lode angle reaches 1 it begins to decrease at the same rate it was increasing since $-1 \leq \bar{\theta} \leq 1$. Conversely, the normalised Lode angle in the grooved specimen is at 1 initially and rapidly decreases, tending toward 0, while the averaged value decreases at a slightly slower rate. The decrease is less rapid as the groove radius increases, which is why the tests with larger groove radii show greater average normalised Lode angles at failure.

6.2.3 Strain Rate Range

In order to determine the effect of strain rate on the damage model, a measure of strain rate is needed such that a single strain rate value can be assigned to each set of tests. This is not trivial since the local strain rate at the point of failure changes as the specimen deforms, so the strain averaged value was taken in the same manner as was done with the triaxiality and Lode angle. However, even using the average strain rate at failure, the variation in strain rate between the different specimen geometries still results in a range of values for a single boundary velocity. Therefore an average was taken for all the tests at each boundary velocity, after which the model can be calibrated separately at each strain rate regime to examine the effect of the strain rate value on the model parameters. Figure 6.14 shows the average plastic strain rates for each test simulation, as well the initial plastic strain rate after yield, and the plastic strain rate at failure, represented by the error bars. Since the strain rate increases throughout the test as the strain field becomes more localised, the strain rates at yield and at failure represent the minimum and maximum strain rates respectively during the test.

Note that the notched specimens all deform at similar strain rates, while the strain rate in the grooved specimens noticeably decrease with an increasing groove radius. The average strain rates for each test speed are given in Table 6.5. Note that the 100 mm/min test slightly yields an underestimation of strain rate due to the lack of data for the grooved specimens. It is evident from the simulations that the deviation in strain rate from yielding to failure is large in comparison to the average, particularly for the 100 mm/min tests. This is because at the

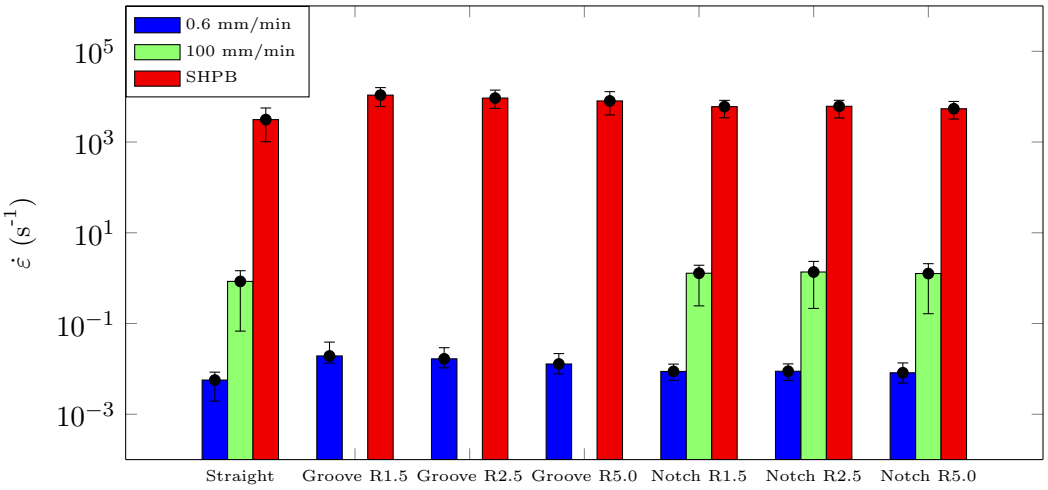

Figure 6.14: The strain rates taken from the numerical simulations of each test.

faster cross-head speed, the time taken for testing machine to reach top speed was a significant portion of the duration of the test. This means that the cross-head speed had not reached its maximum at the point of yield, resulting in a low initial strain rate. The large variation in strain rates, particularly in the grooved specimens, may be problematic as the average strain rate may not be representative of the strain rate at the time of the test when most of the void growth occurs, however this consideration is beyond the scope of this dissertation and was not investigated further.

	0.6 mm/min	100 mm/min	± 7 m/s
$\dot{\varepsilon}$ (s^{-1})	0.0115	1.190	6982.8

Table 6.5: The average strain rates at failure of all the tests for each strain rate regime.

6.2.4 Calibration

Using the plastic strains and average triaxialities and Lode angles at failure obtained from the full set of simulations, the damage model can be calibrated independently for each strain rate regime. Figure 6.15 shows the failure strains for each test.

From the bar graph, it is clear that the strain at failure decreases with an increase in strain rate, confirming the observation made in Chapter 5, and that the notched and grooved specimens fail at lower strains. The notches and grooves increase the triaxiality at the failure location, as described earlier in Equations 2.49 and 2.50. Additionally the grooved specimens fail at lower strains than the notched specimens, which is consistent with the original findings of Xue and Wierzbicki [7, 61] showing that the strain at failure was least along the line $\bar{\theta} = 0$. Since the

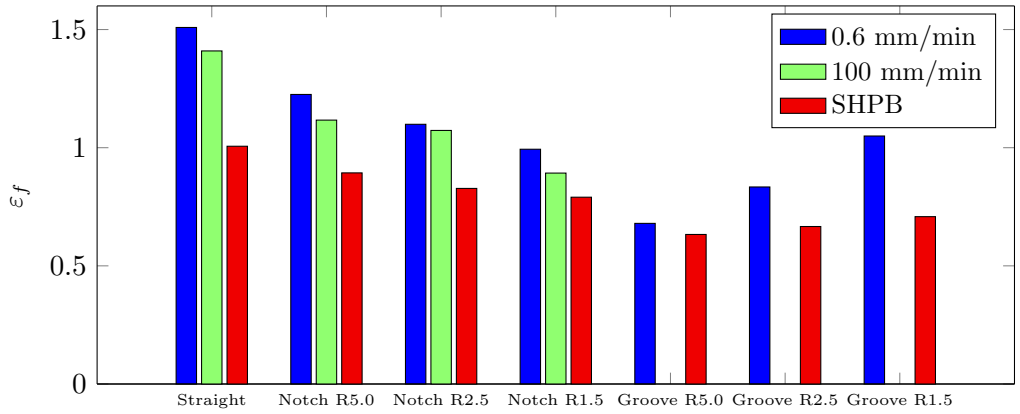

Figure 6.15: The plastic strain at failure for each test.

grooved specimen data is not available for the 100 mm/min tests, curves were fitted to the failure strain vs. triaxiality data for the notched and straight specimens as shown in Figure 6.16.

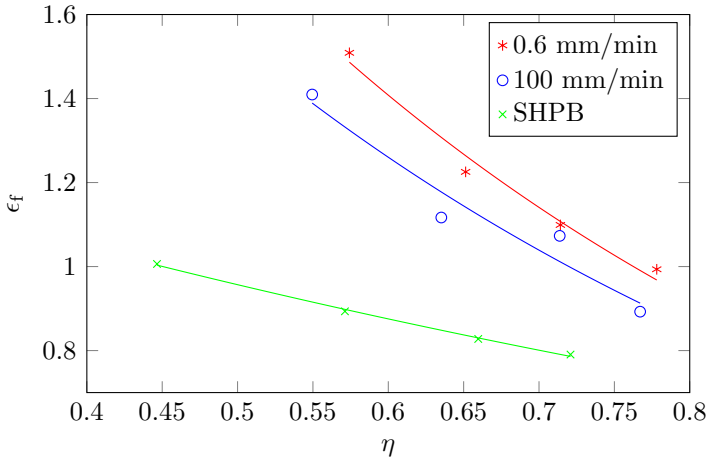

Figure 6.16: The plastic strain at failure vs. triaxiality for the different strain rate regimes for notched and straight specimens.

The curve fitted to the test data for each test speed was of the form:

$$\varepsilon_f = Ae^{-B\eta} \tag{6.6}$$

Figure 6.17 shows the values for the damage parameters plotted against the logarithmic strain rate, which was taken as an average of all the strain rates (notched and straight specimens) for each test speed.

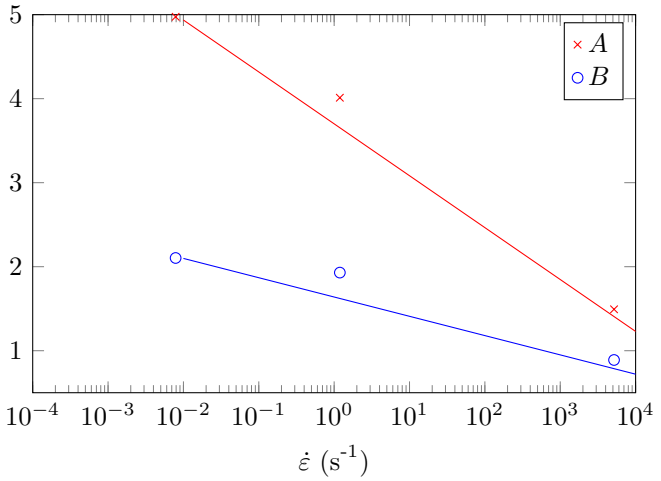

Figure 6.17: The effect of strain rate on the proposed strain rate factors.

Similarly to the strain rate function used in the Johnson-Cook damage model [5], the relationship between the strain rate and the damage parameters was initially approximated as a decreasing logarithmic function. However it was found that using a power law function of the form:

$$A(\dot{\varepsilon}) = D_1 - D_2 \cdot (\dot{\varepsilon})^{D_3} \tag{6.7}$$

$$B(\dot{\varepsilon}) = D_4 - D_5 \cdot (\dot{\varepsilon})^{D_6} \tag{6.8}$$

yielded a better fit to the data, such that the damage function is given as follows:

$$\varepsilon_f = A(\dot{\varepsilon}) \exp\left(-B(\dot{\varepsilon})\eta\right) \tag{6.9}$$

Using the correlated strain rate dependent model, each data point was compared to the correlated value, as shown in Figure 6.18. The contour lines in the figure represent the lines of constant strain rate for the damage function given in Equation 6.9, and the labels for each data point represent the individual average strain rates for each test.

The fit obtained by including strain rate effects in the damage function is good over the entire range of tests, yielding a maximum error of less than 7% for the test at 3121s^{-1}. As can be seen by the error bars, the majority of the correlated data points fit within the error due to the spread of the data and the ability of the user to select the point of failure. The minimum and maximum error values for the error were determined by sampling a number of points at which

failure may have occurred, and using the maximum and minimum values obtained as the limits for the error. This takes into account the effect of the spread of the data, as well as the human error incurred during the sampling process. Note that although the model fits well for the range of data presented in this dissertation, it is not consistent at very high strain rates ($\dot{\varepsilon} \approx 10^5 \mathrm{s}^{-1}$) as the constants A and B become less than zero for strain rates greater than:

$$\dot{\varepsilon}_{lim} = \left(\frac{D_1}{D_2}\right)^{1/D_3} \quad , or \quad \left(\frac{D_4}{D_5}\right)^{1/D_6} \tag{6.10}$$

Clearly the current model is not consistent with any physical interpretation, but since it yields a very good fit to the range of data presented, it is used for the purpose of this dissertation.

Having examined the effect of strain rate on damage for the notched and straight specimens, the damage surface should also be calibrated so as to include the data from the grooved specimens. The surface is calibrated for both the 0.6 mm/min and SHPB test independently, after

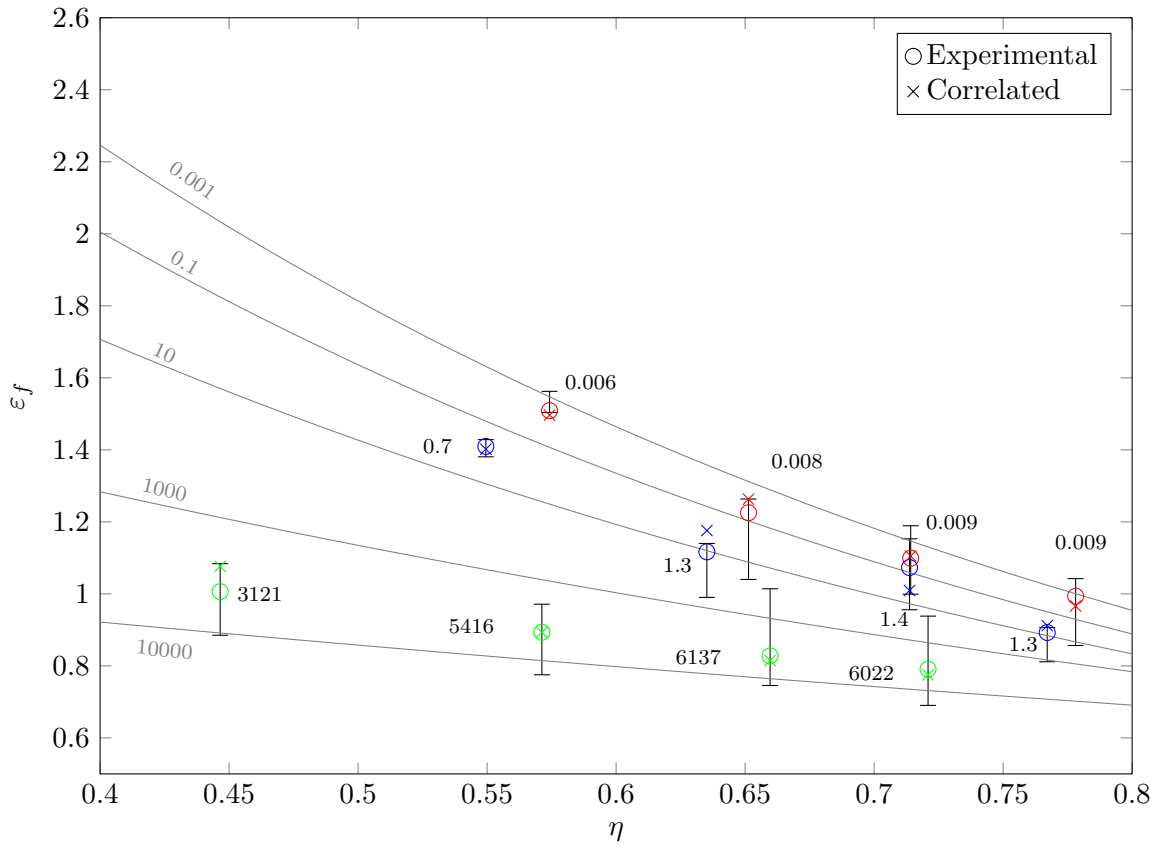

Figure 6.18: The plastic strain at failure vs. triaxiality using a strain rate dependent function. The labels represent strain rate in s^{-1}, and the error bars represent the variation resulting from manually selecting the point of failure, as well as the spread of the data. The correlated data points represent predictions made by the correlated model, whilst the experimental data points represent data obtained experimentally.

which the strain rate parameters previously determined are included such that a single function can describe the full range of tests and the resulting surfaces compared to the independently calibrated surfaces. Figure 6.19 shows the independently calibrated surfaces.

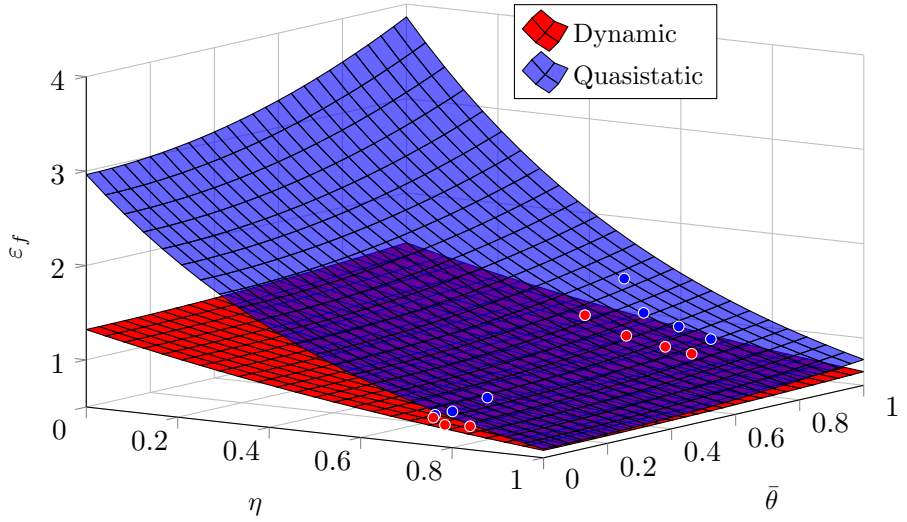

Figure 6.19: The failure surface calibrated for the dynamic and quasistatic tests.

As can be seen, the surface for the dynamic data is flatter than that for the quasistatic data, which is a similar trend to that seen in Figure 6.18. Using a similar process to that used for the notched and straight specimen data, a single function is correlated to the data describing the failure surface as a function of strain rate, such that the final form of the damage model is given as:

$$\left((D_1 - D_2 \cdot \dot{\varepsilon}^{D_3}) \exp\left(-(D_4 - D_5 \cdot \dot{\varepsilon}^{D_6})\eta\right)\right) \cdot \left(D_7 \bar{\theta}^2 + D_8\right) \tag{6.11}$$

However, because the failure surface is only calibrated for two strain rate regimes, a function of the form shown in Equations 6.7 and 6.8 cannot be fitted to the data as there are not enough data points. To accommodate for this, the values for the constants D_1 and D_4 from Equation 6.10 are taken from the previously correlated function shown in Figure 6.18, and scaled so as to account for the effect of the Lode angle (see Equation 4.41). The resulting level surfaces are shown in Figure 6.20.

Using the fully calibrated damage model, the correlated values are once again compared to the values observed experimentally for the full set of data including the 100 mm/min tests, as seen in Figure 6.21.

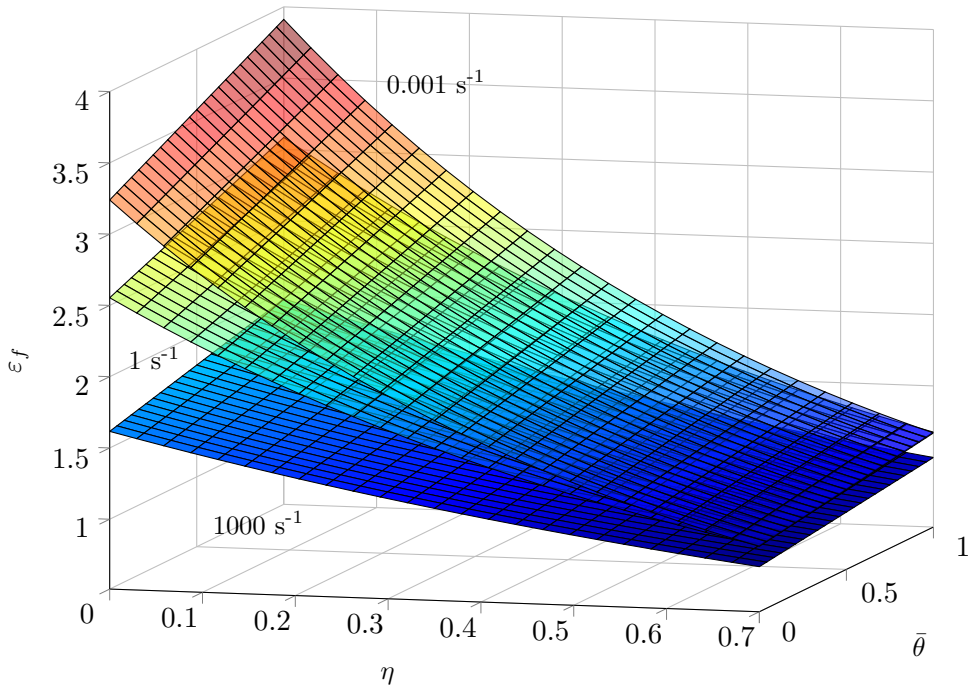

Figure 6.20: The level surfaces of the damage model for varying plastic strain rate.

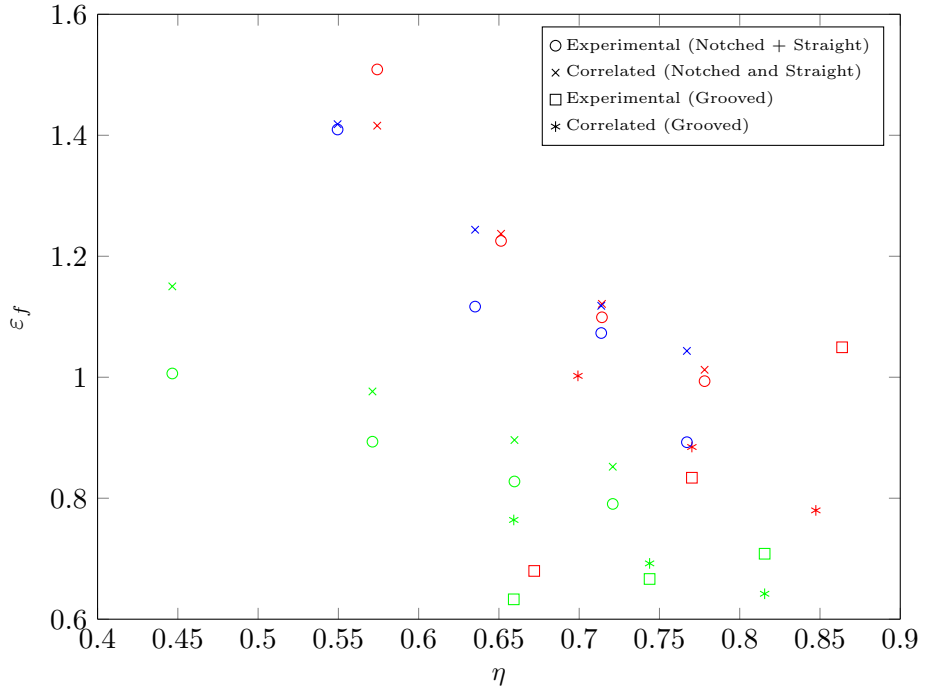

Figure 6.21: The correlated values compared to the experimental data using the fully calibrated model.

Note that model does not show as good a fit as seen in Figure 6.18, particularly for the 100 mm/min tests, which is to be expected since the data from that set of tests was not used to calibrate the model. However, like the fit seen in Figure 6.18, the model also overestimates the strain at failure for the dynamic data. This is a consequence of the use of the average strain rate in the model calibration, particularly for the straight specimen which has a significantly lower strain rate than the rest of the specimens. This causes the model to overestimate the strain at failure, as it is calibrated using a strain rate higher than the actual average strain rate for the straight specimen tests. Conversely, the model underestimates the strain at failure for the straight specimen for the 0.6 mm/min test. This is likely because the values for D_7 and D_8 were taken as an average of the values obtained for the two surfaces shown in Figure 6.19, causing an underestimation in strain at failure for the slower strain rates, and an overestimation thereof for the faster.

The correlated values match the experimental data quite closely for the grooved specimens, which further suggests that using the average strain rate to calibrate the model is the cause of the overestimation, since the grooved specimens deform at significantly higher strain rates than the other geometries. Encouragingly, the correlated values match the 0.6 mm/min test data closely over the all the test geometries, with the exception of the R5.0mm grooved specimen. The experimental data for the grooved specimens does not show an exponential relationship between triaxiality and failure strain as with the notched and straight specimens, but the model yields values in the same range as the experimental data points, and so this is not investigated further for the purpose of this dissertation. The final calibrated values for the model parameters are given in Table 6.6.

D_1	D_2	D_3	D_4	D_5	D_6	D_7	D_8
2.257	1.129	0.0452	3.391	2.013	0.0273	0.470	2.264

Table 6.6: The correlated parameters for the damage model with strain rate dependency.

Note that adding 4 extra constants to take strain rate into account is perhaps impractical, but for the focus of this dissertation, investigating the effect of strain rate on ductile damage, accuracy was preferred over practicality.

6.2.5 Verification

As a form of verification, the calibrated damage model was implemented in the finite element subroutine by deleting elements which satisfy the failure criterion. To keep the model as simple

as possible, the damage number was not expressed in the integral form:

$$D = \int_0^{\varepsilon_f} \frac{\mathrm{d}\varepsilon}{\varepsilon_f(\eta, \bar{\theta}, \dot{\varepsilon})} \quad \text{(Failure at } D = 1\text{)} \tag{6.12}$$

as is done in the literature (see [7, 8, 24]), but rather by simply comparing the effective plastic strain in the element to the function describing the failure strain, $\varepsilon_f(\eta, \bar{\theta}, \dot{\varepsilon})$. For the purpose of this dissertation this approach is acceptable as the loading conditions for each test are relatively constant throughout the duration of the test, but it should be noticed that for simulations with complex loading histories, the integral form of the damage is necessary, as damage is history dependent. The damage model was implemented for the 0.6 mm/min, 100 mm/min and SHPB tests with the straight specimen, and the rsults are shown in Figure 6.22.

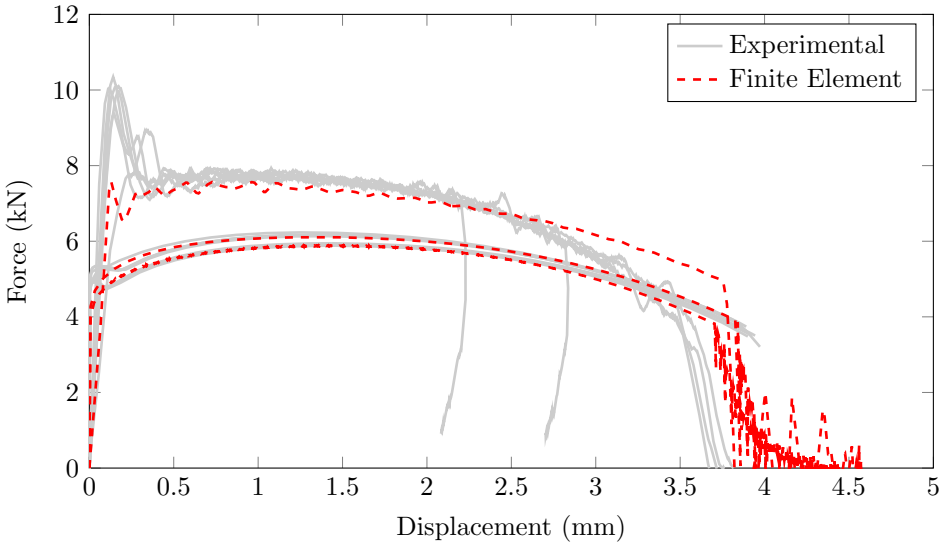

Figure 6.22: The force-displacement data of the straight specimen simulations with the damage model included compared to the experimental data.

As can be seen, the model overestimates the displacement at failure for the dynamic test, and shows an underestimation for the 0.6 mm/min test, while the 100 mm/min test is quite accurate. This is consistent with predictions shown in Figure 6.21, which is encouraging as it suggests the damage behaviour of the finite element model can be accurately predicted after the calibration of the damage model without actually implementing the model in the finite element routine, meaning further simulations to calibrate the damage model can be avoided.

Chapter 7

Discussion and Conclusions

The aim of this dissertation is to investigate the testing procedure required to calibrate an existing damage model over a range of strain rates, and determine the effectiveness of both the testing procedure and the model such that a relationship between strain rate and damage can be determined both qualitatively and quantitatively. In this chapter, the design and manufacture of the specimens required for testing, as well the test results thereof are assessed in terms of ease of use and effectiveness. Thereafter, the challenges and successes of the numerical modelling procedure are investigated regarding the finite element mesh and the user-implemented plasticity model.

The choice of damage model is then analysed, considering the ease of calibration and the accuracy of the damage model over the range of tests. Finally the effect of strain rate on the damage model is reviewed.

7.1 Specimen Design and Manufacture

The design of specimens for the purpose of calibrating a damage model poses three major problems, namely:

- The specimens must be small enough for use with a tensile SHPB apparatus.
- The loading range of the set of tests must be sufficient to fill the design space required to calibrate the damage model.

- The manufacturing process must be simple, accurate and repeatable.

The size of the specimens posed a challenge because the gauge length was limited to minimise ring-up in the SHPB apparatus, and the specimen width was limited by the clamping fixture designed for the tensile SHPB. Having such a short gauge length in comparison to the specimen thickness and width means that inferring a stress-strain relationship from the force-displacement data obtained during a test is difficult, as the strain field is not consistent throughout the gauge length, and necking occurs relatively early in the duration of the test. Additionally, designing the notched and grooved specimens is difficult because of the small geometries required, which poses challenges both in manufacturing and obtaining repeatable results. The radius of the grooved specimens was limited by the size of the cutter available, and the surface finish on the machined groove appears to have possibly had an effect on the repeatability of the results obtained.

Using a set of straight, notched and grooved specimens to fill the normalised Lode angle-triaxiality space was partially successful. The straight and notched specimens showed a relatively constant Lode angle with a large spread of triaxialities that were quite close to the predicted values, which is ideal for the damage model calibration as the specimens can be designed without performing numerical simulations prior to the manufacture and testing. However, the grooved specimens showed a tight grouping of triaxialities for the different groove radii which were significantly higher than the predicted values, and the Lode angle deviated from the $\bar{\theta} = 0$ line as the groove radius increased. Because of this, using a larger radius groove to obtain data at lower triaxialities would be problematic because the normalised Lode angle would begin to become large enough to create difficulty in observing any trends.

Lastly, the accuracy and repeatability obtained using the wire electrical discharge machining method was very encouraging. A previous attempt at specimen manufacture at BISRU [9], which involved conventional machining, found that the straight specimens failed away from the centre of the gauge section of the specimen, which was problematic in terms of predicting such behaviour in a simulation so that the local stress state parameters could be determined at the point of failure. However, there was no such problem in the set of tests performed for this dissertation, which suggests the manufacturing process and specimen mounting procedure was accurate and repeatable enough that there were no imperfection in the specimen gauge section significant enough to cause necking in an off-centre region of the specimen. Additionally, the force-displacement results for the straight and grooved specimens were consistent over the entire

range of strain rates tested, which confirms manufacturing accuracy, as well as consistency in the material properties of the DOMEX 355MC high strength steel tested.

7.2 Tensile SHPB Tests

The tensile SHPB apparatus used was largely successful, producing consistent and interpretable results. The only noticeable issue is that of the initial stress overshoot present during yielding. Anecdotal evidence suggests that it may an artefact of the apparatus and not a material property, although the material does exhibit an upper and lower yield point at quasistatic rates, and there may be some real material response which is accentuate by the apparatus.

The numerical models of the specimen with clamps and bars did not replicate the observed behaviour, which suggests that the issue is not a result of the impedance mismatch between the bars and clamps due to the different material properties. Although this artefact could not be mitigated, it is only present for a small portion of the force-displacement curve for the straight specimens, which yielded the most repeatable and interpretable data.

The data gathered for the grooved specimens was not as interpretable, due to the prevalent transient behaviour present in the recorded signals. The striker velocities were similar over the entire range of tests, meaning the local strain rate was higher in the notched and grooved specimens than the straight specimens, and consequently the notched and grooved specimens fractured significantly earlier. This caused the stress overshoot and resulting oscillations in the signal to take up a far more significant portion of the force-displacement curve, particularly for the grooved specimens. Although these specimens are not used in the calibration of the plasticity model, it is still important that the point of fracture can be accurately located for the calibration of the damage model, which is why the oscillations present in the data are problematic if they have not died away before failure. Aside from the stress overshoot, the data obtained from the SHPB tests suggests that the "Fir-tree" specimen design is successful.

7.3 Numerical Modelling

The models developed for this dissertation addressed three major challenges: efficient modelling of the tensile SHPB apparatus in order to appropriately simulate the boundary conditions experienced by the specimen, simulating quasistatic tests using an explicit finite element scheme,

and finally calibrating and implementing an accurate plasticity model over the entire range of tests.

Modelling the SHPB apparatus was an excellent solution to the problem of correctly replicating the boundary conditions experienced by the specimen, and using the non-reflecting boundary conditions with modified elements at the bar ends allowed for manageable simulation run times. By investigating the implementation of the non-reflecting boundary condition in LS-DYNA, an elegant solution was found using an extra row of radially constrained elements which successfully prevented any spurious reflections. Furthermore, the numerical models yielded results showing very similar behaviour to the experimental data, aside from the stress overshoot seen experimentally which could not be replicated numerically.

Using an explicit scheme to simulate the quasistatic tests is a relatively a simple process. The mass scaling technique used was easily implemented, and yielded results showing negligible kinetic energy in comparison to the internal energy generated during deformation. This suggests that the inertial forces experienced by the specimen are negligible in comparison with the internal forces, meaning the results obtained are accurate. It should be noted that the simulations reached a point of instability when the mass was increased too much, although the kinetic energy was still negligible and the time step was below the critical value. However, providing the level of mass scaling was set below this limit, the simulations were stable while running for reasonable time periods ($\approx$ 2-3 hours), and so the phenomenon was not investigated further.

Implementing the user-defined material model is LS-DYNA was a difficult process, but allowed for a level of control that could not be achieved using built-in functions available with the commercial software. Defining the material model provides the following advantages:

- The plasticity model can be customised.
- The damage model can be implemented in the finite element simulations.
- The parameters for the damage model calibration can be output as history variables.
- The model can be coupled to LS-DYNA's thermal solver, such that the temperature in each element can be calculated accounting for conduction.
- The user has direct control over the definition of the plastic strain rate.

Although the damage model calibration would be possible without implementing a user-defined material model, it would not be possible to implement the element failure criterion in the finite element model, meaning that the damage model could not be verified using the simulations. Additionally, using the thermal solver to calculate temperature is a method which is not widely used, as temperature is usually treated as an internal variable for each element, and allows for a method which is applicable over any range of strain rates. The results of the numerical simulations showed good correlation for the force-displacement curves over the entire range of tests. Using a combination of optimisation routines and estimations regarding the stress at yield for the different strain rates, the plasticity model was successfully calibrated. The dynamic test simulations showed different behaviour to the experimental data during the latter portions of deformation, which should be investigated further. Initial observations suggest that a mechanism, perhaps the rate at which damage occurs, is responsible for the deformation behaviour during the latter stages of deformation which is not captured in the plasticity model.

7.4 The Damage Model

Correctly calibrating the Bai-Wierzbicki damage model over the range of strain rates tested is the crux of this dissertation, as it provides a quantitative measure of the effect of strain rate on ductile damage. However, the calibration of the model for a single strain rate is not a trivial task, and determining a mathematical relationship between the model parameters and strain rate poses even more difficulties. The challenges encountered during the calibration of the damage model for this dissertation are:

- Determining the point of failure in a numerical simulation. This was problematic as a small variation in the choice of displacement at failure resulted in relatively large changes in the local strain at failure. This meant that variations in the displacement at failure due to the spread of the data had a significant effect on the local strain at failure. However, these variations were generally small enough to fall within the variation between specimens exhibited by the material (see Figure 6.18). Additionally, determining which point on the force-displacement curve corresponds to failure was difficult for the SHPB data, as the force does not exhibit a sharp a drop as in the quasistatic data.
- Ensuring sufficient mesh refinement to ensure accuracy of the local element variables at the physical point of fracture. Because the deformation is highly localised at the centre of

the specimen at the time of fracture, the refinement of the mesh in the region of fracture has a significant effect on the effective plastic strain in the element at which fracture first occurs. Although mesh may be refined sufficiently that the force-displacement curve has showed convergence, the strain field is so localised that the refinement at the centre of the specimen may still be inadequate. Adaptive mesh refinement may be required to ensure the strain field is sufficiently captured as the plastic strain increases.

- Determining the dependence of the loading history on damage. It is not clear over what portion of the specimen deformation the physical mechanisms of damage, such as void growth, actually occur. Bao and Wierzbicki [24] proposed using the strain averaged parameters as the values used in the damage model, but there is no physical evidence to support this theory. It seems intuitive that the influence of the damage parameters should increase as the element nears the point of failure, which does occur using the strain averaged parameters as the strain rate increases prior to failure. However, further investigation into the nature of the dependence on the different damage parameters is required.

- Choosing a suitable technique to fit the failure surface to the data. In order to fit a symmetric surface with an exponential dependence on triaxiality and a quadratic dependence on the normalised Lode angle, Bai and Wierzbicki [8] suggested using a combination of two curves along lines of constant Lode angle as given in Equation 2.38. This is slightly different to the form of the failure surface used for this dissertation (see Equation 4.41), which is described using two multiplicatively separable functions of triaxiality and normalised Lode angle. Although the two functions are similar, they do not yield precisely the same results, and because the data for the grooved specimens does not show distinct trends, the results obtained using the former function are predict very high failure strains. Figure 7.1 compares the resulting failure surfaces using the two different surface functions. For this reason, the latter function was used.

Overall the model was successfully calibrated, as illustrated by the verification simulations, and gave quantifiable results to investigate the effect of strain rate on ductile damage. The results clearly showed that the plastic strain at failure is dependent on the Lode angle as well as the triaxiality, although the specimens which failed under $\bar{\theta} \approx 0$ did not show the expected trend of a decrease in failure strain with increasing triaxiality, and actually seemed to exhibit the opposite behaviour. This clearly illustrates the need for a model which accounts for the nature

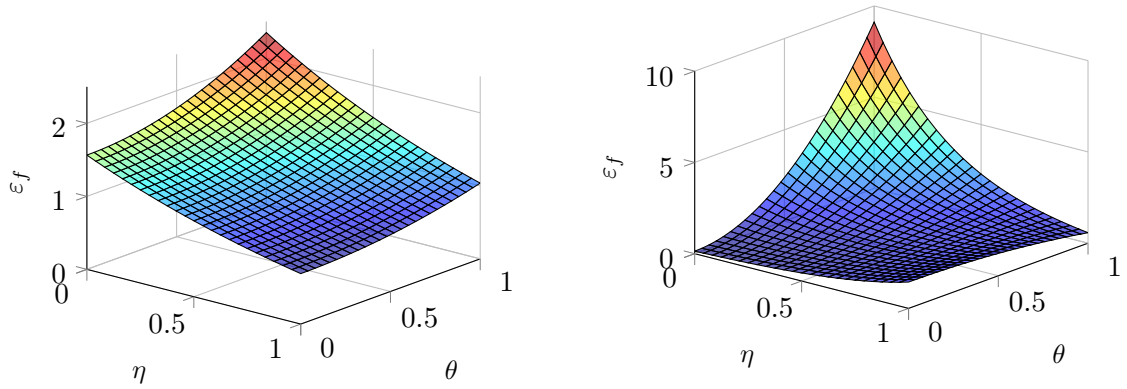

(a) $\varepsilon_f = [D_1 \exp(D_2\eta)] \cdot [D_3\bar{\theta}^2 + D_4]$

(b) $\varepsilon_f = \left[\frac{1}{2}\varepsilon_f^{(+)} - \varepsilon_f^{(\circ)}\right]\bar{\theta}^2 + \varepsilon_f^{(+)}\bar{\theta} + \varepsilon_f^{(\circ)}$

Figure 7.1: A comparison of the two possible functions used to calibrate the failure surface (function (a) was used for this dissertation).

of the loading condition as well as the level of hydrostatic tension. Table 7.1 summarises the advantages and disadvantages of the Bai-Wierzbicki model and the calibration process used.

Advantages
Accurate over a wide range of loading conditions.
Easily implemented in a finite element code.
Uses macroscopic material parameters.
Calibration procedure (excluding strain rate effects) is well defined and accessible.

Disadvantages
Requires a large number of different tests to calibrate.
Very sensitive to mesh refinement and location of point of failure.
Needs 8 parameters to include strain rate effects, and 10 to include asymmetry.

Table 7.1: The advantages and disadvantages of the Bai-Wierzbicki damage model.

7.5 Strain Rate and Ductile Damage

As mentioned previously, the primary aim of this dissertation is to investigate the effect of strain rate on a chosen damage model. A significant finding is that the calibration of the damage model at three different strain rates showed a distinct trend of a decrease in failure strain with increasing strain rate.

This is contrary to the trends reported in the literature (see Section 2.2.3), which suggest that an increase in strain rate results in an increase in ductility. Considering only the notched and grooved specimens, a clear trend was observed showing a decrease in failure strain at the faster test speeds. The exact nature of the strain rate dependency is not known, but a power-law

function is used to quantify the effect of strain rate on the damage function, which yields a close correlation for the range of data tested. A similar process was performed using the full damage surface, which yielded encouraging results, although the failure behaviour could not be captured for the grooved specimens. However, the experimental data fitted the correlated failure strain function within an acceptable tolerance, and verification simulations suggest that the calibration and implementation of the Bai-Wierzbicki damage model with added strain rate dependency is successful.

Chapter 8

Recommendations

Although the aims of this research were met and definite trends regarding the effect of strain rate on ductile damage for the chosen material were identified and characterised, there are several aspects upon which the procedure followed can be improved. This chapter outlines recommendations to be considered for future research following a similar procedure, both in terms of the experimental and numerical methods employed, as well as the possible uses for the results obtained.

8.1 Experimental Method

The specimens used in the test procedure were largely successful despite their small sizes, producing repeatable and useful results. However, the data obtained from the grooved specimens shows some inconsistencies, which may possibly be due to the surface finish obtained during the machining of the larger radii grooved specimens. More effort should be made to ensure a fine surface finish on the surface of the groove. Additionally, the triaxialities at failure obtained from the grooved specimen data is closely grouped, which does not lend itself to identifying trends in the dependence of failure strain on triaxiality for the grooved specimens. Using a larger radius groove is not a perfect solution, as the Lode angle deviates away from the line $\bar{\theta} = 0$, so a preferable solution would be to design a shear specimen compatible with the tensile SHPB apparatus at BISRU.

The quasistatic test procedure requires the use of an extensometer for accurate results that can be compared to the SHPB data, but the results obtained using the extensometer were too

inconsistent. Machining grooves into the adaptors such that displacement between the clamps would be tracked was a feasible idea, but more consideration is needed regarding seating the blades properly in the grooves. Another issue with the quasistatic tests was the time taken for the Zwick to reach full speed for the 100mm/min tests. This can be resolved by testing at a slightly slower speed (75mm/min), and testing at slower speeds still for the notched and grooved specimens, such that the local strain rates are constant, but the acceleration period and the sampling frequency are no longer issues.

Regarding the dynamic test procedure, the stress overshoot in the SHPB tests must be addressed. An investigation must be conducted into the cause of the stress overshoot, and a solution found to mitigate its effect. For testing with the artefact present, the striker velocity should be tuned for each test such that the specimen fails near the end of the stress pulse, which reduces the impact of the resulting oscillations from the overshoot on the processed force-displacement data.

8.2 Numerical Modelling

In order to gain more confidence in the calibrated failure surfaces, the numerical modelling procedure must be improved in a few key areas. One of the issues with the greatest effect on the data obtained is the mesh refinement. For the purpose of this dissertation, mesh refinement studies were not conducted on the specimen models, which can have a profound effect on the effective plastic strain measured, as illustrated in Figure 8.1, which compares the plastic strains in the element at the centre of the specimen for a 0.1mm and a 0.05mm mesh.

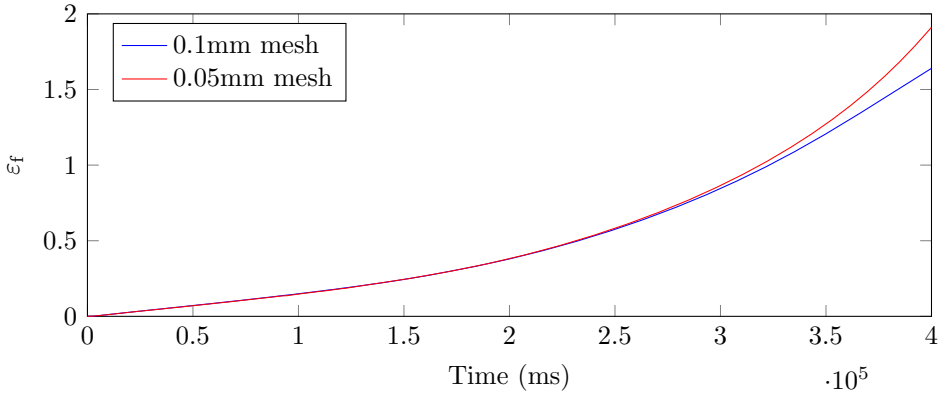

Figure 8.1: The effect of mesh refinement on the local plastic strain.

A mesh convergence study should be completed for each specimen geometry prior to the material model calibration to ensure accurate measurements of the required parameters at the failure location. Using adaptive mesh refinement should also be investigated.

Additionally, the plasticity model did not exhibit a perfect fit to the experimental data for the full range of tests, particularly for the grooved specimens. As mentioned in Section 6.2.1, the effect of using a triaxiality and Lode angle dependent plasticity model should be investigated. High speed camera footage could be used to verify the time of and displacement at fracture in the SHPB tests, and, coupled with digital image correlation software, to verify the strain field in the specimen.

Additionally, the effect of temperature should be further investigated, particularly using the temperature calculated using a thermal solver accounting for heat conduction, which may help eliminate the over prediction in force at failure for the dynamic specimens. Another option to consider, is the effect of damage on the material strength, as implemented by Xue and Wierzbicki [61], which allows for a deterioration in material strength as damage accumulates.

Most importantly, to improve the data obtained and analysis performed in this dissertation, data must be obtained at more strain rates in order to determine the effect of strain rate more rigorously, as the observations made in this dissertation regarding the strain rate effect on ductile damage require additional data points to verify the results. In order to gain a more complete understanding of the effect of strain rate on ductile damage, the fracture characteristics of a material must be determined for a greater variety of strain rates.

The results observed in this dissertation are significant in terms of the use of strain rate dependent material models in impact and blast simulations, particularly using high strength steels such as DOMEX. Many problems involving the design and analysis of protective structures involve the simulation of high strain rate events, such as during a landmine blast or car crash. The effect of strain rate on ductility can have a major impact on the design of such structures, especially considering existing commonly used material models would over predict the performance of the structures by increasing the ductility at higher strain rates. The use of a damage model which correctly models the change ductility as a function of strain rate is important for these types of designs and analyses, and research therein should be of high priority for the manufactures currently making use of damage models for high strength steels.

References

[1] C. Tipper, "The fracture of metals," *Metallurgia*, vol. 39, no. 231, pp. 133–137, 1949.

[2] F. McClintock, "A ctriterion for ductile fracture by the growth of holes," *Journal of Applied Mechanics*, vol. 35, pp. 363–371, 1968.

[3] J. Rice and D. Tracey, "On the ductile enlargement of voids in triaxial stress fields," *Journal of Mechanics of Physics and Solids*, vol. 17, pp. 201–217, 1969.

[4] A. L. Gurson, "Continuum theory of ductile rupture by void nucleation and growth: Part i—yield criteria and flow rules for porous ductile media," *Journal of Engineering Materials and Technology*, vol. 99, pp. 2–15, 1977.

[5] G. R. Johnson and W. H. Cook, "Fracture characteristics of three metals subjected to various strains, strain rates, temperatures and pressures," *Engineering Fracture Mechanics*, vol. 21, no. 1, pp. 31 – 48, 1985.

[6] Y. Bao and T. Wierzbicki, "A comparative study on various ductile crack formation criteria," *ASME. J. Eng. Mater. Technol.*, vol. 126, no. 3, pp. 314 – 324, 2004.

[7] T. Wierzbicki, Y. Bao, Y.-W. Lee, and Y. Bai, "Calibration and evaluation of seven fracture models," *International Journal of Mechanical Sciences*, vol. 47, no. 4–5, pp. 719 – 743, 2005.

[8] Y. Bai and T. Wierzbicki, "A new model of metal plasticity and fracture with pressure and lode dependence," *International Journal of Plasticity*, vol. 24, no. 6, pp. 1071 – 1096, 2008.

[9] A. Bowden, "Experimental and numerical study on the effect of strain rate to ductile damage," Master's thesis, University of Cape Town, 2009.

[10] J. Lubliner, *Plasticity Theory*. New York: Macmillan, 1990.

[11] G. R. Johnson and W. H. Cook, "A constitutive model and data for metals subjected to large strains, high strain rates and high temperatures," in *Proceedings of the 7th International Symposium on Ballistics*, vol. 21, pp. 541–547, The Hague, The Netherlands, 1983.

[12] F. J. Zerilli and R. W. Armstrong, "Dislocation-mechanics-based constitutive relations for material dynamics calculations," *Journal of Applied Physics*, vol. 61, no. 5, pp. 1816–1825, 1987.

[13] H. Zhao, "A constitutive model for metals over a large range of strain rates identification for mild-steel and aluminium sheets," *Materials Science and Engineering: A*, vol. 230, no. 1, pp. 95–99, 1997.

[14] G. Cowper and P. Symonds, "Strain-hardening and strain-rate effects in the impact loading of cantilever beams," Tech. Rep. 28, Brown University Dept. of Appl. Math., 1957.

[15] G. Barenblatt, "The mathematical theory of equilibrium cracks in brittle fracture," *Advanced Applied Mechanics*, vol. 7, pp. 55–129, 1962.

[16] Y. Bai and T. Wierzbicki, "A comparative study of three groups of ductile fracture loci in the 3d space," *Engineering Fracture Mechanics*, vol. 135, pp. 147 – 167, 2015.

[17] V. Tvergaard, "Influence of voids on shear band instabilities under plane strain conditions," *International Journal of Fracture*, vol. 17, no. 4, pp. 389–407, 1981.

[18] A. Needleman and V. Tvergaard, "An analysis of ductile rupture in notched bars," *Journal of the Mechanics and Physics of Solids*, vol. 32, no. 6, pp. 461 – 490, 1984.

[19] V. Tvergaard and A. Needleman, "Analysis of the cup-cone fracture in a round tensile bar," *Acta Metallurgica*, vol. 32, no. 1, pp. 157 – 169, 1984.

[20] Y. Bai and T. Wierzbicki, "Application of extended mohr–coulomb criterion to ductile fracture," *International Journal of Fracture*, vol. 161, no. 1, pp. 1–20, 2010.

[21] M. Wilkins, R. Streit, and J. Reaugh, "Cumulative-strain-damage model of ductile fracture: simulation and prediction of engineering fracture tests," tech. rep., Lawrence Livermore Laboratory, Livermore, California, 1980.

[22] Y. Bao and T. Wierzbicki, "On fracture locus in the equivalent strain and stress triaxiality space," *International Journal of Mechanical Sciences*, vol. 46, no. 1, pp. 81 – 98, 2004.

[23] P. W. Bridgman, *Studies in Large Plastic Flow and Fracture*. Harvard University Press, 1964.

[24] Y. Bao and T. Wierzbicki, "On the cut-off value of negative triaxiality for fracture," *Engineering Fracture Mechanics*, vol. 72, no. 7, pp. 1049 – 1069, 2005.

[25] A. H. Clausen, T. Børvik, O. S. Hopperstad, and A. Benallal, "Flow and fracture characteristics of aluminium alloy aa5083-h116 as function of strain rate, temperature and triaxiality," *Materials Science and Engineering: A*, vol. 364, pp. 260 – 272, 2004.

[26] B. Erice, F. Gálvez, D. Cendón, and V. Sánchez-Gálvez, "Flow and fracture behaviour of {FV535} steel at different triaxialities, strain rates and temperatures," *Engineering Fracture Mechanics*, vol. 79, pp. 1 – 17, 2012.

[27] A. S. Khan and H. Liu, "Strain rate and temperature dependent fracture criteria for isotropic and anisotropic metals," *International Journal of Plasticity*, vol. 37, pp. 1 – 15, 2012.

[28] C. C. Roth and D. Mohr, "Effect of strain rate on ductile fracture initiation in advanced high strength steel sheets: Experiments and modeling," *International Journal of Plasticity*, vol. 56, pp. 19 – 44, 2014.

[29] B. Hopkinson, "A method of measuring the pressure produced in the detonation of high explosives or by the impact of bullets," *Philosophical Transactions of the Royal Society of London. Series A, Containing Papers of a Mathematical or Physical Character*, vol. 213, pp. 437–456, 1914.

[30] R. M. Davies, "A critical study of the hopkinson pressure bar," *Philosophical Transactions of the Royal Society of London A: Mathematical, Physical and Engineering Sciences*, vol. 240, no. 821, pp. 375–457, 1948.

[31] H. Kolsky, "An investigation of the mechanical properties of materials at very high rates of loading," *Proceedings of the Physical Society. Section B*, vol. 62, no. 11, p. 676, 1949.

[32] Y. Bai, X. Teng, and T. Wierzbicki, "Study on the effect of the third stress invariant on ductile fracture," Tech. Rep. 151, Impact and Crashworthiness Laboratory, Massachusetts Institute of Technology, Cambridge, MA., 2006.

[33] D. Mohr and S. Henn, "Calibration of stress-triaxiality dependent crack formation criteria: A new hybrid experimental–numerical method," *Experimental Mechanics*, vol. 47, no. 6, pp. 805–820, 2007.

[34] D. Mohr and M. Oswald, "A new experimental technique for the multi-axial testing of advanced high strength steel sheets," *Experimental Mechanics*, vol. 48, no. 1, pp. 65–77, 2008.

[35] M. Dunand and D. Mohr, "Optimized butterfly specimen for the fracture testing of sheet materials under combined normal and shear loading," *Engineering Fracture Mechanics*, vol. 78, no. 17, pp. 2919 – 2934, 2011.

[36] J. Harding, E. Wood, and J. Campbell, "A direct-tension split hopkinson bar for simultaneous torsion and compression.," *Journal of Mechanical Engineering Science*, vol. 2, pp. 88–96, 1960.

[37] S. Ellwood, L. J. Griffiths, and D. J. Parry, "A tensile technique for materials testing at high strain rates," *J. Phys. E: Sci. Instrum.*, vol. 15, pp. 1169–1172, 1982.

[38] R. A. Govender, T. J. Cloete, and G. N. Nurick, "A numerical investigation of dispersion in hopkinson pressure bar experiments," *Journal de Physique IV France*, vol. 134, pp. 521–526, 2006.

[39] G. Haugou, E. Markiewicz, and J. Fabis, "On the use of the non direct tensile loading on a classical split hopkinson bar apparatus dedicated to sheet metal specimen characterisation," *International Journal of Impact Engineering*, vol. 32, pp. 778–798, 2006.

[40] U. Lindholm and L. Yeakley, "High strain-rate testing: tension and compression," *Exp. Mech.*, vol. 8, no. 1, pp. 1–9, 1968.

[41] D. Mohr and G. Gary, "M-shaped specimen for the high-strain rate tensile testing using a split hopkinson pressure bar apparatus," *Exp. Mech.*, vol. 47, no. 5, pp. 687–692, 2007.

[42] M. Dunand, G. Gary, and D. Mohr, "Load-inversion device for the high strain rate tensile testing of sheet materials with hopkinson pressure bars," *Exp. Mech*, vol. 53, pp. 1177–1188, 2013.

[43] H. Eskandari and J. Nemes, "Dynamic testing of composite laminates with a tensile split hopkinson bars," *Journal of Composite Materials*, vol. 34, no. 4, pp. 260–273, 2000.

[44] T. G. del Río, E. Barbero, R. Zaera, and C. Navarro, "Dynamic tensile behaviour at low temperature of cfrp using a split hopkinson pressure bar," *Composite Science and Technology*, vol. 65, pp. 61–71, 2005.

[45] M. LeBlanc and D. Lassila, "Dynamic tensile testing of sheet materialsal using the split-hopkinson bar technique," *Experimental Techniques*, vol. 17, no. 1, pp. 37–42, 1993.

[46] C. Koh, V. Shim, V. Tan, and B. Tan, "Response of a high-strength flexible laminate to dynamic tension," *International Journal of Impact Engineering*, vol. 35, pp. 559–568, 2008.

[47] C. Wang and Y. Xia, "Validity of one-dimensional experimental principle for flat specimen in bar±bar tensile impact apparatus," *International Journal of Solids and Structures*, vol. 37, pp. 3305–3322, 2000.

[48] J. Peirs, P. Verleysen, W. V. Paepegem, and J. Degrieck, "Determining the stressestrain behaviour at large strains from high strain rate tensile and shear experiments," *International Journal of Impact Engineering*, vol. 38, pp. 406–415, 2011.

[49] M. Downey, "Design, build and test a tensile split hopkinson bar." Honours thesis, University of Cape Town, 2007.

[50] M. Spotts, *Mechanical Design Analysis*. Prentic-Hall, Inc., 1964.

[51] J. O. Halllquist, *LS-DYNA Theory Manual*. LSTC, March 2006.

[52] J. C. Ortiz, M; Simo, "Analysis of a new class of integration algorithms for elastoplastic constitutive equations," *Int J Num Meth Engng*, vol. 23, no. 5, p. 353–366, 1986.

[53] P. Fotiu and S. Nemat-Nasser, "A universal integration algorithm for rate-dependent elastoplasticity," *Computers & Structures*, vol. 59, no. 6, pp. 1173 – 1184, 1996.

[54] R. Kapoor and S. Nemat-Nasser, "Determination of temperature rise during high strain rate deformation," *Mechanics of Materials*, vol. 27, no. 1, pp. 1 – 12, 1998.

[55] R. D. Cook, D. S. Malkus, and M. E. Plesha, *Concepts and Applictions of Finite Element Analysis*. John Wiley & Sons, 1974.

[56] P. Verleysen, B. Verhegghe, J. Degrieck, and B. De Cooman, "Numerical study of the influence of the specimen geometry on split hopkinson tensile test results," in *WIT TRANSACTIONS ON ENGINEERING SCIENCES* (M. Alves and N. Jones, eds.), pp. 549–562, WIT Press, 2005.

[57] J. Lysmer and R. L. Kuhlemeyer, "Finite dynamic model for infinite media," *Journal of the Engineering Mechanics Division*, vol. 95, no. 4, pp. 859–878, 1969.

[58] D. Givoli, "High-order local non-reflecting boundary conditions: a review," *Wave Motion*, vol. 39, no. 4, pp. 319–326, 2004.

[59] B. Karp, A. Dorogoy, and Z. Wang, "Non-uniform impact excitation of a cylindrical bar," *Journal of Sound and Vibration*, vol. 323, pp. 757–771, 2009.

[60] A. Considére, "Memoire sur lemploi du fer et de lacier dans les constructions: ii," *Annales des Ponts et Chausses*, vol. 9, no. 6, p. 574–605, 1885.

[61] L. Xue and T. Wierzbicki, "Ductile fracture initiation and propagation modeling using damage plasticity theory," *Engineering Fracture Mechanics*, vol. 75, no. 11, pp. 3276 – 3293, 2008. Local Approach to Fracture (1986–2006): Selected papers from the 9th European Mechanics of Materials Conference.

Appendix A

LS-DYNA Element Subroutine

```
      subroutine umat44 (cm,eps,sig,epsp,hsv,dt1,capa,etype,tt,
     1 temp,failel,crv,cma,qmat,elsiz,idele)
!
! ************************************************************
! |  Livermore Software Technology Corporation  (LSTC)        |
! |  ---------------------------------------------------------  |
! |  Copyright 1987-2008 Livermore Software Tech. Corp        |
! |  All rights reserved                                      |
! ************************************************************
!
! Copyright (C) 2015 MATTHEW WEYER
!
! This program is free software: you can redistribute it and/or modify
! it under the terms of the GNU General Public License as published by
! the Free Software Foundation, either version 3 of the License, or
! (at your option) any later version.
!
! This program is distributed in the hope that it will be useful,
! but WITHOUT ANY WARRANTY; without even the implied warranty of
! MERCHANTABILITY or FITNESS FOR A PARTICULAR PURPOSE.  See the
! GNU General Public License for more details.
!
! You should have received a copy of the GNU General Public License
! along with this program.  If not, see <http://www.gnu.org/licenses/>.
!
! Redistribution and use in source and binary forms, with or without
! modification, are permitted provided that the redistributions of
! source code must retain the above copyright notice, this condition
! and the following disclaimer.
!
! E-Mail: wrymat001@myuct.ac.za
! Last Modified: 19/06/2015
```

```
!
!*************************************************************************
!*                                                                       *
!*****************          DISCLAIMER          ************************
!*                                                                       *
!*************************************************************************
!*                                                                       *
!* THIS SOFTWARE IS PROVIDED BY THE COPYRIGHT HOLDERS AND CONTRIBUTORS *
!* "AS IS" AND ANY EXPRESS OR IMPLIED WARRANTIES, INCLUDING, BUT NOT   *
!* LIMITED TO, THE IMPLIED WARRANTIES OF MERCHANTABILITY AND FITNESS   *
!* FOR A PARTICULAR PURPOSE ARE DISCLAIMED. IN NO EVENT SHALL THE      *
!* COPYRIGHT OWNER OR CONTRIBUTORS BE LIABLE FOR ANY DIRECT, INDIRECT, *
!* INCIDENTAL, SPECIAL, EXEMPLARY, OR CONSEQUENTIAL DAMAGES            *
!* (INCLUDING, BUT NOT LIMITED TO, PROCUREMENT OF SUBSTITUTE GOODS OR  *
!* SERVICES; LOSS OF USE, DATA, OR PROFITS; OR BUSINESS INTERRUPTION)  *
!* HOWEVER CAUSED AND ON ANY THEORY OF LIABILITY, WHETHER IN CONTRACT, *
!* STRICT LIABILITY, OR TORT (INCLUDING NEGLIGENCE OR OTHERWISE)       *
!* ARISING IN ANY WAY OUT OF THE USE OF THIS SOFTWARE, EVEN IF ADVISED *
!* OF THE POSSIBILITY OF SUCH DAMAGE.                                  *
!*                                                                       *
!*************************************************************************
!
!***********************************************************************
! Damage Model using a von Mises Yield function and a custom hardening
!         law. Damage parameters are taken from Bai & Wierzbicki model.
! Hardening parameters are plastic strain, plastic strain rate
!         and temperature.
! Damage parameters are average triaxiality, average Lode angle, and
!         plastic strain rate.
!***********************************************************************
!
!    Written BY  : Matthew Weyer, M.Sc.
!    Date: June, 2015
!
!   Characteristics:
!           1. For solid elements only
!           2. Formulation based on Incremental Deformation Theory
!           3. Stress integration based on Radial Return Algorithm
!           5. Rate-Dependent Formulation
!
!***********************************************************************
!
! variables
!
!     eps(1)  = local x  strain (Incremental)
!     eps(2)  = local y  strain
!     eps(3)  = local z  strain
!     eps(4)  = local xy strain
```

```
!     eps(5)  = local yz strain
!     eps(6)  = local zx strain
!
!     sig(1)  = local x  stress (Accumulative)
!     sig(2)  = local y  stress
!     sig(3)  = local z  stress
!     sig(4)  = local xy stress
!     sig(5)  = local yz stress
!     sig(6)  = local xz stress
!
!     hsv(1)  = Effective Plastic Strain, epsp
!     hsv(2)  = Triaxiality, eta
!     hsv(3)  = Normalised third deviatoric stress invariant, zeta
!     hsv(4)  = Normalised Lode Angle, thetab
!     hsv(5)  = Average Triaxiality
!     hsv(6)  = Average Normalised Lode Angle
!     hsv(7)  = Plastic Strain Rate
!     hsv(8)  = Temperature
!
!     dt1  =current time step size
!     capa =reduction factor for transverse shear
!     tt = current problem time.
!     temp = current problem temperature
!
!     all transformations into the element local system are
!     performed prior to entering this subroutine.  transformations
!     back to the global system are performed after exiting this
!     routine.
!
!     all history variables are initialized to zero in the input
!     phase.   initialization of history variables to nonzero values
!     may be done during the first call to this subroutine for each
!     element.
!
!     energy calculations for the dyna3d energy balance are done
!     outside this subroutine.
      include 'nlqparm'
      include 'bk06.inc'
      include 'iounits.inc'
      dimension cm(*),eps(*),sig(*),hsv(*),crv(lq1,2,*),cma(*),qmat(3,3)
      character*5 etype
      logical failel
!
      integer          :: i,j
      double precision :: E,pr,lambda,mu,svm,theta,pi,thetab,depsp,sr,dt
      double precision :: C1,C2,C3,C4,C5,C6,C7,sr0,n1,n2,k,m,Tm,Tref
      double precision :: D1,D2,D3,D4,epsfail
      double precision, dimension(6)  :: epspi,deps
```

```
129       double precision, dimension(6,6):: C
130 !
131 !     ****************************************************************
132 !                           MAIN SUBROUTINE
133 !     ****************************************************************
134 !     ----------------------------------------------------------------
135 !     Assign Variable names
136 !     ----------------------------------------------------------------
137       E    = cm(1)  ! Elastic Modulus
138       pr   = cm(2)  ! Poisson's Ratio
139       C1   = cm(3)
140       C2   = cm(4)
141       C3   = cm(5)
142       C4   = cm(6)
143       C5   = cm(7)
144       C6   = cm(8)
145       C7   = cm(9)
146       sr0  = cm(10)
147       n1   = cm(11)
148       n2   = cm(12)
149       k    = cm(13)
150       m    = cm(14)
151       Tm   = cm(15)
152       Tref = cm(16)
153       D1   = cm(17)
154       D2   = cm(18)
155       D3   = cm(19)
156       D4   = cm(20)
157       D5   = cm(21)
158       D6   = cm(22)
159       D7   = cm(23)
160       D8   = cm(24)
161 !     ----------------------------------------------------------------
162 !     Elastic Constitutive Tensor
163 !     ----------------------------------------------------------------
164 !     Calculate Lame constants
165       lambda = E*pr/(1.0D0 + pr)/(1.0D0 - 2*pr)
166       mu     = E/2/(1.0D0 + pr)
167 !     Initialise Elastic Constituve Tensor
168       do i=1,6
169         do j=1,6
170           C(i,j) = 0.0
171         enddo !j
172       enddo !i
173 !     Assemble Elastic Constituve Tensor
174       C(1,1) = lambda + 2*mu
175       C(1,2) = lambda
176       C(1,3) = lambda
```

```
177       C(2,1) = lambda
178       C(2,2) = lambda + 2*mu
179       C(2,3) = lambda
180       C(3,1) = lambda
181       C(3,2) = lambda
182       C(3,3) = lambda + 2*mu
183       C(4,4) = 2*mu
184       C(5,5) = 2*mu
185       C(6,6) = 2*mu
186 !     ------------------------------------------------------------------
187 !     Redefine strain increments
188 !     ------------------------------------------------------------------
189       deps(1) = eps(1)
190       deps(2) = eps(2)
191       deps(3) = eps(3)
192       deps(4) = 0.5*eps(4)
193       deps(5) = 0.5*eps(5)
194       deps(6) = 0.5*eps(6)
195 !     ------------------------------------------------------------------
196 !     Retrieve variables from previous time step
197 !     ------------------------------------------------------------------
198 !     Strain Rate
199       dt = dt1*1.0D-3
200       sr = hsv(7)
201 !     Temperature
202       T = temp
203 !
204 !     Assign variable names for history variables
205 !     Multiply Average values by previous effective plastic strain
206 !
207       hsv(5) = epsp*hsv(5)
208       hsv(6) = epsp*hsv(6)
209 !
210 !     Update Sress based on incremental plasticity theory
211 !
212       call integrate(C,deps,sig,epsp,svm,zeta,tt,depsp,sr,dt,T,mu,
213      1               C1,C2,C3,C4,C5,C6,C7,sr0,n1,n2,k,m,Tm,Tref)
214 !
215 !     ------------------------------------------------------------------
216 !     Assign history variables
217 !     ------------------------------------------------------------------
218 !     Effective Plastic Strain
219       hsv(1) = epsp
220 !
221 !     Triaxiality
222       p = -1.0/3.0*(sig(1) + sig(2) + sig(3))     ! Hydrostatic Pressure
223       if (tt.ne.0.0) then
224   hsv(2) = -p/svm                  ! Triaxiality
```

```
225       endif
226 !
227 !     Lode Angle
228       hsv(3) = zeta
229       pi = 4*ATAN(1.D0)
230       if (zeta.gt.1.0) then
231   theta = 0.0D0
232       elseif (zeta.lt.-1.0) then
233   theta = pi/3
234       else
235   theta = 1.0D0/3.0D0*ACOS(zeta)        ! Lode Angle
236       endif
237       thetab = 1.0D0 - 6*theta/pi       ! Normalised Lode Angle
238       hsv(4) = thetab
239 !
240 !     Average Values
241       if(epsp.ne.0.0) then
242   hsv(5) = (hsv(5) + hsv(2)*depsp)/epsp
243   hsv(6) = (hsv(6) + hsv(4)*depsp)/epsp
244       endif
245 !
246 !     Strain Rate
247       if(dt.eq.0.0) then
248         sr = 0.0
249       endif
250       hsv(7) = sr
251       hsv(8) = T
252 !
253 !     Failure
254       D1Rate = D1 - D2*sr**D3
255       D2Rate = D4 - D5*sr**D6
256       epsfail = D1Rate*exp(-D2Rate*hsv(5))*(D7*hsv(6)**2 + D8)
257       failel = epsp.gt.epsfail
258       return
259       end
260 !
261 ! ********************************************************************
262 !                       RADIAL RETURN ALGORITHM
263 ! ********************************************************************
264 !
265       subroutine integrate(C,eps,sig,epsp,svm,zeta,tt,depsp,sr,dt,T,mu,
266      1                     C1,C2,C3,C4,C5,C6,C7,sr0,n1,n2,k,m,Tm,Tref)
267 !
268       integer  :: i,ii,jj,iter
269       double precision :: f,mu,dlambda,H,Hp1,Hp2
270       double precision :: C1,C2,C3,C4,C5,C6,C7,sr0,n1,n2,k,m,Tm,Tref
271       double precision :: epsp,depsp,svm,j3,epsde,epstr
272       double precision, dimension(6)   :: eta,sig,sigt,eps,epspi,epsd
```

```
      double precision, dimension(6,6) :: C
!
!     Compute Elastic Predictor Trial Stress
!
      do ii=1,6
  sigt(ii) = sig(ii)
        do jj=1,6
          sigt(ii) = sigt(ii) + C(ii,jj)*eps(jj)
        enddo ! jj
      enddo ! ii
!
!     Check for Yielding
!
      call vonmises(sigt,svm,eta)
      call hardfcn(epsp,H,Hp1,Hp2,sr,T,C1,C2,C3,C4,C5,C6,C7,sr0,n1,n2,
     1             k,m,Tm,Tref)
!
      f = svm - H
!
!     ---------------------------------------------------------------
!                              PLASTIC STEP
!     ---------------------------------------------------------------
      if(f.gt.0.0) then ! Material in Plastic State
!       Calculate Plastic Multiplier
        dlambda = 3.0/2.0*(f + sr*Hp2)/(svm*(Hp1 + Hp2/dt + 3.0*mu))
!   Update Plastic Strain Increment
  do i=1,6
    epspi(i) = dlambda*eta(i)
  enddo !i
!   Update Stress
  do ii=1,6
    sig(ii) = sigt(ii)
    do jj = 1,6
      sig(ii) = sig(ii) - C(ii,jj)*epspi(jj)
    enddo ! jj
  enddo ! ii
!   Update Effective Plastic Strain
  depsp = 2.0D0/3.0D0*svm*dlambda
  epsp = epsp + depsp
!   Calculate Plastic Strain Rate
  sr = depsp/dt
!       Calculate effective stress
  call vonmises(sig,svm,eta)
!
!     ---------------------------------------------------------------
!                               ELASTIC STEP
!     ---------------------------------------------------------------
      else  ! Material in Elastic State
```

```
!   Assign Trial Stress to Actual Stress (Elastic Regime)
  do i=1,6
    sig(i) = sigt(i)
    depsp = 0.0

  enddo
      endif
!
!     ----------------------------------------------------------------
!                     CALCULATE THIRD DEVIATORIC INVARIANT
!     ----------------------------------------------------------------
!
!     Calculate Lode Angle
      j3 = eta(1)*eta(2)*eta(3) + 2*eta(4)*eta(5)*eta(6)
      j3 = j3 - eta(4)**2*eta(3) - eta(5)**2*eta(1) - eta(6)**2*eta(2)
      if (tt.ne.0.0) then
  zeta = 27.0D0/2.0D0*j3/(svm**3)
      endif
!
      return
      end
!
! ********************************************************************
!                       VON MISES EQuIVALENT STRESS
! ********************************************************************
!
      subroutine vonmises(sig,svm,eta)
! !
      integer :: i
      double precision :: s1,s2,s3,s4,s5,s6,sigh,svm,j2
      double precision, dimension(6) :: eta,sig,sigd
!
!     Assign variables for stress components
!
      s1 = sig(1)
      s2 = sig(2)
      s3 = sig(3)
      s4 = sig(4)
      s5 = sig(5)
      s6 = sig(6)
!
!     Calculate Hydrostatic Stress Magnitude
!
      sigh = 1.0D0/3.0D0*(s1 + s2 + s3)
!
!     Calculate Stress Deviator
!
      sigd(1) = s1 - sigh
```

```
      sigd(2) = s2 - sigh
      sigd(3) = s3 - sigh
      sigd(4) = s4
      sigd(5) = s5
      sigd(6) = s6
!
!     Calculate second invariant, J2
!
      j2 = 0.0D0
      do i=1,3
  j2 = j2 + 0.5D0*sigd(i)**2
      enddo ! i
      do i=4,6
  j2 = j2 + sigd(i)**2
      enddo ! i
!
!     Define von Mises Stress and Yield Surface
!
      svm = sqrt(3.0D0*j2)
!
!     Compute Yield Surface Normal, eta
!
      eta(1) = sigd(1)
      eta(2) = sigd(2)
      eta(3) = sigd(3)
      eta(4) = sigd(4)
      eta(5) = sigd(5)
      eta(6) = sigd(6)
!
      return
      end
!
! ********************************************************************
!                          HARDENING FUNCTION
! ********************************************************************
!
      subroutine hardfcn(epsp,H,Hp1,Hp2,sr,T,C1,C2,C3,C4,C5,C6,C7,sr0,
     1                   n1,n2,k,m,Tm,Tref)
!
      double precision :: H,Hp1,Hp2,C1,C2,C3,C4,C5,C6,C7,sr0,n1,n2,k
      double precision :: sr
      double precision :: ftemp,m,Tm,Tref,T
!
!     Compute Hardening Function, H, and its Derivatives, Hp1,Hp2
!
      if(T.lt.Tref) then
        ftemp = 1.0D0  ! Temperature dependence function
      else
```

```
417         ftemp = 1.0D0 - ((T - Tref)/(Tm - Tref))**m
418       endif
419 !
420       if(epsp.eq.0.0) then
421       Hp1 = 0.0
422       else
423       Hp1 = (C2*n1*epsp**(n1-1.0D0))*ftemp ! Strain derivative
424       endif
425 !
426 !     Piecewise rate depence function
427       if(sr.gt.sr0) then
428       H = (C1 + C2*epsp**n1 + (C5 - C6*epsp**n2)*log(sr/sr0)
429      1    + C7*sr**k)*ftemp
430       Hp2 = ((C5 - C6*epsp**n2)/(sr0 + sr) + k*C7*sr**(k-1.0D0))*ftemp
431       else
432       H = (C1 + C2*epsp**n1)*ftemp
433       Hp2 = 0.0D0
434       endif
435 !
436       return
437       end
438 !
439 ! ********************************************************************
440 !                             END OF PROGRAM
441 ! ********************************************************************
442 !
```

Appendix B

Wave Speed Equation Derivations

Derivations for dilatational waves in both infinite media and slender bars can be derived using linear elastic, infinitesimal strain theory. The linear elastic relationship between the stress and strain tensors can be written as:

$$T_{ij} = \lambda \varepsilon_{kk} \delta_{ij} - \mu \left(\frac{\partial u_i}{\partial x_j} + \frac{\partial u_j}{\partial x_i} \right) \tag{B.1}$$

and the infinitesimal version of Cauchy's equation of motion can be written as:

$$\rho \frac{\partial^2 u_i}{\partial t^2} = \frac{\partial T_{ij}}{\partial u_j} \quad \text{(Assuming no body forces)} \tag{B.2}$$

Using Equation B.1 to determine an expression for the divergence of the stress tensor, the equation of motion can be written on in terms of the derivatives of the displacements.

$$\rho \frac{\partial^2 u_i}{\partial t^2} = (\lambda + \mu) \frac{\partial \varepsilon_{kk}}{\partial u_i} + \mu \frac{\partial^2 u_i}{\partial x_j \partial x_j} \tag{B.3}$$

Using these three equations, the wave equation can be derived for the different boundary conditions.

One-dimensional waves in infinite media

For one-dimensional wave propagation in infinite media, the movement in the directions transverse to the wave direction is negligible in comparison to the displacement in the direction of the wave, meaning $\mathbf{u} = u(x_1, t)\mathbf{e_1}$. Consequentially, the trace of the strain tensor can be simplified to:

$$\varepsilon_{kk} = \varepsilon_{11} = \frac{\partial u}{\partial x_1} \tag{B.4}$$

Using Equations B.4 and B.3, the wave equation can be written as:

$$\frac{\partial^2 u}{\partial t^2} = c^2 \frac{\partial^2 u}{\partial x_1^2} = \frac{\lambda + 2\mu}{\rho} \frac{\partial^2 u}{\partial x_1^2} \tag{B.5}$$

The Lamè parameters, λ and μ can be written in terms of the elastic modulus, E, and Poisson's ratio, ν, which can be used to define the dilatational wave speed as:

$$c = \sqrt{\frac{E}{\rho} \frac{(1-\nu)}{(1+\nu)(1-2\nu)}} \tag{B.6}$$

One-dimensional waves in a slender bar

The boundary conditions for stress wave propagation in a slender bar are significantly different to in an infinite medium. The displacements in the transverse directions can no longer be considered negligible because distance to the radial boundaries of the bar is significant in comparison to the displacement in the normal direction caused by the wave, meaning the strains can be written as:

$$\varepsilon_{22} = \varepsilon_{33} = -\mu\varepsilon_{11} = -\mu \frac{\partial u}{\partial x_1} \tag{B.7}$$

where u is the displacement in the normal direction. Using simple linear elastic theory for uniaxial tension or compression, the stress tensor component in the normal direction can be written as:

$$T_{11} = \sigma = E\varepsilon_{11} \tag{B.8}$$

and consequently Equation B.2 can be simplified to:

$$\frac{\partial^2 u}{\partial t^2} = \frac{E}{\rho}\frac{\partial^2 u}{\partial x_1^2} \tag{B.9}$$

As can be seen from Equations B.5 and B.9, the difference in the two wave speeds can be defined as:

$$\frac{c_{inf}}{c_{bar}} = \frac{1-\nu}{(1+\nu)(1-2\nu)} \tag{B.10}$$

Appendix C

Drawings

This appendix contains the technical drawings made for the various tensile specimen geometries.

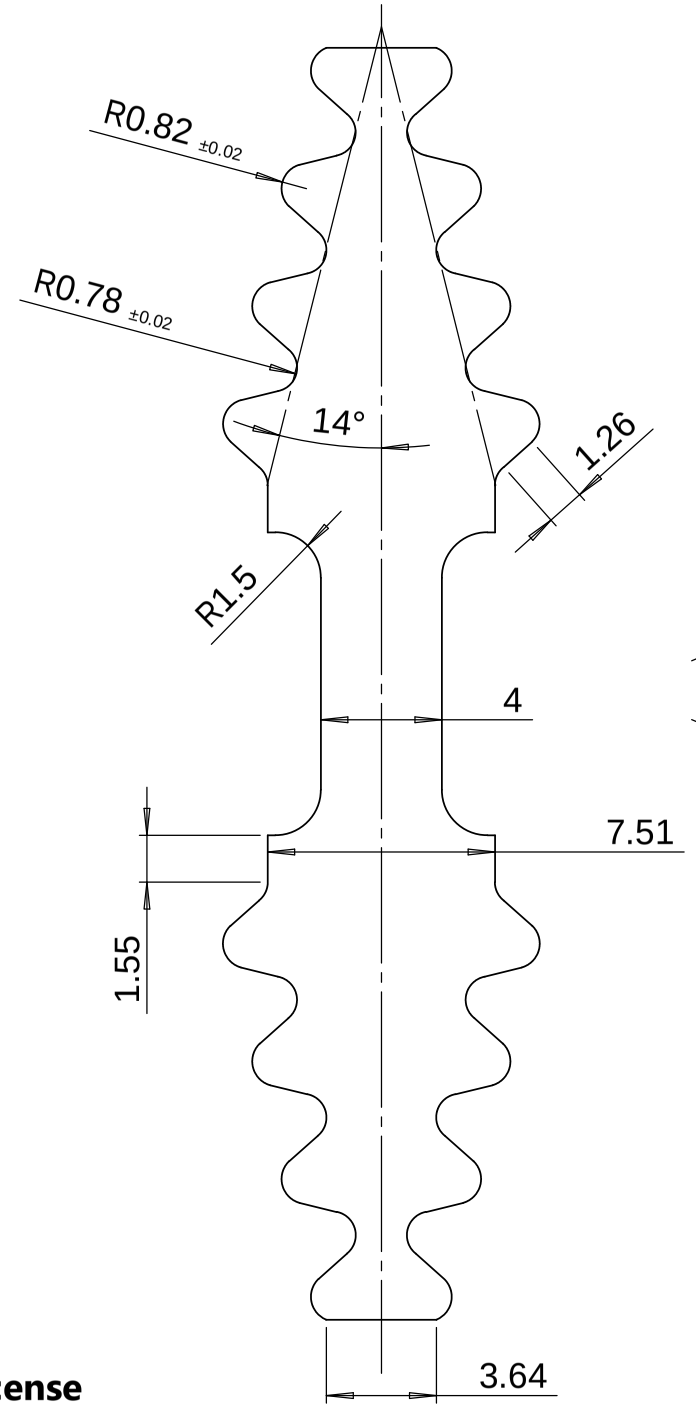

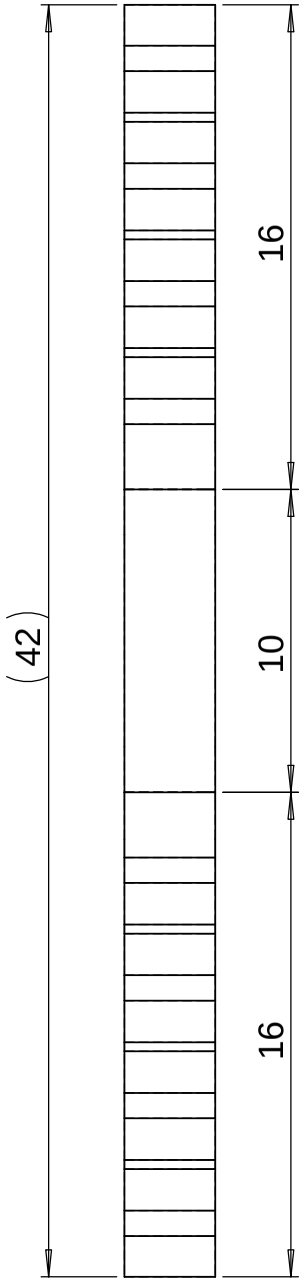

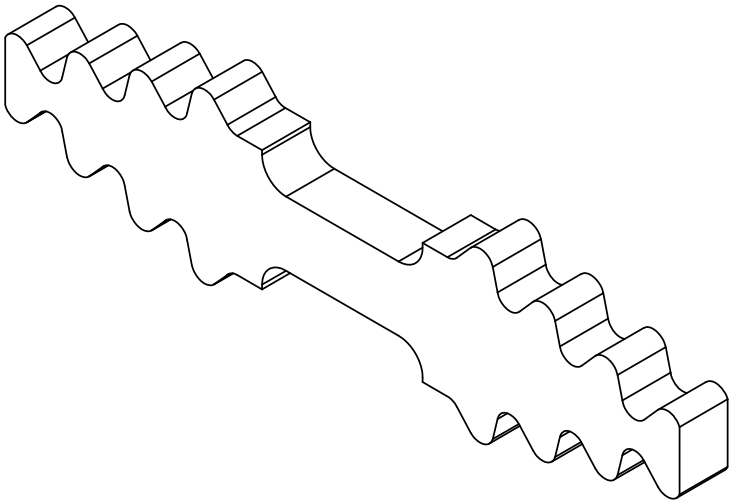

SCALE 3 : 1

A4 Landscape	University of Cape Town Department of Mechanical Engineering				
	Title: specimen_flat				
Quantity: 9	Part Finish	Date: 2015/04/17	Scale: 4:1	Sheet1	of 1
Material: DOMEX 355MC	Drawn By: Matthew Weyer WYRMAT001			Drawing Number 1	

SolidWorks Student License
Academic Use Only

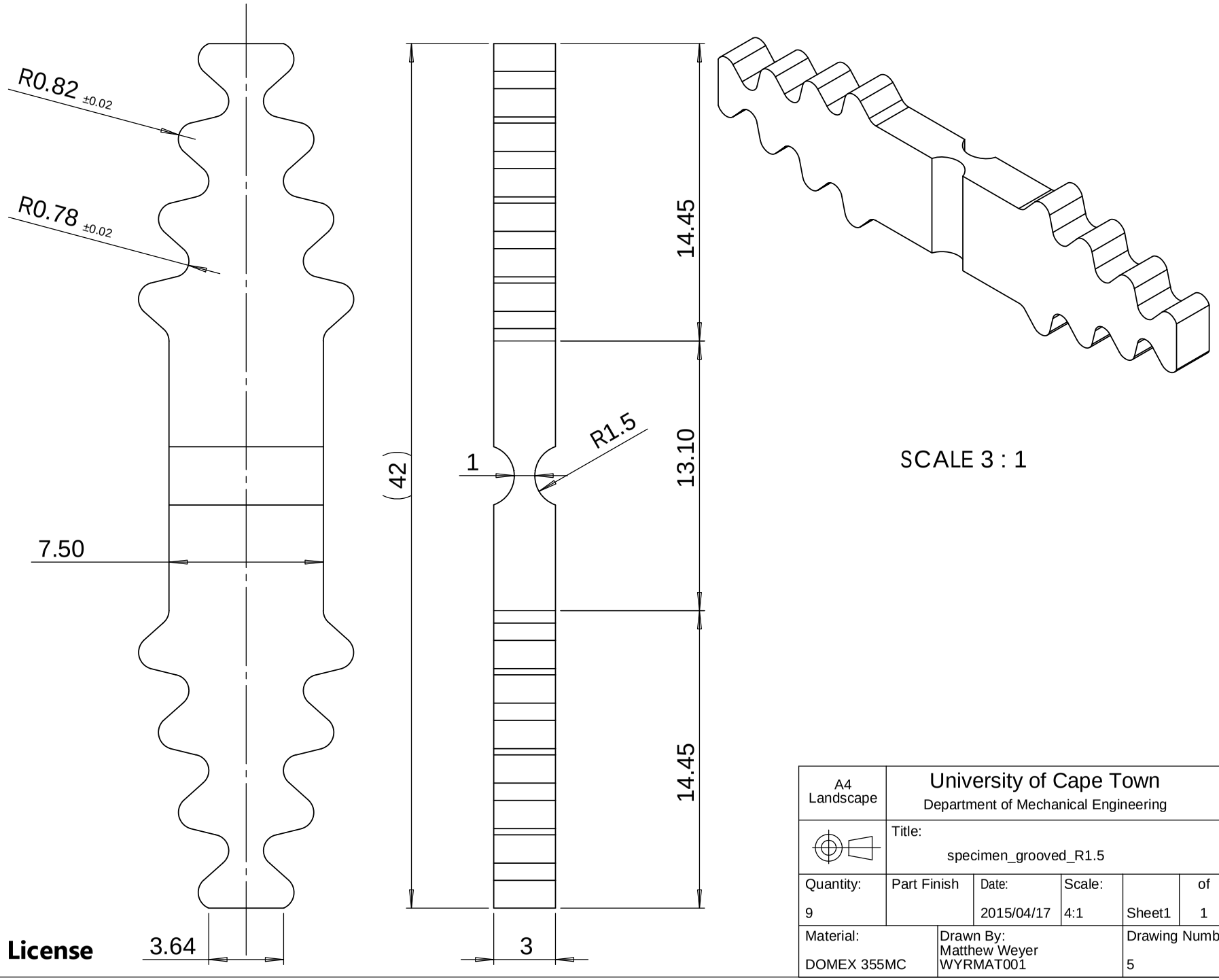

A4 Landscape	University of Cape Town Department of Mechanical Engineering				
	Title: specimen_grooved_R1.5				
Quantity: 9	Part Finish	Date: 2015/04/17	Scale: 4:1	Sheet1	of 1
Material: DOMEX 355MC	Drawn By: Matthew Weyer WYRMAT001			Drawing Number 5	

SolidWorks Student License
Academic Use Only

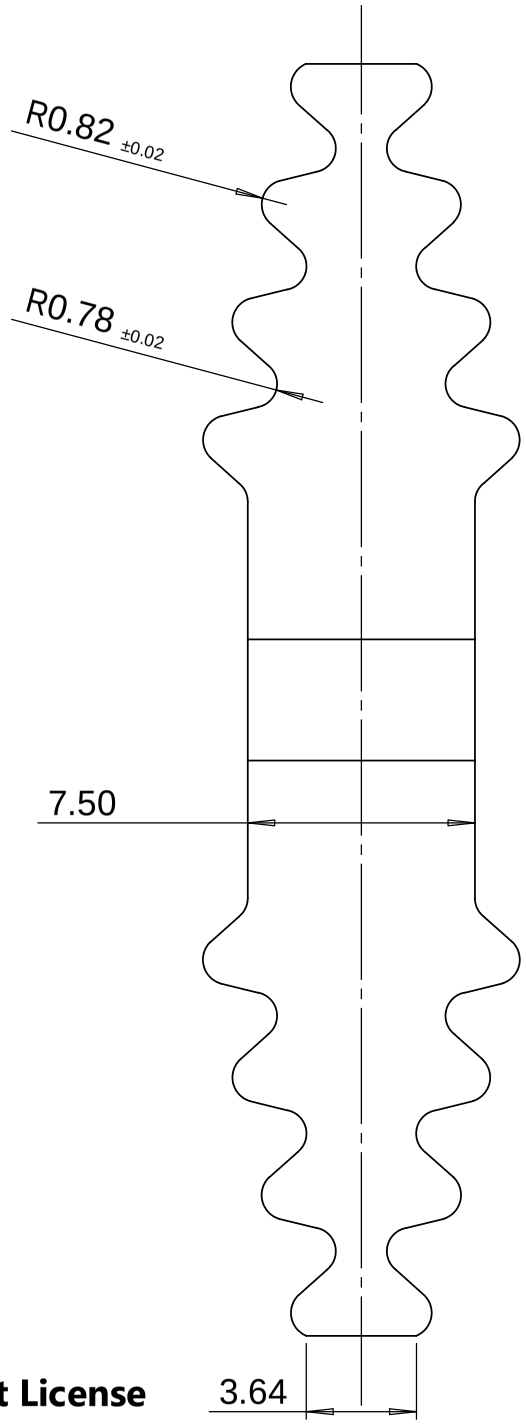

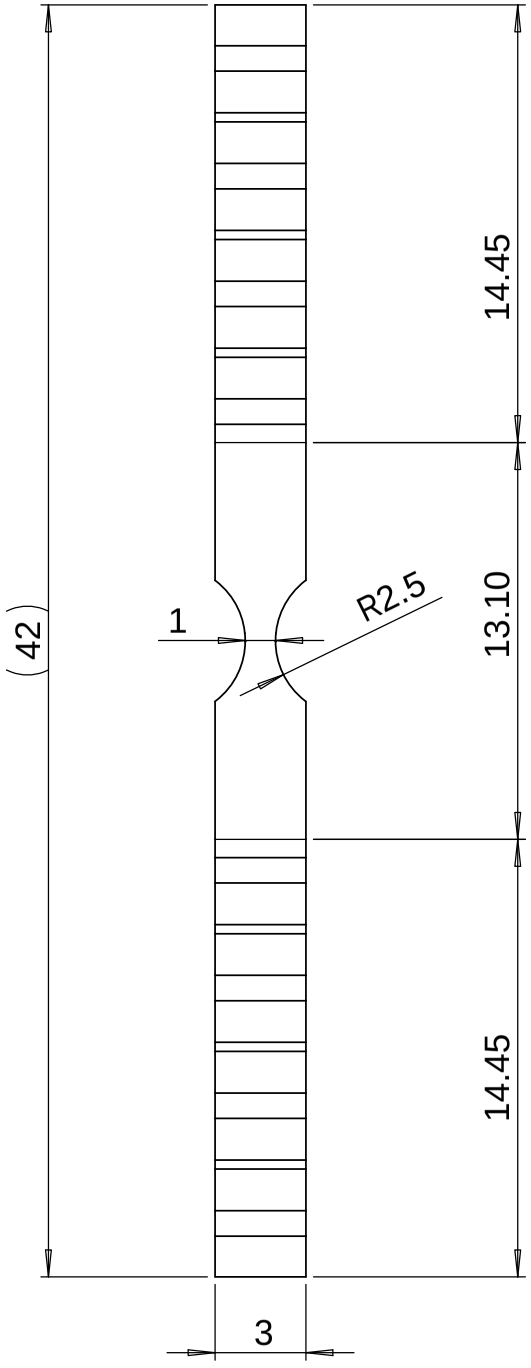

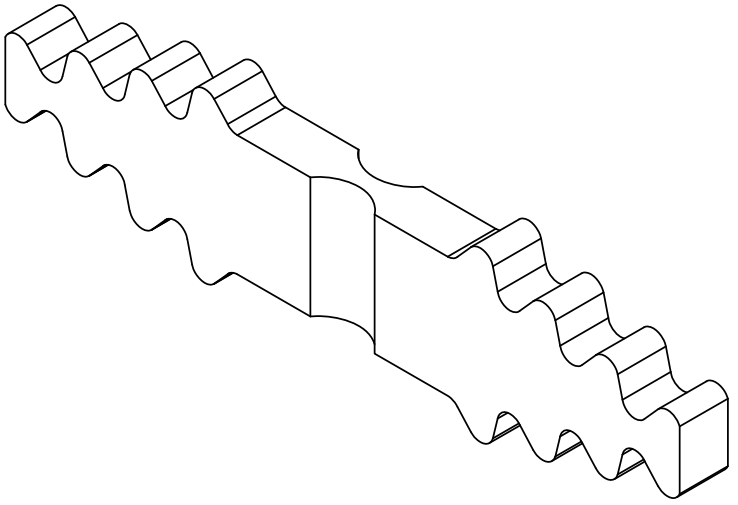

SCALE 3 : 1

A4 Landscape	University of Cape Town Department of Mechanical Engineering				
	Title: specimen_grooved_R2.5				
Quantity: 9	Part Finish	Date: 2015/04/17	Scale: 4:1	Sheet1	of 1
Material: DOMEX 355MC	Drawn By: Matthew Weyer WYRMAT001			Drawing Number 6	

SolidWorks Student License
Academic Use Only

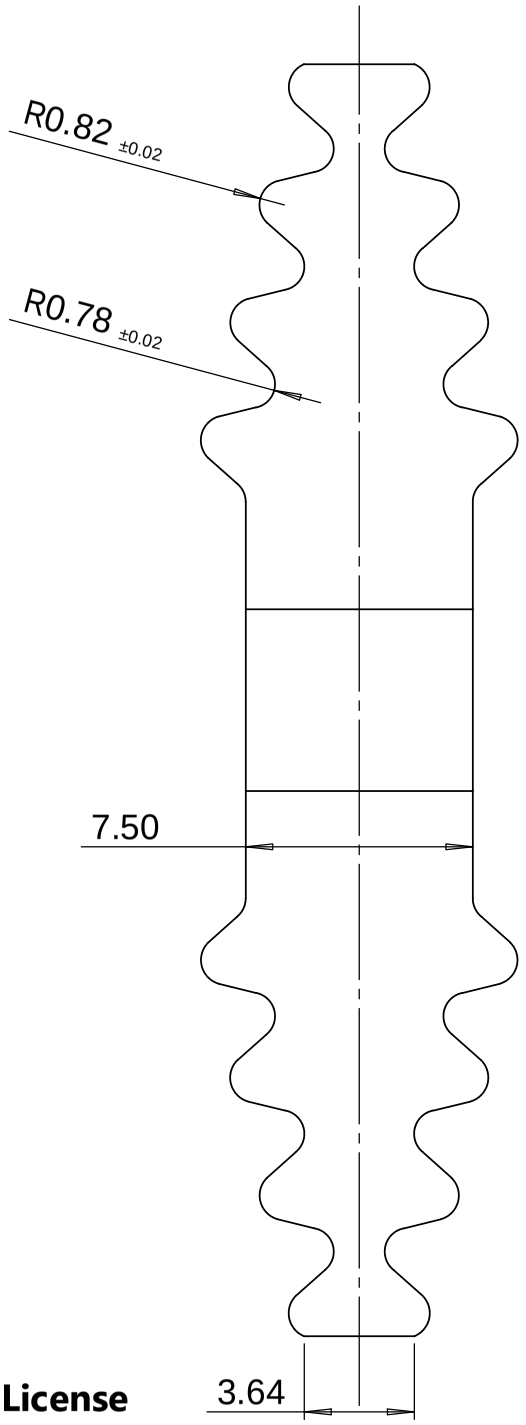

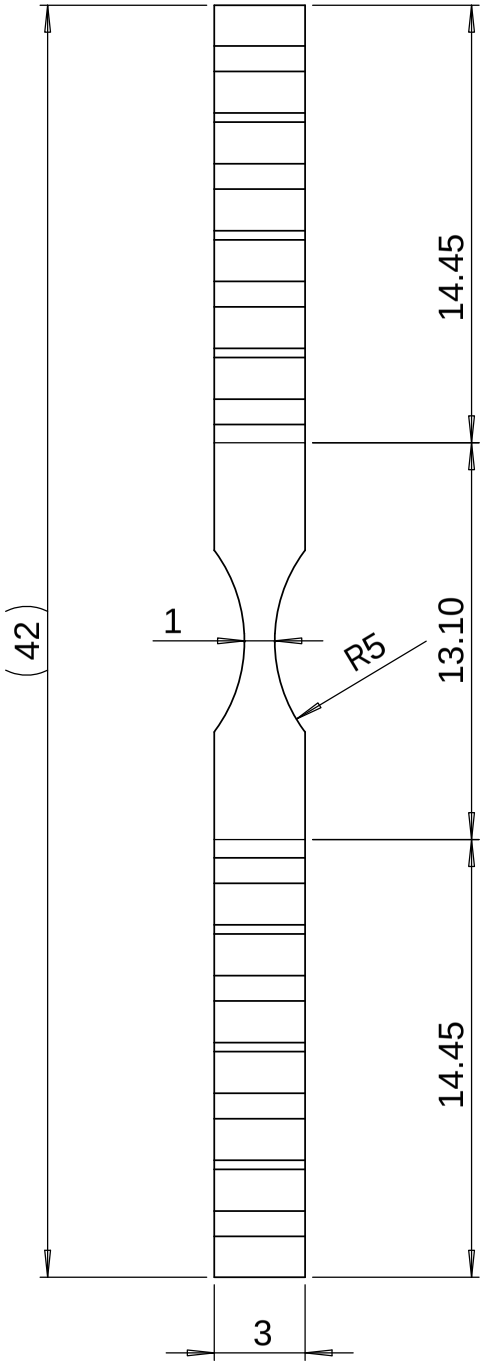

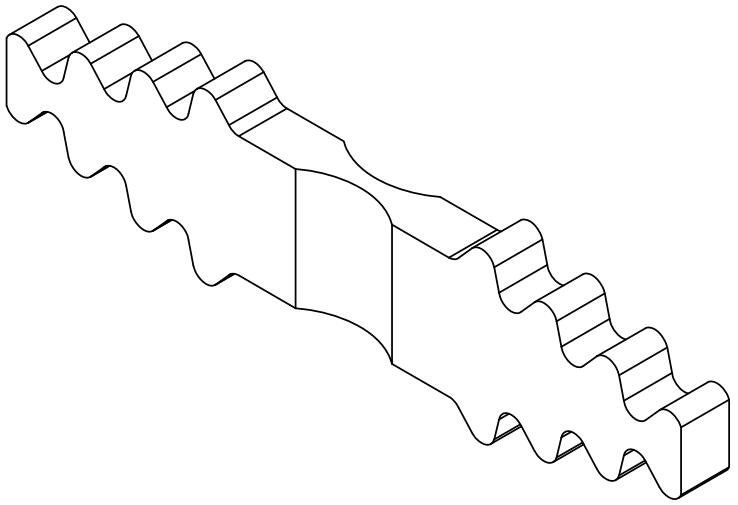

SCALE 3 : 1

A4 Landscape	University of Cape Town Department of Mechanical Engineering				
	Title: specimen_grooved_R5.0				
Quantity: 9	Part Finish	Date: 2015/04/17	Scale: 4:1	Sheet1	of 1
Material: DOMEX 355MC	Drawn By: Matthew Weyer WYRMAT001			Drawing Number 7	

SolidWorks Student License
Academic Use Only

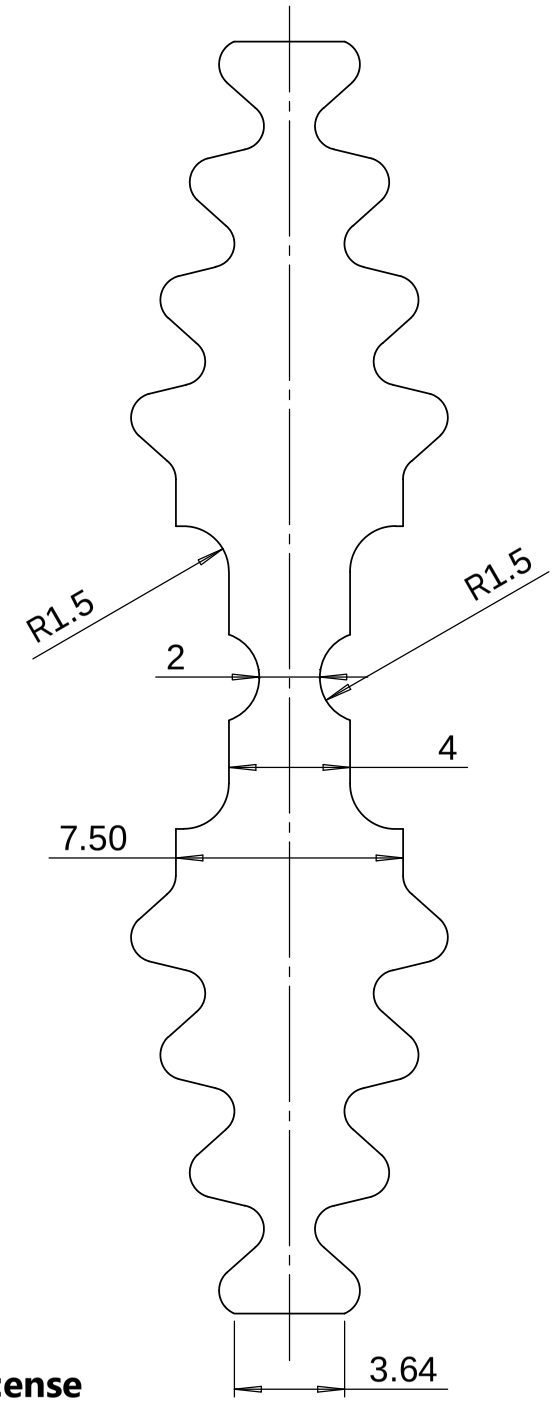

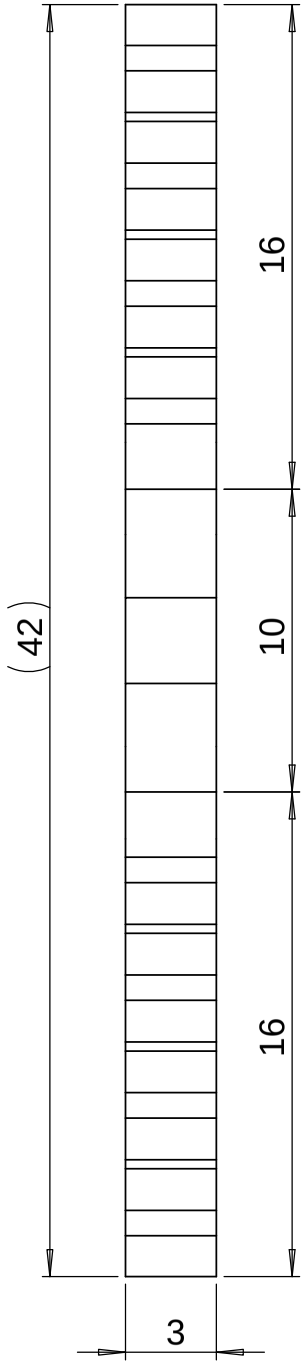

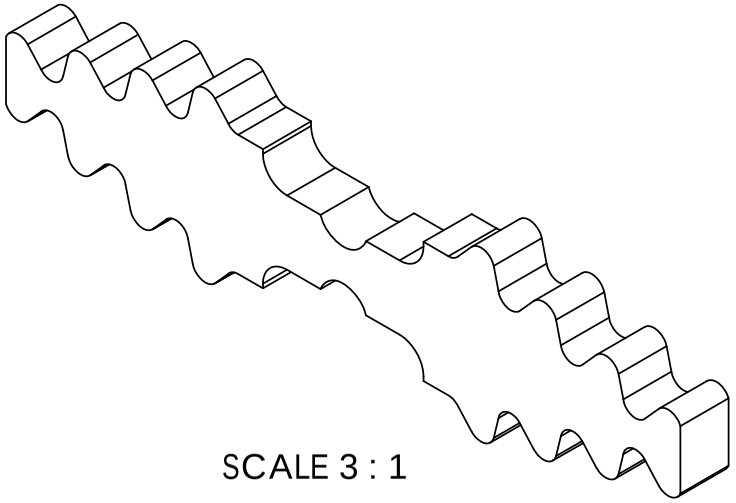

SCALE 3 : 1

A4 Landscape	University of Cape Town Department of Mechanical Engineering				
	Title: specimen_notched_R1.5				
Quantity: 9	Part Finish	Date: 2015/04/17	Scale: 4:1	Sheet1	of 1
Material: DOMEX 355MC	Drawn By: Matthew Weyer WYRMAT001			Drawing Number 2	

SolidWorks Student License
Academic Use Only

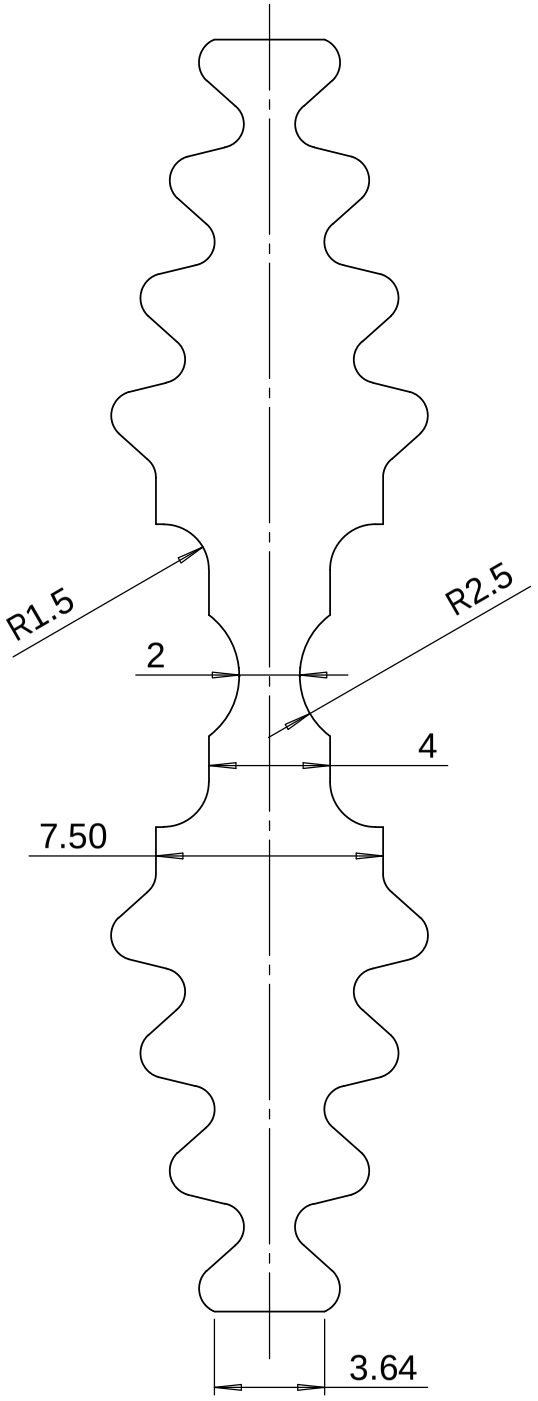

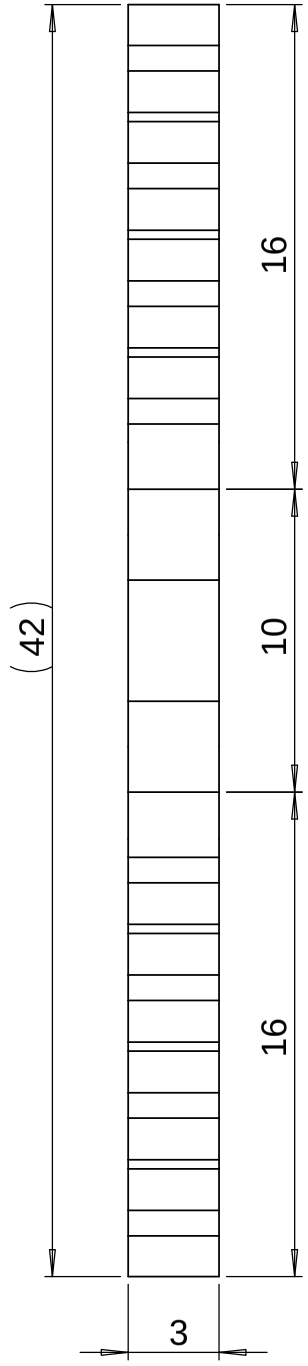

A4 Landscape	University of Cape Town Department of Mechanical Engineering				
	Title: specimen_notched_R2.5				
Quantity: 9	Part Finish	Date: 2015/04/17	Scale: 4:1	Sheet1	of 1
Material: DOMEX 355MC	Drawn By: Matthew Weyer WYRMAT001			Drawing Number 3	

SolidWorks Student License
Academic Use Only

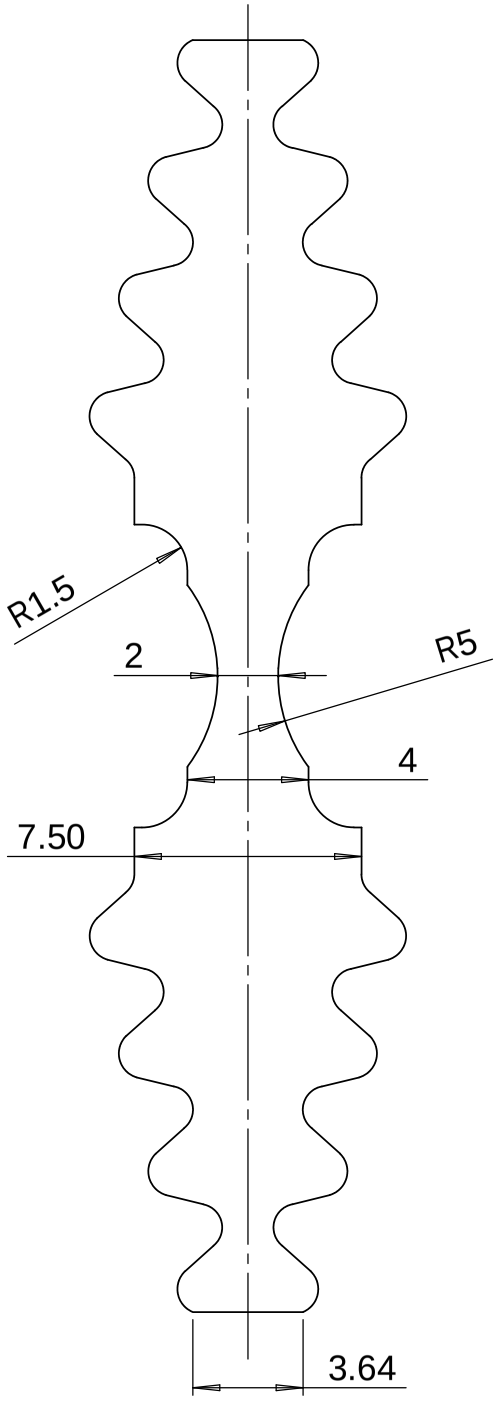

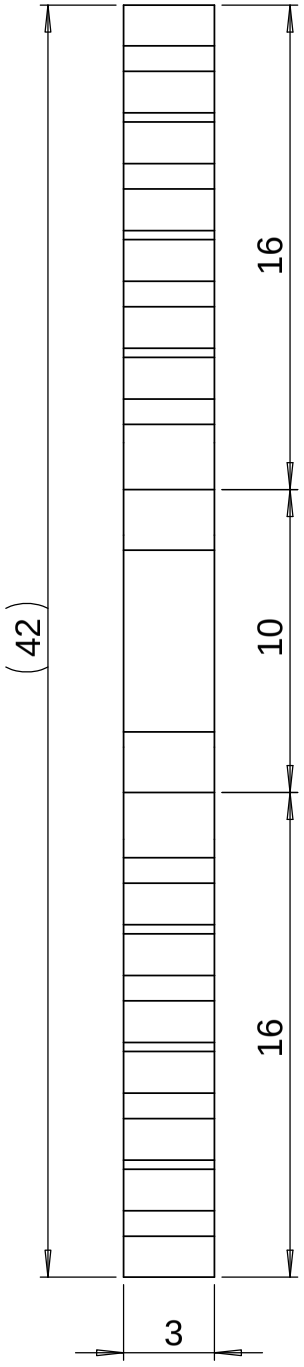

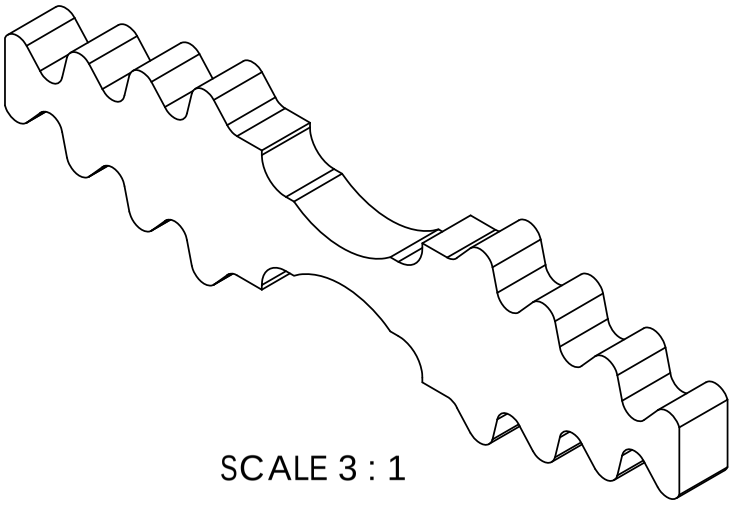

SCALE 3 : 1

A4 Landscape	University of Cape Town Department of Mechanical Engineering				
	Title: specimen_notched_R5				
Quantity: 9	Part Finish	Date: 2015/04/17	Scale: 4:1	Sheet1	of 1
Material: DOMEX 355MC	Drawn By: Matthew Weyer WYRMAT001			Drawing Number 4	

SolidWorks Student License
Academic Use Only

Appendix D

Assessment of Ethics in Research Projects Form

This appendix contains the Assessment of Ethics in Research Projects form required for submission.

EBE Faculty: Assessment of Ethics in Research Projects

Any person planning to undertake research in the Faculty of Engineering and the Built Environment at the University of Cape Town is required to complete this form before collecting or analysing data. When completed it should be submitted to the supervisor (where applicable) and from there to the Head of Department. If any of the questions below have been answered YES, and the applicant is NOT a fourth year student, the Head should forward this form for approval by the Faculty EIR committee: submit to Ms Zulpha Geyer (Zulpha.Geyer@uct.ac.za; Chem Eng Building, Ph 021 650 4791). Students must include a copy of the completed form with the thesis when it is submitted for examination.

Name of Principal Researcher/Student: MATTHEW WEYER

Department: MECHANICAL ENGINEERING

If a Student: Degree: M.Sc. MECHANICAL ENGINEERING

Supervisor: T.J. CLOETE

If a Research Contract indicate source of funding/sponsorship:

Research Project Title: EXPERIMENTAL ~~AND THEORETICAL~~ AND THEORETICAL STUDY ON STRAIN RATE EFFECTS ON DUCTILE DAMAGE

Overview of ethics issues in your research project:

Question 1: Is there a possibility that your research could cause harm to a third party (i.e. a person not involved in your project)?	YES	(NO)
Question 2: Is your research making use of human subjects as sources of data? If your answer is YES, please complete Addendum 2.	YES	(NO)
Question 3: Does your research involve the participation of or provision of services to communities? If your answer is YES, please complete Addendum 3.	YES	(NO)
Question 4: If your research is sponsored, is there any potential for conflicts of interest? If your answer is YES, please complete Addendum 4.	YES	(NO)

If you have answered YES to any of the above questions, please append a copy of your research proposal, as well as any interview schedules or questionnaires (Addendum 1) and please complete further addenda as appropriate.

I hereby undertake to carry out my research in such a way that

- there is no apparent legal objection to the nature or the method of research; and
- the research will not compromise staff or students or the other responsibilities of the University;
- the stated objective will be achieved, and the findings will have a high degree of validity;
- limitations and alternative interpretations will be considered;
- the findings could be subject to peer review and publicly available; and
- I will comply with the conventions of copyright and avoid any practice that would constitute plagiarism.

Signed by:

	Full name and signature	Date
Principal Researcher/Student: MATTHEW PETER WEYER	Signed	11/02/2015

This application is approved by:

Supervisor (if applicable):	T.J. Cloete Signed	17/02/2015
HOD (or delegated nominee): Final authority for all assessments with NO to all questions and for all undergraduate research.	R.D. KNUTSEN	18/02/2015
Chair: Faculty EIR Committee For applicants other than undergraduate students who have answered YES to any of the above questions.		